DEVELOPMENT OF COMPACT LASERS FOR LASER REMOTE SENSING APPLCATIONS

by

Shuo Li

B. S., Nankai University, 2010

M. S., University of Pittsburgh, 2011

Submitted to the Graduate Faculty of

The Swanson School of Engineering in partial fulfillment

of the requirements for the degree of

Doctor of Philosophy

University of Pittsburgh

2018

UNIVERSITY OF PITTSBURGH

SWANSON SCHOOL OF ENGINEERING

This dissertation was presented

by

Shuo Li

It was defended on

July 9th, 2018

and approved by

Albert To, Ph.D., Associate Professor, Department of Mechanical Engineering and Materials Science

Guangyong Li, Ph.D., Associate Professor, Department of Electrical and Computer Engineering

Susheng Tan, Ph.D., Associate Professor, Department of Electrical and Computer Engineering

Zhihong Mao, Ph.D., Associate Professor, Department of Electrical and Computer Engineering

Dissertation Director: Kevin Chen, Ph.D., Professor, Department of Electrical and Computer Engineering

--

DEVELOPMENT OF COMPACT LASERS FOR LASER REMOTE SENSING APPLCATIONS

Shuo Li, PhD

University of Pittsburgh, 2018

Laser-induced breakdown spectroscopy (LIBS) is a powerful laser sensing technique to determine elemental compositions. It has been widely used in laboratories. There is increasing focus on the development of field-portable LIBS instruments as stand-off sensing tools for harsh or dangerous environments. In this dissertation, we focused on developing field-portable, compact lasers for LIBS applications, using both conventional and advanced manufacturing methods.

We first demonstrated the development of a compact actively Q-switched laser, followed by the development of a double-pulse laser based on the same optical design. Several LIBS experiments were successfully performed using these two lasers. We also investigated the advantages of using double-pulse LIBS during the early plasma stage. Significantly signal improvement had been observed. We also demonstrated selective signal enhancement which is usually achieved by using bulky and expensive high power tunable laser in the lab. The low-cost instrument and innovative technology we demonstrated here make it possible to extend such improvement to field-portable LIBS applications.

Next, we introduced the development of a compact unibody laser enabled by addictive manufacturing and its advantages compared with laser made by conventional method. The technology exploits the flexibility of the bottom-up manufacturing schemes to produce entire laser photonic systems made of flexure alignment structure and cellular cooling structures. We also explored the 3D printing of advanced diamond/metal composites with excellent thermomechanical property. This innovation in the digitization of laser manufacturing process and the utilization of

new materials and structures will allow rapid design modification and radical design innovation in developing laser and photonic systems, which can be deployed on mobile drone platforms for a wide array of industrial, consumer, environmental, and military applications.

TABLE OF CONTENTS

LIST OF TABLES

LIST OF FIGURES

PREFACE

First, I would like to express my sincere gratitude to my advisor Prof. Kevin Chen for the generous support of my Ph.D. study, for his kindness, motivation, and immense knowledge. I could not have imagined having a better advisor and mentor for my Ph.D. study. Besides my advisor, I would like to thank the rest of my thesis committee: Prof. Alber To, Prof. Guangyong Li, Prof. Susheng Tan and Prof. Zhihong Mao, for their support and kindness through my study.

My sincere thanks also go to Prof. Yongfeng Lu at the University of Nebraska–Lincoln. Prof. Lu kindly provided me an opportunity to work in his lab as a visiting student and continually offered generous support for my Ph.D study. I couldn't earn my Ph.D. without your kind help!

I would also like to thank my fellow doctoral students and friends such as, Dr. Bryan Nelsen, Dr. Tong Chen, Dr. Qingqing Wang, Dr. Mingshan Li, Dr. Rongzhang Chen, Dr. Aidong Yan, Dr. Lei Liu, Dr. Xi Huang, Ran Zou, Mohan Wang, Sheng Huang, Xuan Liang, Zach Splain, and Lin Chen for their feedback, cooperation and of course friendship.

Nevertheless, I would like to thank my family: my father Fenghai Li, my mother Hongbing Zhao and my girlfriend Yiliang Li, for supporting me spiritually throughout writing this thesis and my life in general. Thank you for encouraging me in all of my pursuits and inspiring me to follow my dreams!

1.0 INTRODUCTION

Laser-induced breakdown spectroscopy (LIBS) is a powerful technology to determine elemental composition. It offers many advantages over conventional atomic emission spectroscopy techniques, such as the ability to detect all elements, simultaneous multi-element detection, real-time and in situ analysis, no sample preparation and simply setup.[1,2] These merits make LIBS a good candidate for the remote sensing applications. A typical LIBS system usually contains two parts, a laser source and a spectrometer. In laboratory LIBS setup, commonly used laser sources are high power Q-switched Nd: YAG lasers that side pumped by flash lamp. These lasers not only are bulky due to their complex electronics and the need for water cooling, but also have very low wall-plug efficiency, making them unsuitable as portable laser sources for LIBS applications.

Besides laser performance itself, dimension, weight and efficiency are the key requirements for portable lasers. Considerable progress has been achieved in the miniaturization of lasers, such as the development of fiber lasers, microchip lasers and compact flash lamp pumped solid-state lasers.[3] Recently, a new type of compact Q-switched laser that end pumped by vertical-cavity surface-emitting laser (VCSEL) array has been developed.[4] It has intrinsic advantages over conventional flash-lamp pumped lasers in terms of efficiency, compactness and reliability. The potential advantages of such compact lasers for LIBS application is studied in this thesis, where several compact laser systems based on VCSEL end-pumping were designed, built and tested for LIBS applications.

Compared with other spectrometric methods, LIBS still suffers from a relatively poor sensitivity. Lots of researchers have devoted their work to improve LIBS performance. But not all of them is suitable to be adapted to field-portable LIBS. Among these various methods, double-pulse LIBS have been proved to be a very effective approach for improving LIBS performance in terms of enhanced emission intensities, lower limits of detections, improved signal-to-noise ratio and having the potential to perform field-portable LIBS experiment.[5] Despite of the intensive researches in double-pulse and field-portable LIBS, very few researches have been performed on double-pulse LIBS using field-portable laser system because of lacking suitable laser source. Therefore, a field-portable double-pulse laser system based on VCSEL end-pumping was also developed for LIBS application in this thesis.

Both the single-pulse and double-pulse laser systems developed here have been proven to be an effective laser sources for LIBS application in terms of dimension, weight, efficiency and the ability to improve LIBS performance. These two laser systems were made using conventional laser manufacturing methods, where commercial available off-the-shelf and CNC machined parts are used. To further explored the possibility of building compact laser system, 3D printing, also known as additive manufacturing, was used to develop a compact unibody laser system with total weight less than 150 g. Its performance was also improved using advanced cellular and flexure structure. We also explored the 3D printing of advanced diamond/metal composites with excellent thermomechanical property.

1.1 ORGANIZATION OF THE DISSERTATION

The rest of the dissertation is organized as follows. Chapter 1 will introduce the fundamental of LIBS as well as an overview of compact laser sources. Chapter 2 introduces the development of a field-portable actively Q-switched laser end-pumped by VCSEL including both optical and electrical design. Several LIBS experiments have also been performed to test its performance. Chapter 3 introduces the development of a field-portable double-pulse laser which shares the same cavity design as the laser in previous chapter but with several advances. Significant improvements have been achieved in LIBS experiments using such double-pulse laser compared with single-pulse laser. Chapter 4 introduces the development of a compact unibody laser enabled by additive manufacturing and its advantages compared with laser made by conventional method. Chapter 5 discuss 3the D printing of advanced diamond/metal composites with cellar structure. Chapter 6 is the conclusion and future direction.

1.2 LASER-INDUCED BREAKDOWN SPECTRUM

Laser-induced breakdown spectroscopy is a powerful diagnostic technique for the determination of elemental compositions of specimens in gaseous, liquid and solid phases.[1,6] It belongs to the family of atomic emission spectroscopy (AES). The basic steps are: atomization of samples to produce high energy atomic species, detection of the emitted light from these species and determination of the concentration in the sample. The dielectric breakdown of gases had been known for at least 100 years, where discharges can be produced in low-pressure gas by applying AC voltage. The production of dielectric breakdown by optical radiation wasn't achieved until the

discovery of Q-switched laser in 1963. This kind of laser has the capability of producing high peak power laser pulse to generate plasmas, which symbolizes the birth of LIBS.

1.2.1 Fundamental of laser-induced breakdown spectrum

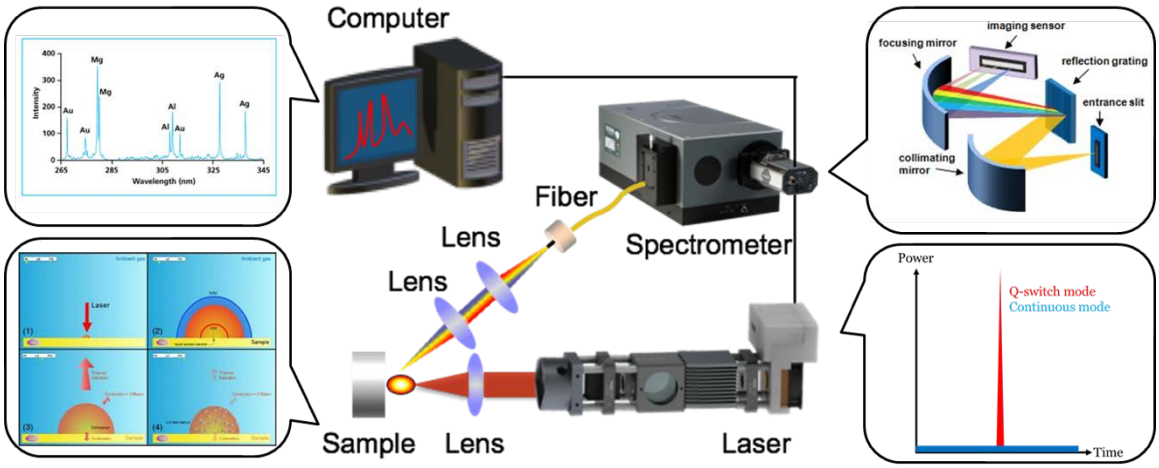

Figure 1.1 LIBS technique overview.

Figure 1.1 shows a typical setup of LIBS experiment. A LIBS measurement is carried out by first focusing an intense laser pulse on sample surface. This strong laser radiation will generate plasmas which contain characteristics atomic and ionic emissions. Such optical emissions will then be collected by lens into spectrometer which shows the signal's components in frequency domain. By analyzing these signals, the information on element composition can be obtained. Compared with other AES techniques that use adjacent physical devices (e.g. electrodes, coils, flame) as vaporization/excitation source, LIBS is more suitable as a remote sensing technique since laser can be easily focused onto far way target.

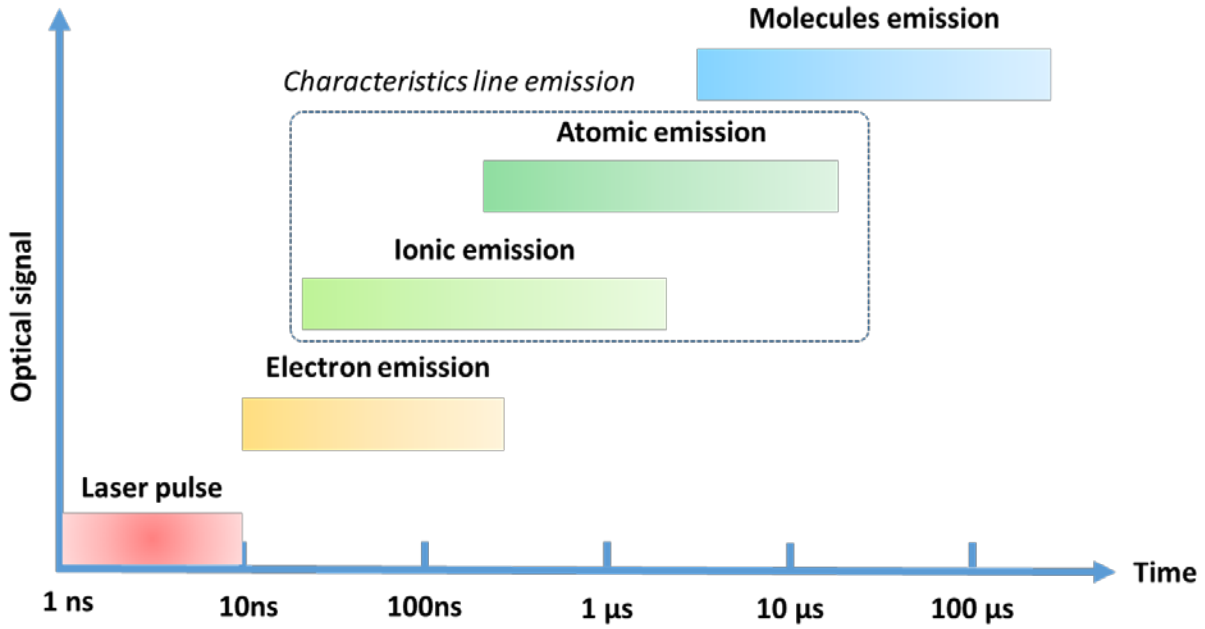

Figure 1.2 Time evolution of various optical signals in LIBS.

Since plasma is generated by a short laser pulse (~ns), its spectrum evolves rapidly in time. The temporal behavior of laser-induced plasma spectrum is illustrated schematically in Figure 1.2. At the very beginning, spectrum is dominated by a continuum background emission caused by Bremsstrahlung emission.[1] Such broadband emission doesn't provide any useful information on the sample element composition. After the continuum background disappears, characteristic ionic and atomic lines begin to show up. These shape line emissions come from the electron transition between various energy levels. They provide critical information on the element composition. Therefore, they are chosen to identify element in LIBS. As plasma further cools down, atom recombines and forms molecule which gives broadband molecules emission.

1.2.2 Methods to improve LIBS performance

However, a conventional LIBS using a single-pulse laser suffers from a relatively poor sensitivity with respect to other spectrometric methods. Since 1990s, several enhanced LIBS schemes have been studied to improve the sensitivity and reliability of the LIBS technique through temporal, spatial, and spectral engineering of plasmas interactions. These enhancement methods have been summarized in Table 1.1. These efforts have yielded significant success to improve the performance of LIBS.

Table 1.1 Methods to enhance LIBS performance.

Reference	Method	Advantages	Disadvantages	Field work
[5,7]	Double-pulse LIBS	10~100 times signal enhancement	Can't selectively enhance an emission line	Easy
[8-10]	LIBS-LIF	100~1000 times signal enhancement. Selectively enhance an emission line	Require expensive tunable laser and precision timing control.	Hard
[11,12]	Confined LIBS	10~50 times signal enhancement, simple setup	Can't selectively enhance an emission line	Easy
[13,14]	Spark discharge assisted	6 times signal enhancement	Require specialized instrument	Hard
[15,16]	Flame enhanced LIBS	4 times signal enhancement, simple setup	Can't selectively enhance an emission line	Easy
[17,18]	Microwave enhanced	20 times signal enhancement	Require specialized instrument	Hard
[19-21]	Effect of Atmospheric Conditions	Reduce background emission, 3~10 signal enhancement	Require specialized instrument	Hard

1.3 COMPACT LASER SOURCES FOR LIBS

As the performance of LIBS evolves in laboratories, there is increasing demand on the development of portable LIBS instruments for use in the field as stand-off sensing tools for harsh or dangerous environments.[3,22,23]

1.3.1 Compact laser sources review

In laboratory LIBS setup, commonly used laser sources are high power actively Q-switched flash lamp pumped Nd: YAG lasers which delivers nanosecond pulse with pulse energy ranging from 10 to 1000 mJ. These lasers not only are bulky due to their complex electronics and the need for effective cooling system, but also have very low wall-plug efficiency, making them unsuitable as portable laser sources. For a field-portable LIBS system, compact, high efficiency, and highly reliable laser should be used. Over the last decade, a number of miniaturized solid-state lasers have been demonstrated to deliver sufficient laser pulse energy with necessary peak intensity to perform LIBS analysis. The detail is listed in Table 1.2. Among these lasers, diode pumped solid-state laser offers the best overall performance.

Table 1.2 Overview of portable LIBS lasers.

Reference	Laser	Type	Performance
[24]	Kigre MK-367	Passive Q-switch solid-state laser, flash lamp pump	15 mJ/Pulse, 4 ns
[25]	Ultra CFR, Big Sky Laser	Actively Q-switched laser, flash lamp pump	50 mJ/Pulse,
[26]	SPI Laser	Passive amplified fiber laser	0.5 mJ/Pulse, 15~200 ns
[27]	JDS Uniphase	Diode-pumped passively Q-switched laser (Mircochip laser)	0.007 mJ/Pulse
[28]	Customized	Flash-lamp pumped actively Q-switched laser	45 mJ/Pulse, 4.5 ns
[29]	Customized	Passively diode-pumped passive-Q-switched laser	8 mJ/Pulse, 6 ns

1.3.2 VCSEL end pumped Q-switched laser

Recently, a new class of high-power VCSEL devices have been developed as laser pump sources. Comparing with the edge-emitting laser stacks, VCSEL have high efficiency (>40%).[30] The narrow linewidth of VCSEL (1 nm, FWHM) enables strong and resonate absorption of Nd: YAG crystal.[31] These two factors guarantee a high overall electrical-to-optical efficiency of the lasers. The cooling scheme for the VCSEL chip is straightforward. This ensures a far smaller overall packaging size than those of edge-emitting laser stacks, making them suitable as a pump source for compact lasers. VCSEL also have a uniform output profile, which enable good laser beam profile. [4]

To explore the application of compact laser sources for LIBS application, we developed several compact laser sources for LIBS applications. The first one is a compact actively Q-switched laser pumped by VCSEL. It operates at the wavelength of 1064 nm with a maximum pulse energy of 12.9 mJ. The second laser is a compact field-portable double-pulse laser system

that can dramatically improve LIBS performance. The third laser is a compact passively Q-switched laser enabled by additive manufacturing.

1.4 LASER ENABLED BY ADDITIVE MANUFACTURING

3D printing technology, known more formally as additive manufacturing, has been developing very fast in recent years, attracting much attention in both the industry and academic society. It has been used in such fields as industrial prototyping[32], bone tissue in medical research[33], specialized electronic[34,35], and reaction ware for chemical synthesis and analysis[36]. However, this technology has not yet been addressed in manufacturing laser systems, which remains largely unchanged since its founding. For a typical laser system, many discrete mechanical mounts and stages are bolted individually on a laser platform, making it sensitive to mechanical disturbance. To ensure a stable operation, solid and heavy material is used for construction. However, the use of heavy material is the most primitive and least effective way to ensure mechanical stability, adding unnecessary weight to the laser system. Besides, traditional manufacturing methods place restriction on the geometry of the laser system, which limits the design of laser systems.

Motivated by the idea that 3D printing offers many advantages over traditional manufacturing methods [37] by revolutionizing the way that materials turned into functional devices, we aim to improve laser manufacturing process by introducing 3D printing. First, the laser designs are no longer limited by commercial-off-the-shelf mechanical components. Many mechanical designs can be implemented to reduce the size and weight and to improve functionality, which are particularly useful for portable laser systems. Furthermore, the additive layer-by-layer approach enables multiple laser components to merge into a single solid piece, not only reducing the

requirement of post-machining and assembling, but also improving the rigidity of laser systems. Moreover, the modification of laser designs can be easily achieved digitally using computer-aided design (CAD) software, and the modified design can be manufactured using the same 3D printing process. Thus, diverse and distinct scientific needs can be met without incurring additional manufacturing cost.

Here, we explore the possibility to develop laser system using 3D printing technology. The entire laser frame is built as a single aluminum piece, featuring advanced mechanical and thermal designs. Passive air cooling and active water cooling mounts based on cellular structure are built into the frame. Meanwhile, two adjustable flexure optical mounts are printed for laser cavity alignment. The laser can deliver a maximum output energy of 9 mJ with pulse width of 12 ns. Our results pave the way towards manufacturing laser system using 3D printing technology

2.0 COMPACT VCSEL END-PUMPED Q-SWITCHED LASER

In this chapter, we describe the development of a compact actively Q-switched Nd: YAG laser end-pumped by a high-power VCSEL chip. The design of this compact laser and its performance were also studied. The laser operates at the wavelength of 1064 nm with a maximum pulse energy of 12.9 mJ. The repetition rate can be varied from 1 to 200 Hz. The laser performance including output power, pulse width, timing jitter, pulse stability and Q-switch delay were studied. Figure 2.1 shows the photo of laser with its controller.

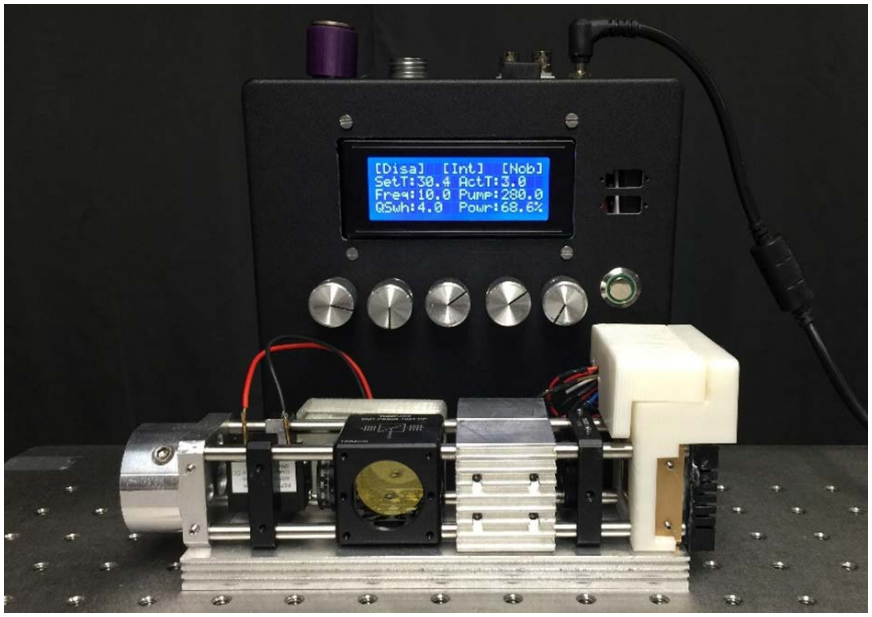

Figure 2.1 Photo of compact VCSEL pumped Q-switched laser system.

2.1 LASER SYSTEM OVERVIEW

Over the last decade, several miniaturized solid-state lasers have been demonstrated to deliver sufficient laser pulse energy with necessary peak intensity to perform LIBS analyses.[3] Most of these laser systems are Q-switched solid-state lasers. Besides the laser performance itself, dimension, weight, and efficiency are the key requirements for portable laser applications. Despite advances in these compact laser sources, some compromises must be made. For example, microchip lasers usually have low pulse energies and work in the passively Q-switch mode, making them inappropriate to perform time-resolved measurements due to their poor jittering.[27] In order to achieve a breakdown threshold using microchip lasers, tight focusing is essential, which drastically reduces the stand-off distance. Compact flash-lamp pumped lasers, on the other hand, have high pulse energies and can be synchronized with spectrometers to perform time-resolved measurements. However, pumping with a spectrally wide flash lamp is not as efficient because most of the pumping energy is turned into heat instead of pumping the gain medium. A more energy-efficient pumping scheme is the diode laser pumping enabled by high-power edge-emitting diode laser stacks and vertical-cavity surface-emitting lasers (VCSEL).

Both side and end pumping schemes have been used to achieve lasing using diode pump lasers. However, the end pumping scheme has been widely used for compact solid-state lasers for its high-energy absorption efficiency. The pumping light profile can be adjusted to coincide with the cavity resonator mode to yield good laser beam quality.[38] Recently, a new class of high-power VCSEL devices have been developed as laser pump sources. Comparing with the edge-emitting laser stacks, VCSELs have high efficiency (>40%).[39] The narrow linewidth of VCSEL (1 nm, FWHM) enables strong and resonate absorption of Nd: YAG crystal.[40] These two factors guarantee a longer running time when powered by battery. The cooling scheme for VCSEL chips is

straightforward. This ensures a far smaller overall packaging size than those of edge-emitting laser stacks, making them suitable as a pump source for compact lasers. VCSELs have a uniform output profile, which enable good laser beam profile. Because of these advantages, VCSEL laser chips have become popular pumping sources for compact solid-state laser developments and applications such as mid-IR conversion[41] and laser spark plugs[42].

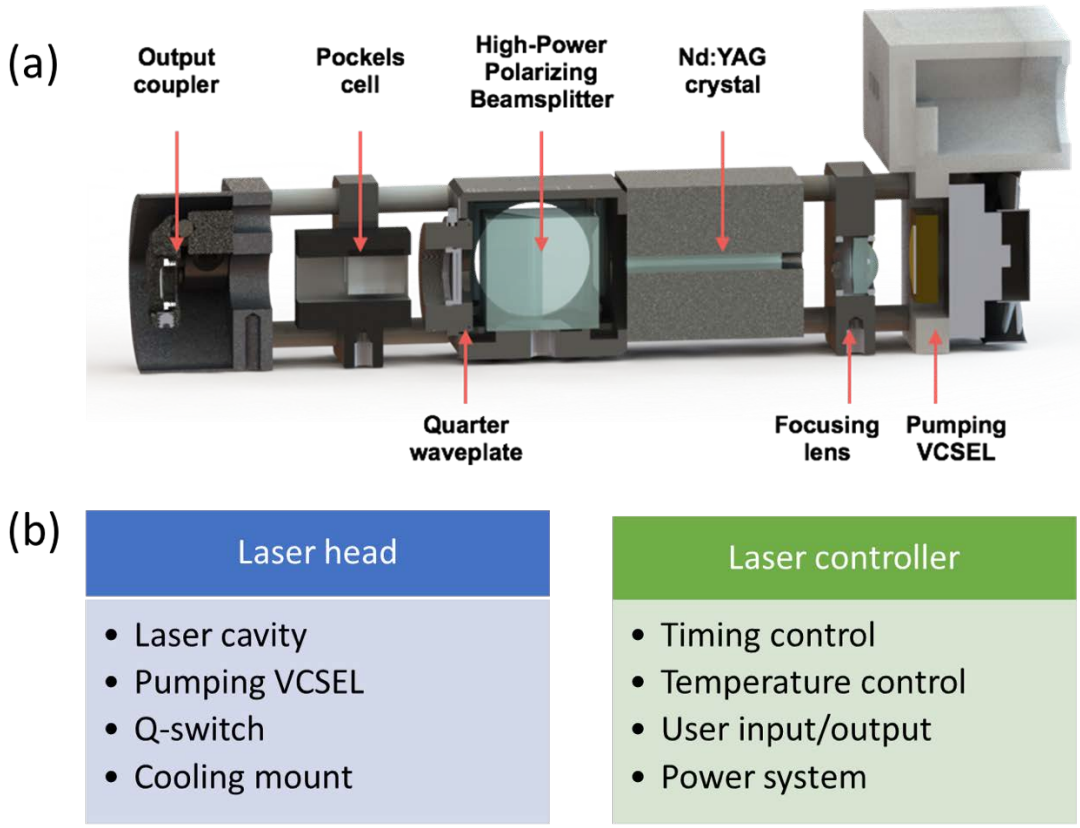

Figure 2.2 Laser system overview (a) Schematic of laser head, (b) Overview of laser head and controller.

Here we describe the development of a compact actively Q-switched Nd: YAG laser end-pumped by a high-power VCSEL chip as shown in Figure 2.2. To our best knowledge, this is the first time such type of laser is utilized in LIBS applications. The compact laser system is consisted

of two parts, a laser head and a laser controller, the system overview of which can be found in Figure 2.2 (b).

2.2 LASER OPTICAL DESIGN

Laser optical design (laser head) can be divided into four section, laser cavity, pumping VCSEL, Q-switch and cooling system. It weighs about 0.7 kg. The length of its cavity is about 14 cm. All opto-mechanic components of the lasers are housed in a 30 mm cage system

2.2.1 Laser cavity design

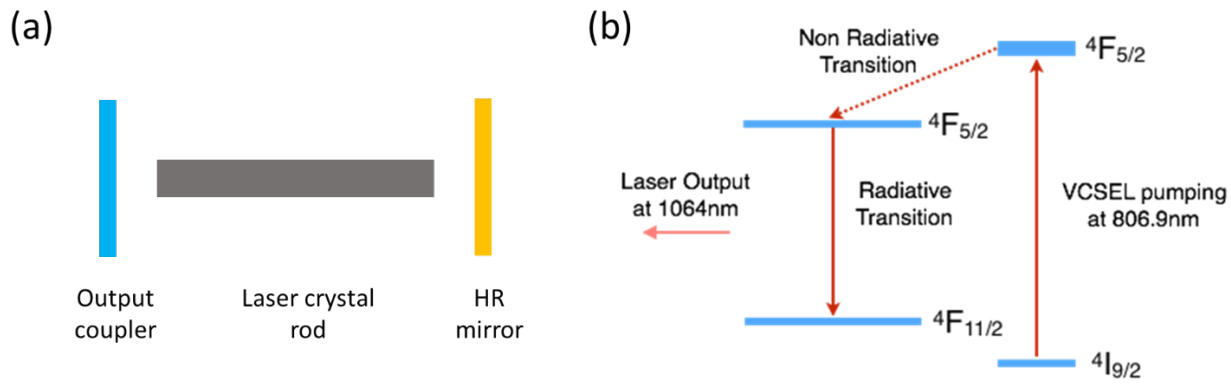

Figure 2.3 Schematic of laser cavity and energy level of gain medium (a) Schematic of laser cavity, (b) Schematic of Nd: YAG energy level.

Figure 2.3 (a) shows the schematic of laser cavity that features a "plane-parallel" design[38], where two ends of laser cavity are flat. The major advantage of this design is output beam has a good M^2 number. But such cavity is very sensitive to misalignment. There is a trade-off between output

beam quality and robustness of laser cavity. For LIBS applications, especially those stand-off measurement, a good output beam quality is preferred. Therefore, we choose the beam quality over robustness of laser cavity. At the same time, we will improve the robustness of laser cavity by using a more stable optomechanical design.

The gain medium used here is a Neodymium-doped yttrium aluminum garnet (Nd: YAG) crystal rod. Nd: YAG crystal is by far the most commonly used solid-state laser gain medium because of its unique properties favorable for laser operation. The YAG itself has both a good optical quality and a high thermal conductivity. Its structure is very stable against high temperature up to the melting point. The hardness and strength of YAG are also very good for fabrication. The active ion is the Nd^{3+}, a trivalent rare earth ion. In our laser system, the $4F_{3/2} \rightarrow 4I_{11/2}$ transition[38] is used with transition wavelength centered at 1064 nm as shown in Figure 2.3 (b). This is the transition with the highest emission cross sections. The absorption band is around 808 nm which has been chosen as the pumping wavelength. The upper-level lifetime is about 230 μs that is much longer than the upper-level lifetime (~10ns) of pumping VCSEL. This long upper-level lifetime allows Nd: YAG laser to work in Q-switch mode, where pumping VCSEL can only works in quasi-continuous-wave mode. Commercially available Nd: YAG crystals are grown exclusively by the Czochralski method with limited crystal size. In our application, the crystal is 40 mm in length and 4.3 mm in diameter. The curved cylinder surface is roughly grinded to reduce reflection which will reduced feedback in the radial direction. Therefore, the feedback can only be achieved in the axis direction. The two flat cylinder surfaces are finely grinded to a mirror finish and then coated with anti-reflection or anti-transition coating layers. Since our laser is end pumped, one flat surface of the crystal rod is coated with high transition for 808 nm pumping wavelength and high reflection

for 1064 nm lasing wavelength. On the other flat surface, the crystal is only coated with high transition for 1064 nm lasing wavelength.

2.2.2 VCSEL end-pumping

As pumping source, VCSEL array, shown in Figure 2.4 (a), belongs to the family of surface emitting semiconductor lasers where laser beam emission is perpendicular from the top surface. Figure 2.4 (b) shows that VCSEL laser resonator consists of two distributed Bragg reflector (DBR) with active gain layer in between. The wavelength can be tuned by adjusting the DBR. The VCSEL used in our experiment outputs a wavelength of 808 nm that falls in the center of Nd: YAG crystal absorption band. Since the cavity length of VCSEL is very small, the out power of a single VCSEL is quite limited. To achieve high out power, VCSEL array that contains lots of single VCSEL units is used as pump source. In quasi-continuous-wave operation, as shown in Figure 2.4 (c), total pump energy equals pump power times pump time. In our application, the VCSEL arrays can inject a pulse energy up to 240 mJ into gain medium at a time interval of 300 μs with peak power of 800 W.

For solid-state lasers, many different optical designs have been proposed to effectively transfer energy from pumping source to gain medium. Figure 2.4 (d) shows two major pumping geometries, side pumping and end pumping.[43] For side pumping, the pump light is injected into gain medium from the side, a direction that is perpendicular to the laser beam. The key advantage is that it allows the use of pump sources with very low spatial coherence such as flash lamp. Besides, multiple pump source can be combined in side pump thus offering a high output power. For these reasons, side pumping is mostly used in high power solid-state lasers. However, high gain, good beam quality and high-power efficiency are very difficult to obtain in side pumping.

This is because gain at the edge of laser modes, leading to a poor extraction efficiency and encouraging high-order lasing mode.

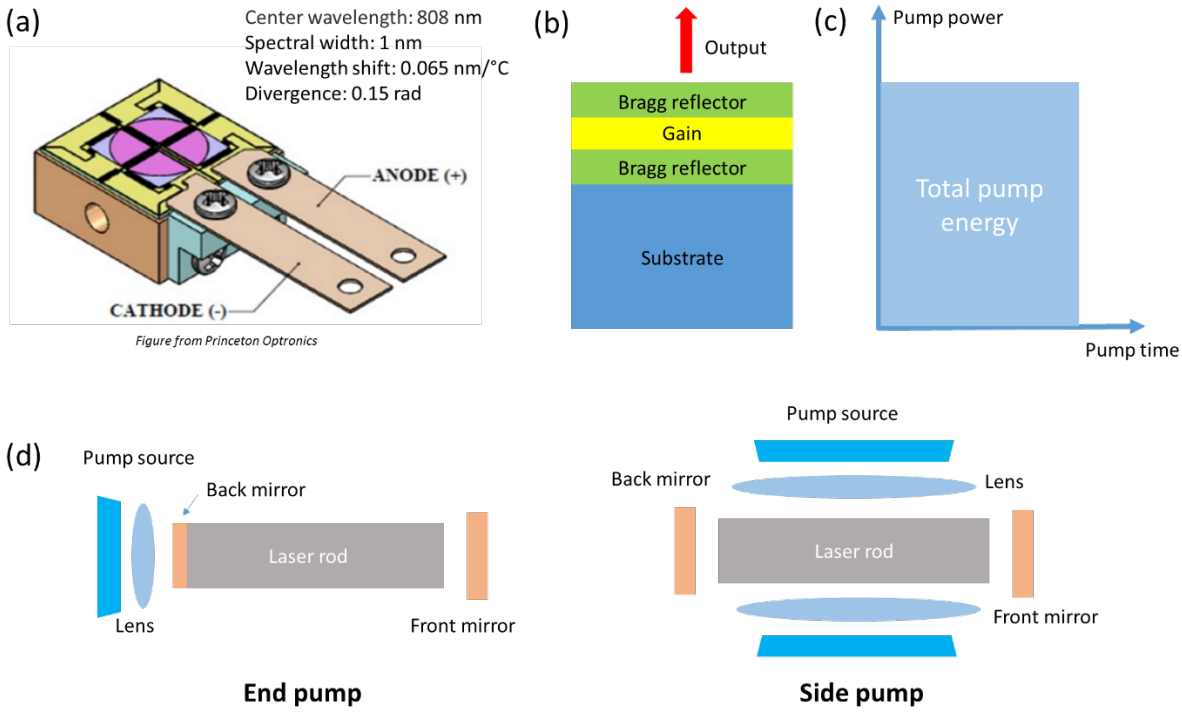

Figure 2.4 Laser pumping system. (a) Schematic of VCSEL array, (b) Schematic of a single VCSEL, (c) Pumping chart, (d) Schematic of end pump v.s. side pump.

In end pumping, the pump light is injected along the laser beam. The pump beam is usually focused by a lens on laser end-face where pump beam can overlap with lasing mode of laser resonator. In this case, higher-order modes have very low gain compared with fundamental mode. Thus, single mode operation is often possible. High power efficiency can also be achieved. The limitation of end pumped is that the pump light can only be injected through two end faces, which limits the laser output power.

Another factor to be considered here is cooling. In Nd: YAG laser crystal, about 40% of the pump energy will be converted into heat.[38] Temperature gradient will cause thermal lensing in

laser crystal. Strong thermal lensing effect will cause the breaking up of the lasing mode. For side pumping, cooling is complicated since the side of laser crystal is not only used for pumping but also for cooling. It is very difficult to design a compact device that can effectively cool laser crystal. For end pumping, on the other hand, only two crystal end faces are used for pumping, the side of laser crystal can be used for effectively cooling. This allows laser to be made in a very compact size. Since our laser will be used for field application where high energy efficiency and compactness are preferred, end pump configuration is chosen.

2.2.3 Actively Q-switch based on polarizing device

Q-switching is a technique to obtain high energy pulses from lasers by modulating the Q-factor of laser resonator. The Q factor (quality factor) is a measure of the strength of damping cavity energy. It is defined as 2π times the ratio of the stored energy to the energy dissipated per oscillation cycle. In our laser, shown in Figure 2.5 (a), the Q-switch is based on polarizing devices consisted of a Pockels cell, a 1/4 wave-plate and polarizing beam splitter.

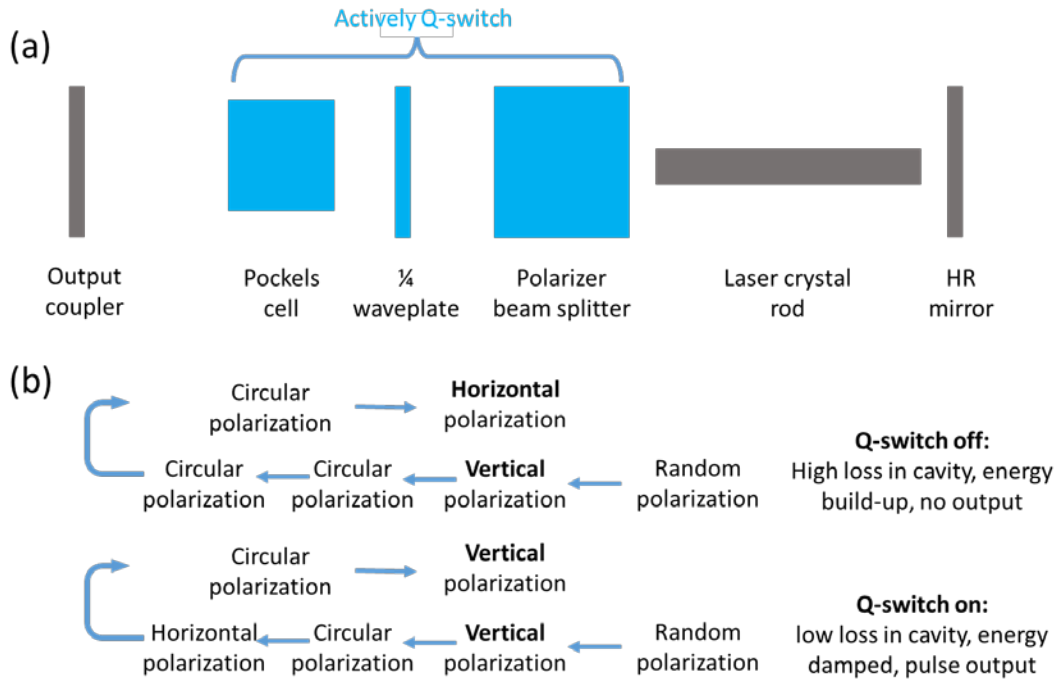

Figure 2.5 Laser Q-switch system (a) Schematic of actively Q-switch within in laser cavity, (b) Working principle of Q-switch.

When VCSEL starts to pump the laser crystal, the Q factor is kept low. Light emitted from laser rod is linearly polarized by the polarizer. When it will pass the ¼ waveplate twice after reflected from mirror, the polarization will be rotated by 90 degrees. Thus, it won't pass the polarizer and no feedback will be formed. When enough energy is stored in laser crystal, a voltage will be applied to the Pockels cell, the total polarization will be rotated by 180 degrees. Thus, it will pass the polarizer and the feedback will be formed. At this moment, the Q factor is very large. The pulse energy will build exponentially from spontaneous emission. A strong pulse with narrow pulse width will be emitted. The entire process is shown in Figure 2.5 (b).

2.2.4 Laser thermal management

Figure 2.6 shows the laser thermal management system which can be divided into two parts, passive crystal cooling and actively VCSEL cooling. For Nd: YAG crystal, about 40% of the pump power will be converted to heat[38], causing its temperature to increase. The increased temperature may not damage crystal itself, but will cause thermal lensing effect that will compromise laser performance.[38] Besides, if heat can't be dissipated effectively, the crystal mount will expand unevenly because of end pumping, leading to cavity misalignment. A heavy-duty laser crystal mount made from Aluminum with integrated fin structure is used to effectively dissipate heat.

The pumping VCSEL has an efficiency of 30% at its full power of 800 W and a pumping duration of 300 μs. Therefore, 1.4 J heat will be generated when it works at 10 Hz. If such amount of heat can't be dissipated effectively, VCSEL temperature will increase 2.24 °C each minute. Even if VCSEL itself can be operated at a high temperature up to 80 °C, inappropriate thermal management can lead to wavelength shift and even the breakdown of VCSEL. In our application, an actively temperature control system based on Peltier cell was developed. It features a close-loop design that can maintain VCSEL temperature at 30°C at normal working condition. The proportional-integral-derivative (PID) control constant in the temperature controller was optimized for this application.

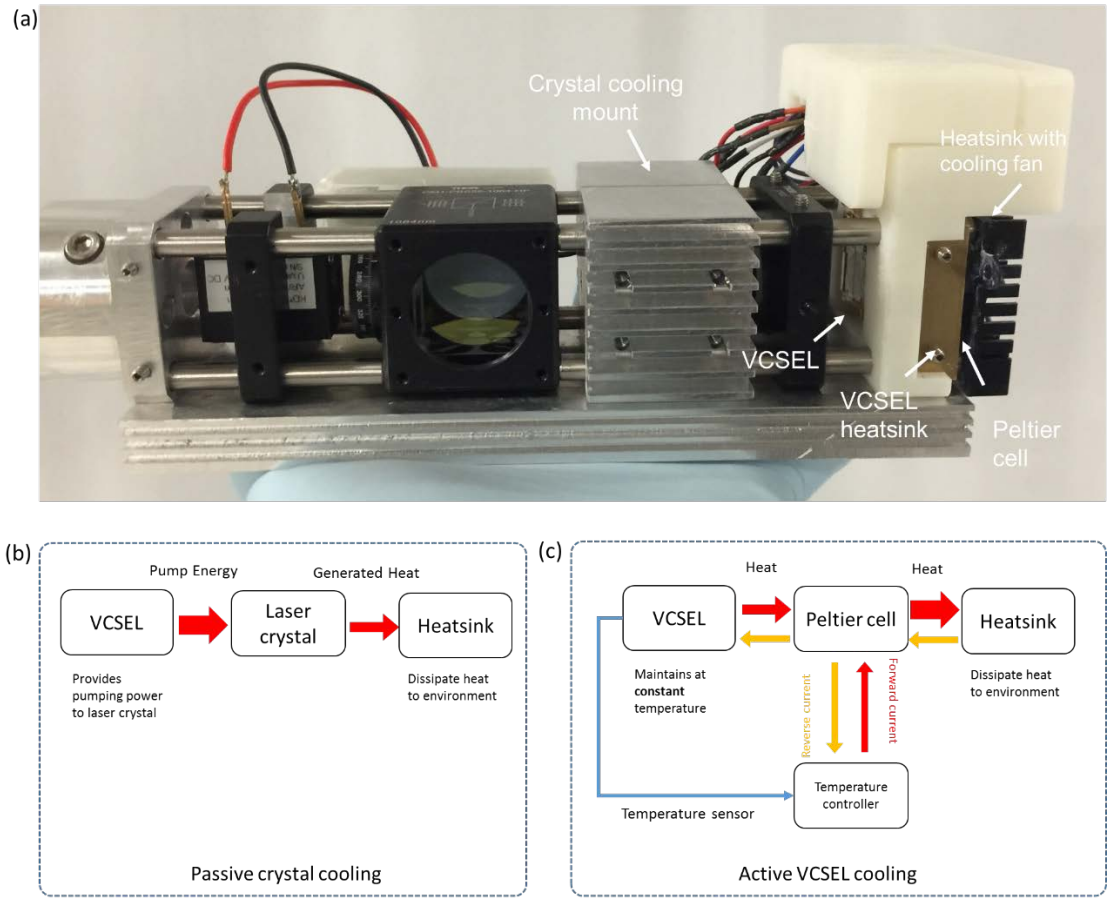

Figure 2.6 Laser cooling system (a) Photo of laser passive and active cooling systems, Working principle of (b) passive and (c) active working systems.

2.3 LASER ELECTRICAL DESIGN

The electrical part of laser system (laser controller) has a dimension of 80 mm × 200 mm × 200 mm and a weight of 2.5 kg. It is equipped with some user-interface electronics (screen, knobs, and buttons) and contains all the associated electronic components such as VCSEL drivers, timing control and temperature control system. The whole system is powered by 24 V DC, making it suitable for field application. All the electrical components are commercially available. A PCB

board hosting all these components was designed and built. The software development was based on an open source platform called Arduino.

2.3.1 Timing control system

The successful operation of an actively Q-switched laser depends on precise timing. The VCSEL pumping signal and Pockels cell triggering signal must be precisely synchronized. To achieve optimized laser performance, the electrical signal should have low jitter and high resolution. The chip used here is a 16 MHz, 8-bit ATmega328 microprocessor that has a time resolution of 62.5 ns with +/- 5 ns jitter. The Arduino microcontroller (ATmega328) has a 16-bit built-in timer that has three output ports. One of them was used to trigger VCSEL, while another was used to trigger Pockels cell. This timer is the heart of controlling laser timing. The clock source from the internal clock sends pulses to the pre-scaler which divides the pulses by a determined amount. For a 16-bit timer, the maximum count is 65536. If the minimum step is set at 62.5 ns, the maximum laser period will be 4 ms, which is too small. The period should be 100 ms for our experiment. Therefore, we need to set the pre-scale on the timer, which will extend the period to 100 ms. There are several working modes in the timer. CTC mode is chosen here. Figure 2.7 (a) and (b) shows a timing chart of Q-switch process and its corresponding electrical triggering signal. Figure 2.7 (c) shows the photo of microcontroller with two signal pins from Timer 1 indicated in red arrow.

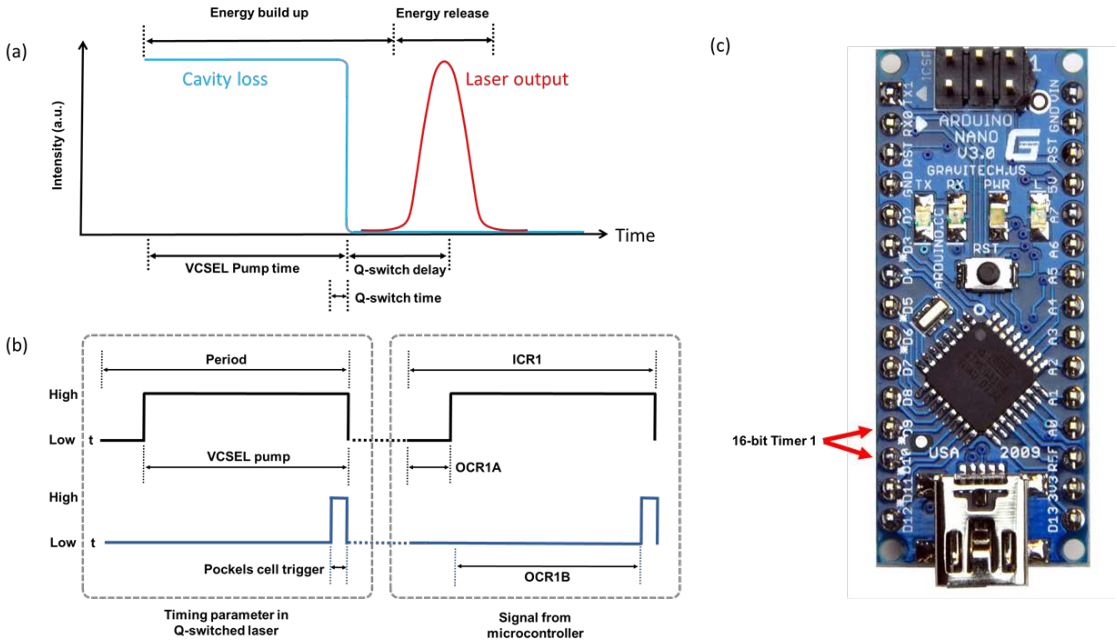

Figure 2.7 Laser timing control system (a) Timing chart of Q-switch, (b) Timing chart of triggering signal, (c) Photo of microcontroller.

2.3.2 Temperature control system

Since the output wavelength of VCSEL depends on temperature, it is crucial to maintain a constant VCSEL temperature. The core of temperature control system is the temperature controller (HTC 4000, wavelength electronics), as shown in Figure 2.8. A single resistor sets the maximum output current. A potentiometer (10K) was used to control the temperature set point. A thermistor was used to measure the temperature. A Peltier cell was used to heat or cool the VCSEL depending on the difference between real and set temperature. By calculation, a 10 KΩ resistor and 5 µF capacitor was chosen to set the PID constant. The detailed pin mapping can be found in Figure 2.8 (a).

(a)

Pin	Function
1	5 k resistor for limiting maximum output current
2	
3	Connect to pin 2, allow bipolar operation
4	Volt reference
5	Measurement ground
6	Actual temperature output
7	Setting temperature output
8	Voltage input
9	Supply voltage input
10	Ground
11	Peltier cell (+)
12	Peltier cell (-)
13	Thermistor
14	Thermistor
15	10 k resistor sets sensor current to 126 µA
16	
17	10 k resistor sets proportional gain
18	
19	5 µF capacitor sets PID time integration constant
20	

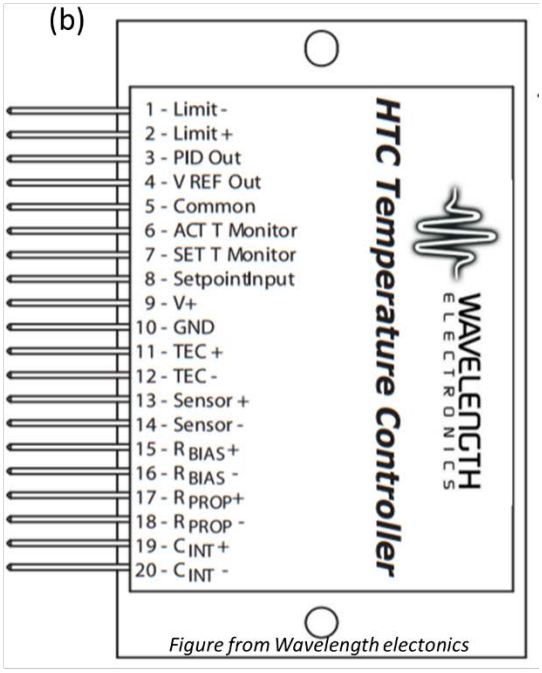

Figure 2.8 Laser temperature control system (a) Pin map of temperature controller (b) Schematic of temperature controller.

2.3.3 User input and output system

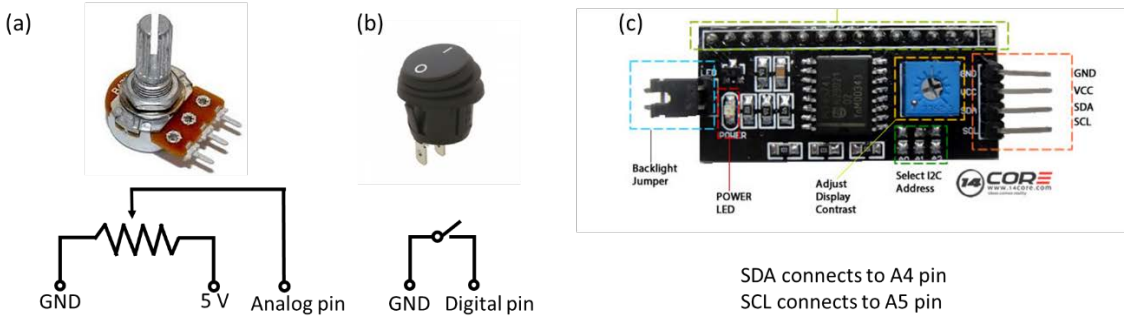

Figure 2.9 User input/output system (a) Potentiometer, (b) Switch, (c) LCD controller.

The laser controller has a user-friendly interface including knobs, switches and an LCD, the details of which can be found in Figure 2.9. Figure 2.9 (a) shows a potentiometer that is used to set laser

VCSEL temperature by changing its resistance. This potentiometer is also used to change laser parameters such as frequency, pumping time and Q-switch time as well. Here the center output pins are connected to the analog input of microcontroller, which converted the 0 to 5 V input voltage to 1 to 1024 digitalized value. These values are then used to set laser parameters. For setting laser output power, the laser diode driver needs analog input instead of digital input. A voltage divider is designed with the potentiometer which can output 0 to 12 V to set the laser output power from 0 to maximum. A push button, as shown in Figure 2.9 (b), is used to turn laser on. It is not only connected to the laser diode driver but also connected to the microcontroller's digital input. When the button is pushed down, its output voltage will change from 0 to 5 V. So, the microcontroller will be notified and updates the display to user. All system's working parameters are displayed in the LCD screen.

The software is developed using Arduino, an open source platform. The code is written in C++. The program can be divided into two parts, an initial setup function and an infinite for-loop. In the setup function, the system will be initialized. In the for-loop, the system will not only read system parameters and display them to user on the LCD screen, but also change system parameters accordingly.

2.3.4 Laser power system

One major advantage of our laser system is that it runs at 24 V DC, making it a good candidate as field-portable device when powered by battery. Unlike flash lamp driver that usually require 220 VAC, our VCSEL driver is powered by 24 V DC. A 24 V to 5 V DC convertor is used to drive microcontroller, temperature controller and Pockels cell driver that all run at 5 V. The schematic of laser power system is shown in Figure 2.10.

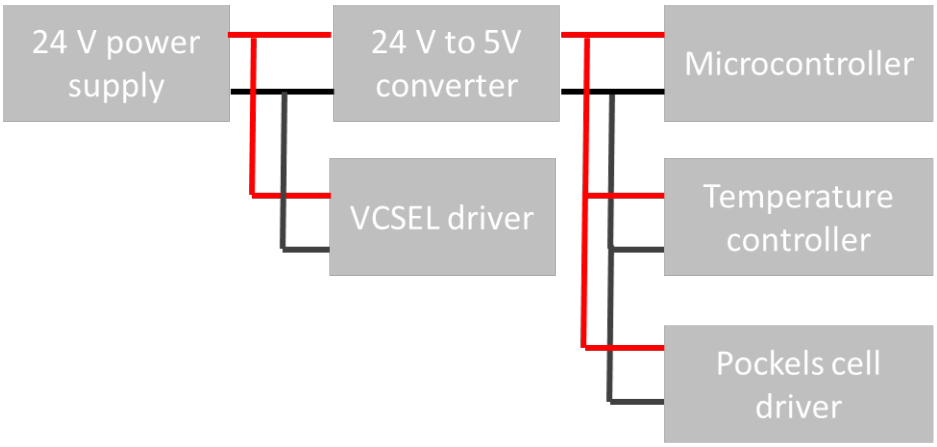

Figure 2.10 Schematic of laser power system**.**

2.4 LASER PERFORMANCE

In this section, laser performances were studied in terms of output power, Q-switch delay, pulse width and pulse stability.

2.4.1 Output power and Q-switch delay

The laser output power was first studied at various pump conditions with the laser running at 10 Hz. The output power was measured using a thermal power meter (Thorlabs, S302C). As is shown in Figure 2.11 (a), the laser output power was characterized at different pump powers and durations. The pump threshold was measured at 130 W. After reaching the pump threshold, laser output power increases with the pump power and the slope also increases with the pump duration. The maximum output power of laser is limited by the electronics used to power VCSEL, which was capped at 425 W or 53% of the maximum output power of the VCSEL. This yields a maximum output pulse energy of 12.9 mJ/pulse.

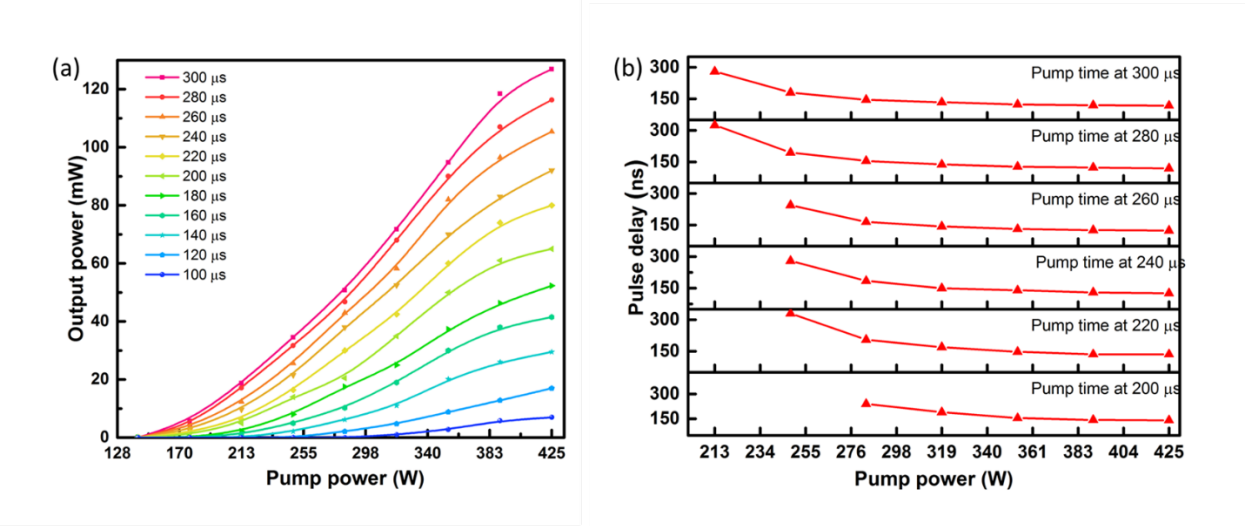

Figure 2.11 (a) Output power v.s. pump power at various pump durations, (b) Q-switch delay v.s. pump power at various pump durations.

An important parameter of the actively Q-switched laser for time-resolved LIBS measurements is the Q-switch delay, which is defined as the delay between the triggering time of the Pockels cell and the moment when the laser cavity emits a laser pulse. This is presented in Figure 2.11 (b), where the Q-switch delays were measured for the VCSEL pump durations from 200 to 300 μs with pump powers ranging from 213 to 425 W. The Q-switch delay times were found to be between 120 and 325 ns. At the peak pump power of 425 W, the Q-switch delay time reduced to a minimal of 120 ns at a pump duration of 300 μs. When pump duration was decreased to 200 μs, the minimal Q-switch delay was measured as 136 ns. The result obtained here was used to calibrate synchronization between the laser and spectrometer when performing LIBS experiments.

2.4.2 Pulse width measurement

Laser pulse width was also studied under various pump conditions. The laser pulse was attenuated using a high-power polarizer, a half wave plate, and a neutral density filter to avoid damaging photodiode. The attenuated pulse was then measured by a high speed InGaP photodiode (New Focus 1544-B) that connected to a digital oscilloscope with a bandwidth of 2.5 GHz (DPO7254, Tektronix).

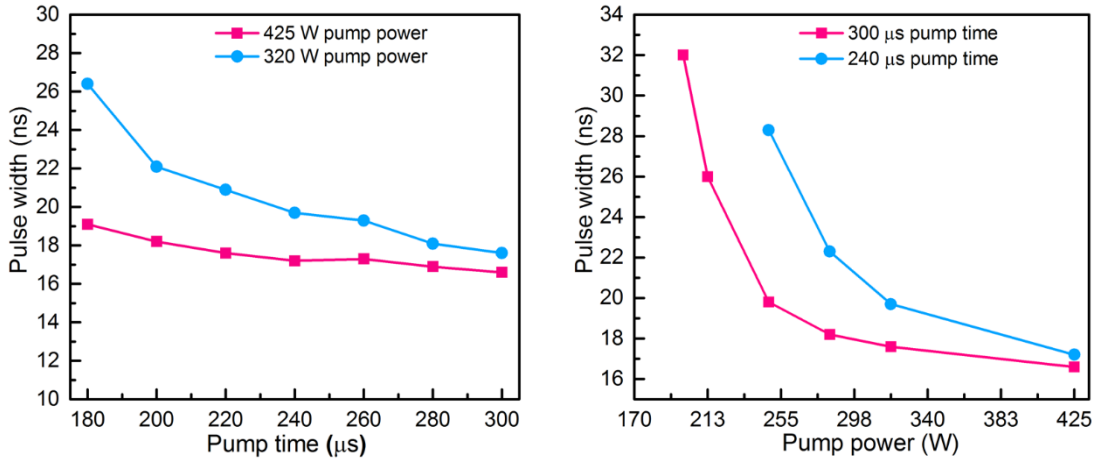

Figure 2.12 Laser pulse width measurement (a) Pulse width as a function of pump time at two different pump powers, (b) Pulse width as a function of pump power at two different pump times.

Pulse width as functions of pump durations at two different VCSEL pump power of 425 W and 320 W are presented in Figure 2.12 (a). Output laser pulse width decreased when the pumping duration increased from 180 to 300 μs. The pulse width was reduced to 16.6 and 17.6 ns, respectively. The output pulse width can be further reduced when the pump duration was increased. Figure 2.12 (b) shows the relationship between the pulse width and the VCSEL pump

power when the pump duration was set at 240 and 300 μs, respectively. For a fixed pump time, the pulse width decreases with increased pump power. Characteristics presented in Figure 2.12 is consistent with a previous report [28].

2.4.3 Laser stability measurement

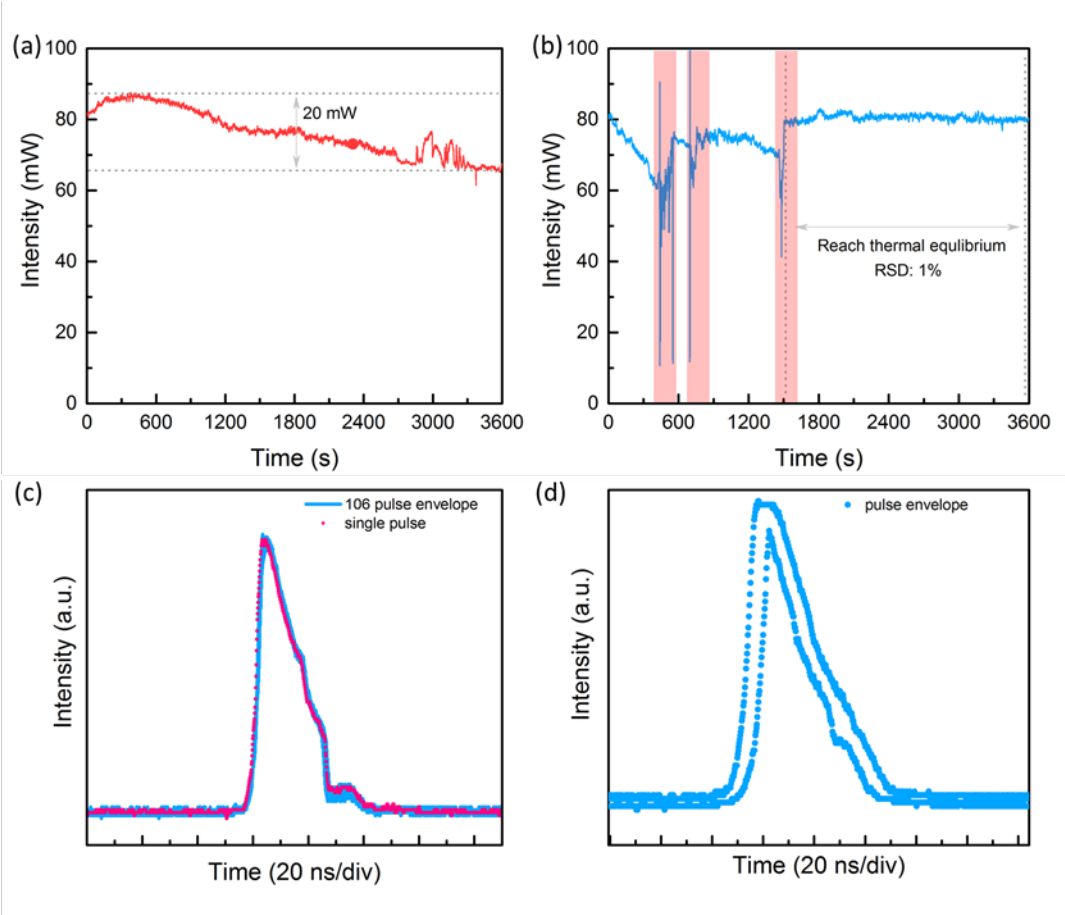

Figure 2.13 Laser stability measurement. (a) Output power stability test without alignment, (b) Output power stability test with realignment. Red shaded area shows where alignment happened. Room temperature was 22°C. Laser ran at 10 Hz, (c) Stability measurement of laser pulse by comparing the envelope formed by 106 pulses and a single pulse, (d) Laser timing jitter measurement by analyzing the pulse envelope formed by 106 pulses.

Laser output power stability is very important for a successfully LIBS measurement. A laser with low output power fluctuation can give more accurate and consistent LIBS results. To get a stable output power, not only the laser needs a stable electrical system, but also a rigid optomechanical build. Figure 2.13 (a) and (b) show laser output power as a function of time without and with re-alignment. Without realignment, the laser output power dropped to 75% of its maximum power, which is caused by the misalignment of laser cavity. However, if the laser cavity was realigned after laser cavity reached thermal equilibrium, the laser outpower was very stable with a relative-standard-deviation of 1% as shown in Figure 2.13 (b).

Laser shot-to-shot pulse stability and timing jitter are very important parameters to ensure reliable LIBS measurements. A stable pulse shape and lower timing jitter infer a high performance electrical design. Pulse stability was studied by recording continuous pulse shape as an envelope using the oscilloscope. A pulse envelope formed by 106 pulses was plotted in Figure 2.13 (a) (blue traces). It is compared with a pulse shape of a single laser shot (red dot). Result presented in Figure 2.13 (a) shows the peak intensity variation of 106 pulses are less than 1%, demonstrating that a high stability of the laser pulses.

The timing jitter measurement was shown in Figure 2.13 (b), where a 10 Hz signal from the microcontroller was sent to the oscilloscope channel 1 as trigger, while the pulse signal measured by the photodiode was fed to the oscilloscope channel 2. 106 continuous pulses were recorded to form a pulse envelope with the outline shown in blue dot. By studying the pulse envelope width, timing jitter was estimated to be ±2 ns, comparable to most commercial actively Q-switched lasers.

2.4.4 Fifth harmonic generation

To further test laser performance, we generated 213 nm laser light using three nonlinear crystals. A linear configuration was chosen to simplify the experiment setup, so a more compact system was developed. As show in Figure 2.14, laser beam with 1064 nm fundamental frequency passed through a type I second harmonic generation crystal. The second harmonic of 532 nm with perpendicular polarization was generated. Then such 532 nm laser beam passed a type II fourth harmonic generation crystal and a fourth harmonic of 266 nm was generated. Finally, the fundamental frequency and fourth harmonic were mixed at the fifth harmonic generation crystal, generating a fifth harmonic of 213 nm laser beam. Phase matching condition was achieved by rotating crystal along the tilting axis as shown in red.

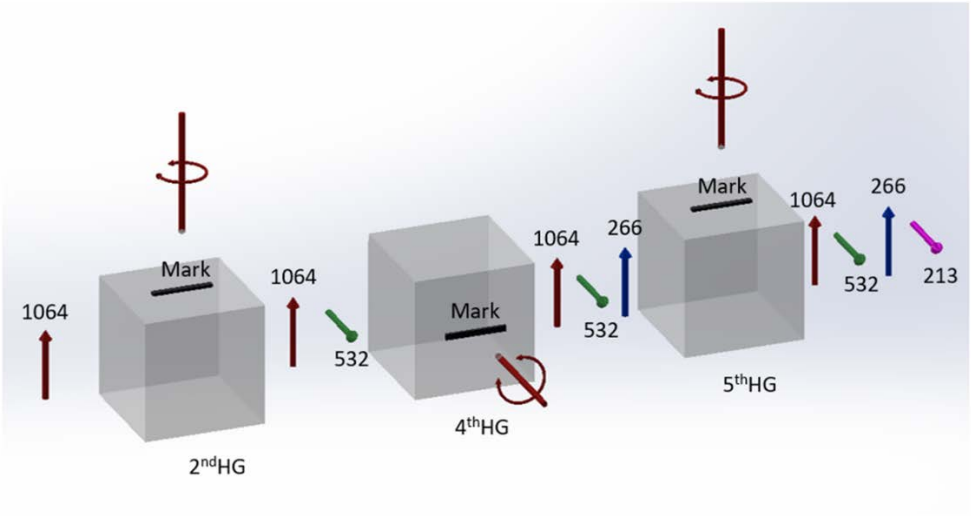

Figure 2.14 Schematic of fifth harmonic generation.

After the fifth harmonic generation device, there are four different wavelengths. To separate them, optical filter is not suitable since pulse energy is too high. Grating is also not

suitable, since grating will not only mess up beam quality but also not convenient for real world application. Therefore, a Pellin Broca prism made of UV fused silica is used. The fifth harmonic was successfully separated from other wavelengths based on total internal reflection and wavelength dispersion. UV fused silica is used to reduce absorption in UV wavelength range. If N-BK7 glass is used, the fifth harmonic is absorbed strongly. Almost no output can be detected. The details of pulse energy of the harmonic generations can be found in

Table 2.1. The final fifth harmonic generation efficiency is 1.25%, which is comparable to commercial lasers. Such high conversion efficiency is due to the high laser performance, especially the good beam quality.

Table 2.1 Pulse energy of various harmonic generations

Wavelength	1064 nm	532 nm	266 nm	213 nm
Pulse energy	80 mJ	20 mJ	2 mJ	1 mJ

2.5 LIBS EXPERIMENT RESULT

In this section, several LIBS experiments were performed to test our laser performance. The test results show that our laser is an effective and compact laser tool for laser remote sensing applications.

2.5.1 Experiment setup

The schematic of LIBS setup is shown in Figure 2.15. The compact laser operated at its fundamental wavelength (1064 nm) with a pulse repetition rate of 10 Hz. The output pulse had a pulse energy of 12.9 mJ and a pulse width of 16.6 ns. The Pockels cell's triggering signal was also used to synchronize with a spectrometer (Andor Tech., Shamrock 505i), which was equipped with an intensified charge coupled device (ICCD) detector (Andor Tech., iStar, DT-334T). The 120 ns Q-switch delay was considered for synchronization.

Table 2.2 Elemental concentrations (wt.%) of Mn and Cr in Al alloy sample.

	Standard Reference Materials (wt %)				
Elements	1255b	1256b	1240C	1258I	No.1259
Mn	0.0527	0.3857	1.2680	0.4810	0.0790
Cr	0.0150	0.0572	0.00054	0.0011	0.1730

The optical emissions from plasmas were coupled into a fiber bundle that connected to the spectrometer by two lenses (6 and 10 cm focal lengths). The reason to use two lenses instead of a single lens is to collect more light from plasma, because the effective light collection solid angle of double lenses system can be much larger compared with a single one. The laser beam was focused onto the sample surface by a single lens (20 cm focal length). The focused spot size is around 0.3 mm. The sample itself was mounted on a computer-controlled motorized stage that moved the sample during measurements to avoid over ablation. The sample used in this experiment is shown in Table 2.2.

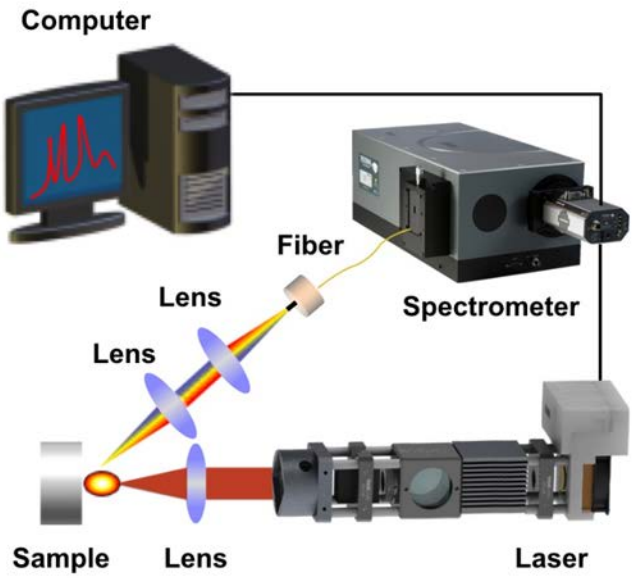

Figure 2.15 Schematic of LIBS experiment setup.

2.5.2 Signal stability test

Shot-to-shot stability of LIBS signal is an indirect reflection of variations in laser performance such as pulse energy stability and timing jitter. The laser pulse was focused on an aluminum alloy sample (NIST 1259) to generate plasmas. The strong Al 394.4 nm and Al 396.2 nm atomic emission lines were chosen to minimize the effect of inhomogeneity on precision. A series of 1000 sequential LIBS spectra were recorded to study the peak-to-base and peak-to-peak ratios. As can be seen in Figure 2.16 (a), the Al 396.2 nm peak-to-base ratios had a relative standard deviation (RSD) of 19%, which was comparable to a previous study[44] but obtained with only 10% of its pulse energy. This RSD was mainly determined by the target surface quality at the point of analysis. The peak-to-peak (Al 394.4/Al 396.2) atomic line emission ratios, as shown in Figure 2.16 (b), had an RSD of 3%. Both shot-to-shot signal stability tests above have demonstrated that our laser has excellent performance in terms of LIBS measurement repeatability.

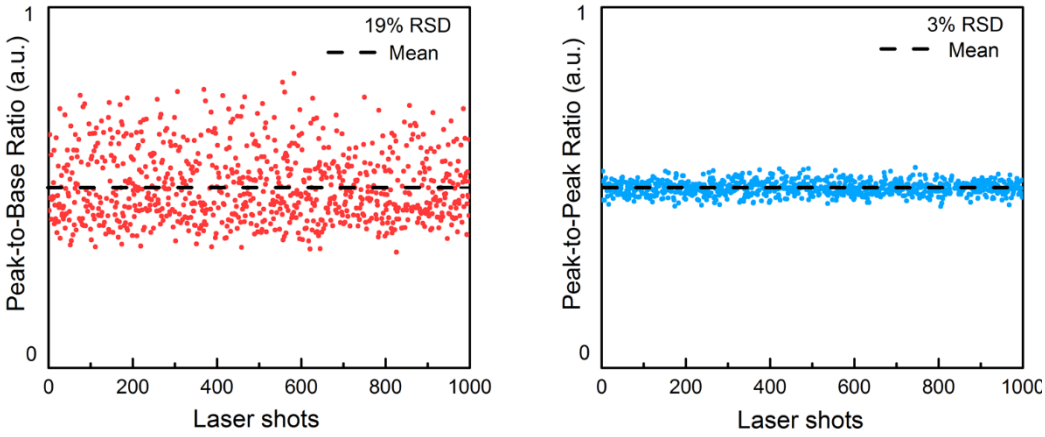

Figure 2.16 Shot-to-shot emission peak analysis. (a) Al 396.2 peak-to-base atomic emission ratios for a 1000-shot sequence, (b) Al 394.5/Al 396.2 peak-to-peak atomic emission ratios for a 1000-shot sequence. Each data point is represented by a red/blue dot. The black dash lines show average value.

2.5.3 Crater profile and ablation efficiency

The experiments were performed without using any spatial filter to optimize beam profile. The laser pulse was directly focused onto sample surface by a single lens (20 cm focal length). Craters formed by 10, 50, 100, 200, and 500 consecutive laser pulses on a stainless-steel sample (NIST 304) were studied using a scanning electron microscope (SEM) and a white light interferometric microscope (Zygo).

Table 2.3 Ablation efficiency.

Number of pulses	10	50	100	200	500
Ablation efficiency (μm^3/mJ)	1.76	0.52	0.42	0.20	0.20

SEM images of three craters formed by 100, 200, and 500 pulses are shown in Figure 2.17 (a, d, g), respectively, and the corresponding 3D images generated from the interferometric scope are shown in Figure 2.17 (b, e, h). The crater profiles obtained here were prominently cone-like because of the almost perfect Gaussian laser beam profiles.[45]

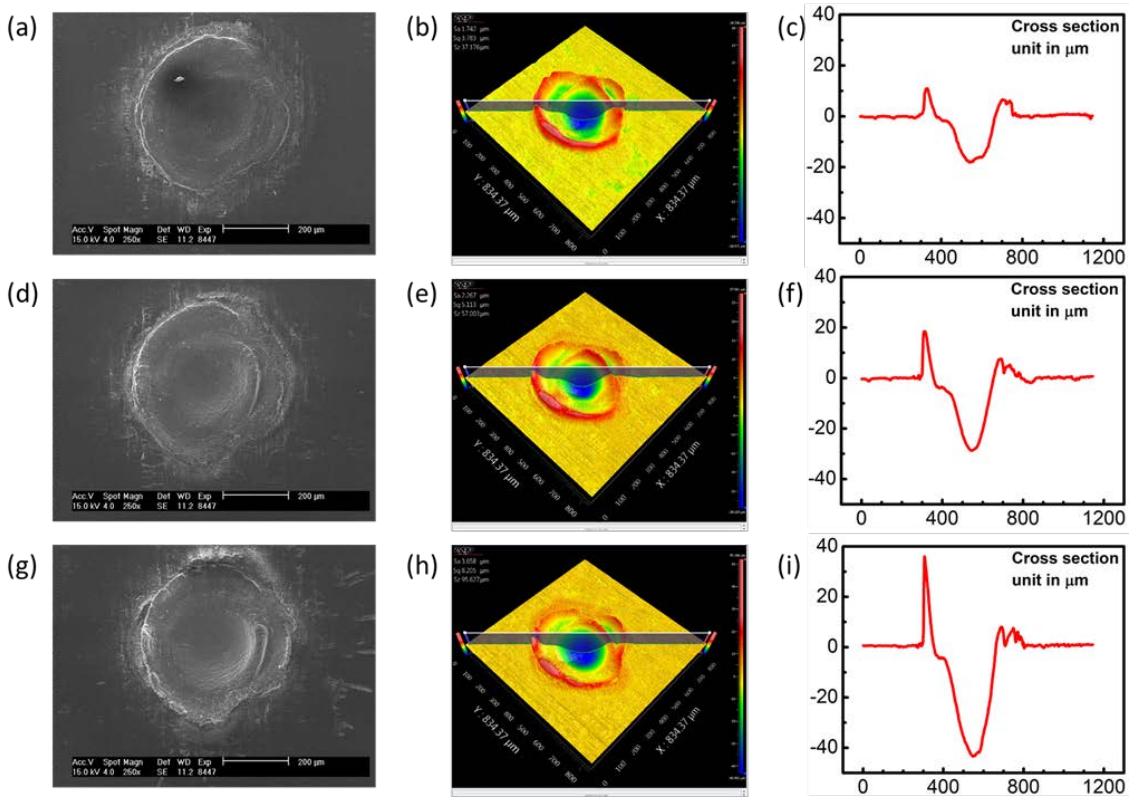

Figure 2.17 Craters created by different numbers of focused laser pulses. (a,d,g) SEM image of craters created by 100, 200 and 500 laser pulses, (b,e,h) 3D images of craters, (c,f,i) Craters cross sections obtained from 3D images.

The spike structures around the edge of the craters were formed by the recondensation of plasmas. Figure 2.17 (c, f, i) shows cross section views of these craters, which were then used to estimate the crater volumes. The ablation efficiency is defined as the ratio of the crater volume to

the laser pulse energy. The ablation efficiency of different numbers of pulses are shown in Table 2.3. As the number of pulses increased, the ablation efficiency decreased. The ablation efficiency from the first 10 pulses was about 1.76 um^3/mJ, which reduced to 0.2 um^3/mJ for 500 pulses.

2.5.4 Time-resolved emission spectra

Time-resolved measurements can provide a detailed diagnostic of the transient plasmas. Time-resolved emission spectra for an Aluminum alloy sample (NIST 1259) is shown in Figure 2.18, where Figure 2.18 (a) shows Mg ionic emission lines (279.6 and 280.3 nm) and Figure 2.18 (b) shows Al atomic emission lines (394.5 and 396.2 nm).

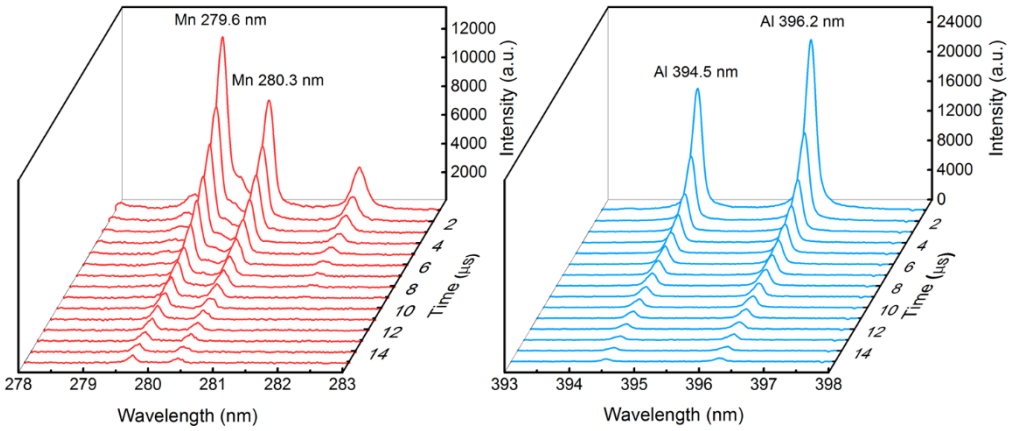

Figure 2.18 Time-resolved emission spectra of an Al alloy sample. (a) Mg ionic line with gate width set at 100 ns, (b) Al atomic line with gate width set at 1000 ns. Each spectrum was averaged over 30 pulses.

A monoexponentially temporal behavior was observed for the emission peak intensity. An exponential curve fitting algorithm was used to calculate the lifetime of each peak. [1] The lifetimes

of 279.6, 280.3, 394.5, and 396.2 lines were calculated to be 0.66±0.048, 0.62±0.023, 1.67±0.11, and 1.62±0.11 μs, respectively. The plasma lifetimes obtained here were at least a thousand times longer than those obtained by a microchip laser[27].

2.5.5 Electron tempearture and density

The plasma temperature and electron density can be obtained through time-resolved emission spectra. Atomic lines of Al I 309.28 nm and Al I 396.15 nm were chosen to evaluate the electron temperature based on the assumption of local thermodynamic equilibrium.[1] As shown in Figure 2.19 (a), the plasma temperatures were estimated to be 5000 K to 8000K from 2 to 10 μs. Electron density, on the other hand, was evaluated from the Stark broadening.[1] The Al I 396.2 nm atomic line was chosen to measure the full width at half-maximum (FWHM) line width for evaluating the electron densities. As shown in Figure 2.19 (b), electron densities were on the order of 10^{16} cm^{-3} from 1 to 10 μs. Since the property of the laser-induced plasmas depends on several factors such as laser wavelength, laser energy, pulse duration and the sample itself, it is very difficult to compare the results obtained here with other results. But the results generally appear similar to our previous studies.[11,15]

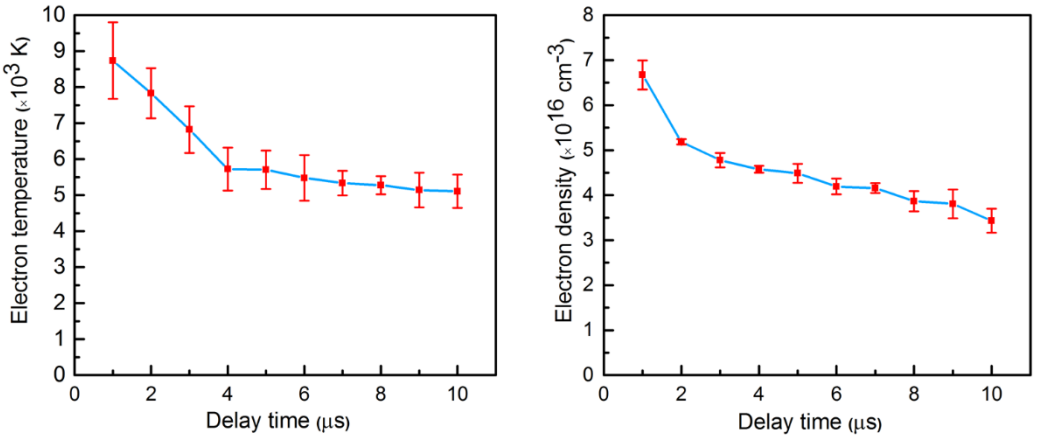

Figure 2.19 Time evolution of (a) electron temperature and (b) electron density in laser-induced plasma. The gate width was set at 1 μs. Each spectrum was averaged over 30 pulses.

2.5.6 Limits of detection measurement

Five Aluminum standard reference materials from NIST were used as targets in this study. The concentration details are listed in Table 2.2. Limits of detection (LODs) were calculated according to International Union of Pure and Applied Chemistry (IUPAC) criterion: LOD= 3σ/s, where σ is the standard deviation of the background and s is the slope of the calibration curve. The emission lines chosen to construct the calibration curves here were Cr I 367.87 nm, Mn I 403.07 nm, and Al I 309.28 nm.

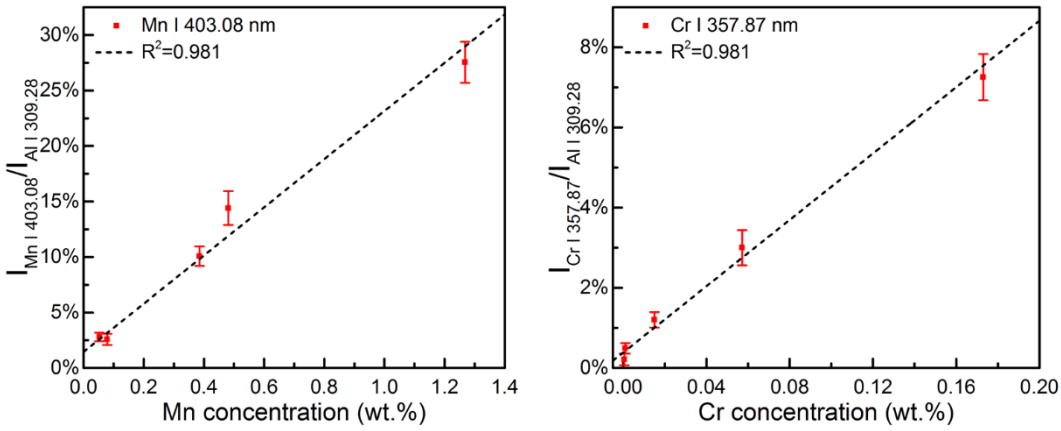

Figure 2.20 Calibration curves for (a) Mn (403.08nm) and (b) Cr (357.89 nm) in Aluminum samples. A gate delay of 1 μs and gate width of 10 μs were used for acquisition. Total number of 30 pulses were accumulated during each measurement.

Fifteen measurements were performed to produce the calibration curves. As shown in Figure 2.20, the obtained calibration curves have good linear fitting (R>98%) within the experimental uncertainty. The estimated LODs for trace elements of Cr and Mn were 101 and 192 ppm, respectively. The LODs obtained here were comparable to those reported in previous researches using a commercial actively Q-switched Nd:YAG laser.[46] The results obtained here are specific to experiment setup. The main objective here is not to improve LODs but to evaluate our laser performance in LIBS.

2.6 CONCLUSION

The new laser source developed here not only exhibits high laser performance but also meets the dimension, weight, and efficiency requirements of a field-portable laser source for LIBS

applications. Time-resolved LIBS measurements were successfully performed using this laser combined with an ICCD detector. Reliable LIBS results were obtained from these experiments.

Although similar laser design has been demonstrated before, the work undertaken for this study has resulted in a truly compact, lightweight, and high-performance laser. Furthermore, the laser runs at 24 V DC, making it possible to be powered by a battery. Most of the laser body is built from commercially available parts. Its weight and dimensions can be further reduced by using 3D printing technology, making it more attractive for LIBS applications. The details will be discussed in Chapter 4.0 .

In the following chapter, we will discuss the development of a double-pulse laser for LIBS application. The double-pulse laser shares many designs with the current single pulse laser. Thus, this chapter also serves as a foundation for the following chapter.

3.0 FIELD-PORTABLE DOUBLE-PULSE LASER SYSTEM

In this chapter, we developed a compact field-portable double-pulse laser system and tested its performance for LIBS applications. This double-pulse laser system has a total weight less than 11 kg, a total volume smaller than 0.02 m^3 and powered by 24 V DC. Compared with the recently developed commercially available double-pulse Nd:YAG system (EverGreen from Quantel-laser inc), our laser has many advantages such as advanced VCSEL pumping, passive air cooling, built-in pulse triggering system, higher efficiency, less weight, compact size and the ability to run on battery. The laser system consists of two identical actively Q-switched lasers with a maximum pulse energy of 12 mJ and a wavelength of 1064 nm. Two laser pulses are coupled together through a collinear beam coupling device. We also tested this double-pulse laser in several LIBS experiments, where significant improvement of LIBS performance was obtained.

3.1 DOUBLE-PULSE LASER OVERVIEW

Laser-induced breakdown spectroscopy is a powerful technology to determine elemental composition. However, it suffers from a relatively poor sensitivity with respect to other spectrometric methods. Double-pulse laser-induced breakdown spectroscopy (DP-LIBS) has been

proved to be a very effective approach for improving LIBS performance in terms of enhancing emission intensities, lowering limits of detections and improving signal-to-noise ratio.[47-49] Up until now, most of the double-pulse LIBS experiments are performed using benchtop lasers which are not suitable for field-portable LIBS applications. Field-portable single-pulse LIBS systems capable of real time and in-situ analysis[22,23,50] have been demonstrated by using compact laser sources such as fiber lasers[26,51,52], microchip lasers[27,53] and passively Q-switched flash lamp pumped solid-state lasers [54]. Despite of the intensive researches in double-pulse LIBS and field-portable LIBS, very few double-pulse LIBS experiments were performed using field-portable laser systems.[28]

(a)

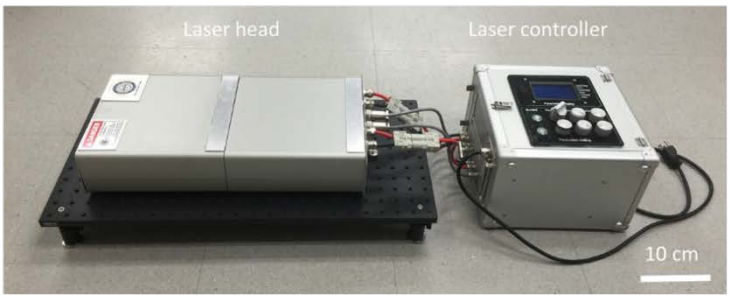

(b)

Property	value
Max pulse energy	15mJ/Pulse
Pulse widtgh	10 ns
Pulse jitter	+/- 5 ns
Pulse delay	0 ns to 100 ms, 62.5 ns resolution
Laser head weight	5 kg
Laser head size	85mm*215mm*450mm
Laser controller weight	5 kg
Laser controller size	170*240mm*270mm

Figure 3.1 (a) Photo of the double-pulse laser system that consists of a laser head and a laser controller and (b) the laser system's key parameters.

A real field-portable laser needs to fulfil the requirement of size, weight and energy consumption. It should have a compact size, light weight and be powered with battery. The lasers are also required to possess good beam quality for beam combining. Nevertheless, precise timing control and low timing jitter are equally important to perform time-resolved measurement. Figure 3.1 shows the double-pulse laser system that fulfills all the above requirements.

3.2 DOUBLE-PULSE LASER DESIGN

3.2.1 Optical design of laser head

The double-pulse laser system consists of a laser head that has all the optical components and a laser controller that contains all the electrical components. In this section, we will focus on the laser head design. Figure 3.2 (a) shows the schematic of the laser head. It consists of a collinear pulse coupling device as shown in Figure 3.2 (b) and two identical actively Q-switched lasers as shown in Figure 3.2 (c). We built our laser system based on Thorlabs 30 mm cage system that features four rigid steel rods on which optical components can be mounted along a common optical axis and an extensive selection of accessories for the cage system are also available. We also designed and made parts that were not commercially available. Dovetail optical rails were used to mount both lasers and beam coupling device to the laser case. The dovetail rails have the advantage of low profile and easy release feature, making it a suitable candidate to build stable, rigid mechanical assemblies. The optomechanics components are shown in Figure 3.3.

In double pulse LIBS, there are mainly two configurations, collinear and orthogonal. In collinear configuration, the two laser beams share the same optical path while in orthogonal configuration, one of the laser beam is directed perpendicular to sample surface and another is parallel to the sample surface. The advantage of our collinear device is that it is suitable for field LIBS applications, since it is more compact and there is no need for alignment. The collinear beam coupling device, shown in Figure 3.3 (g). The ½ waveplates along with the polarizing beam splitter are used to attenuate the output pulse power without compromising pulse performance, such as changing pulse width and introducing pulse jitter. The pulse intensity attenuation is achieved by rotating the ½ waveplate, as shown in Figure 3.3 (c). A focusing lens at the front of polarizing

beam splitter is used to focus the pulses on sample surface. Knob 1 and Knob 2 are used to align two focused laser pulses to the same spot.

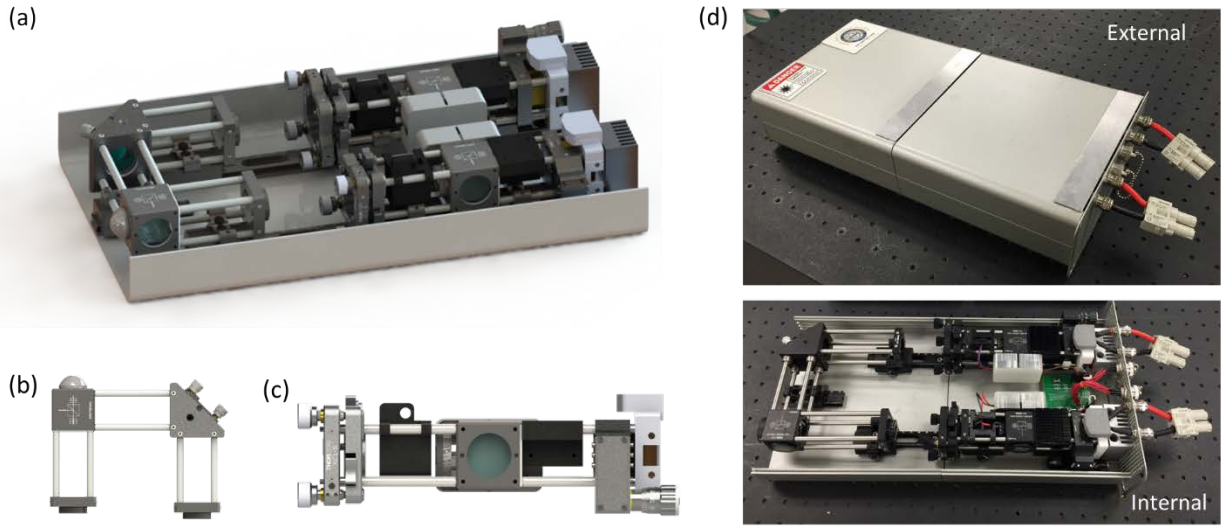

Figure 3.2 Laser head design. (a) schematic of double-pulse laser system, (b) schematic of collinear beam coupling device, (c) schematic of actively Q-switched laser, (d) photo of laser head external and internal view.

These two Q-switched lasers have similar design as described in the previous chapter but with a few improvements. For example, the output coupler is replaced by an updated version with adjustment knob, shown in Figure 3.3 (a). Since the laser body is protected by an enclose, the adjustment knob won't be accidently touched, which may lead to cavity misalignment. The focusing lens mount, as shown in Figure 3.3 (d), has a fine adjustment knob that allows precision control over pumping energy injection. For laser crystal holder, as shown in Figure 3.3 (e), an updated version is made with weight reduced by at least 50%.

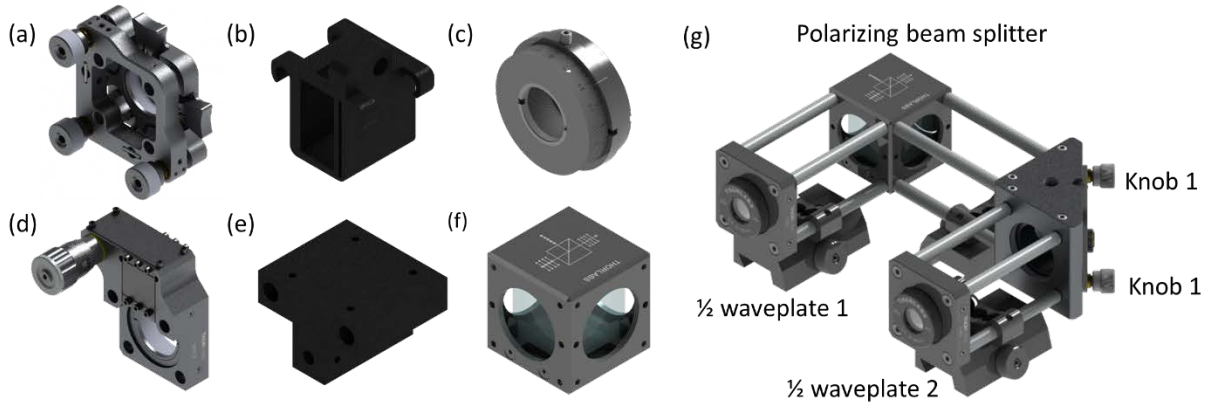

Figure 3.3 Laser optomechanics components. (a) Output coupler mount, (b) Pockels cell mount, (c) ¼ waveplate mount, (d) Focusing lens mount, (e) Laser crystal mount, (f) High power polarizing beam splitter, (g) Collinear beam coupling device.

Thermal management system is also improved compared with the laser developed in the previous chapter. In our previous single pulse laser, VCSEL heatsink is cooled by a mechanical fan that may induce vibration. In our current double-pulse laser system, VCSEL heatsink, as shown in Figure 3.4 (a), features a fanless design. The heatsink is bolted to the aluminum enclosure so that heat can be conducted to the enclosure and then dissipate to the environment. A crystal holder made of Al is made to hold and cool the crystal. A loss fit is chosen to hold laser crystal to avoid damaging. Thermal grease is used to fill the gap between crystal and its holder to effectively transfer heat. During the testing, both cooling structures work very well. No VCSEL overheating or crystal thermal lensing is observed.

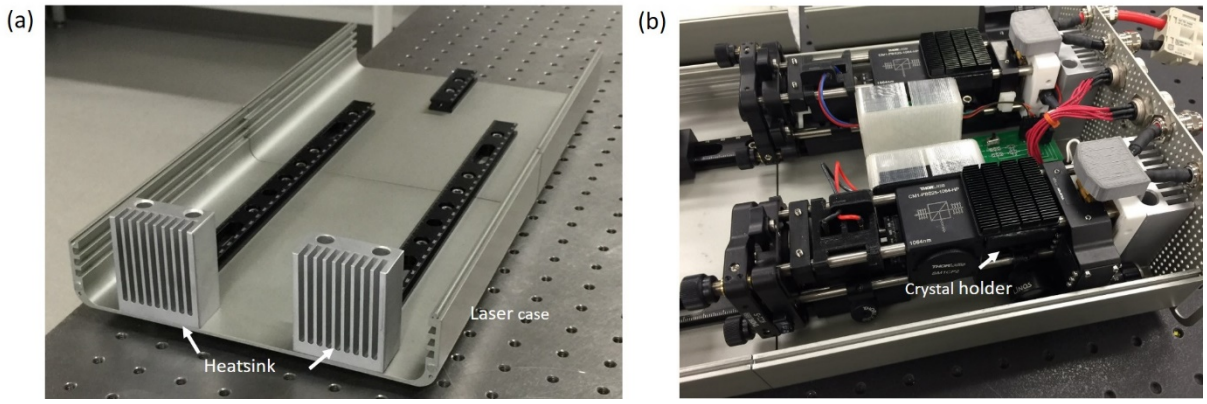

Figure 3.4 Laser thermal management system. (a) Photo of VCSEL cooling design, (b) Photo of laser crystal cooling design.

3.2.2 Electrical design of laser controller

The laser controller contains all the key electronics to drive the laser. It features a user-friendly interface electronics (screen, knobs and buttons) as shown in Figure 3.5 (a). The detailed description of this interface is shown in Figure 3.5 (b). Figure 3.5 (c) shows the internal structure of laser controller, which can be divided into four units, as shown in Figure 3.5 (d), temperature control unit, VCSEL driver unit, timing control unit and user input unit. The temperature control unit and VCSEL driver unit are the same as the single pulse laser controller. But the timing control unit and user input unit are completely new designs. A more powerful microcontroller ATmega2560 is used here. A PCB board is used to hold all the key electronics components, such as microcontroller, temperature control units, resistors and capacitors. Even with lots of electrical components, the laser controller has a compact dimension of 170 mm × 240 mm × 270 mm and weighs only 4.5 kg.

The core component of laser controller is a Mega 2560 microcontroller board based on the ATmega2560 chip. It can monitor laser status, read user input, and change laser parameter

accordingly. The detailed pin mapping is shown in Table 3.1. The programing language used here is also C++. Since ATmega2560 chip is much more powerful than ATmega326 chip, it allows us to write more complex program (about 1000 lines in our software). The software flowchart is shown in Figure 3.6 (a). The LCD can display key laser parameters, such as VCSEL pumping power and temperature, laser on/off status, pumping time and pump delay.

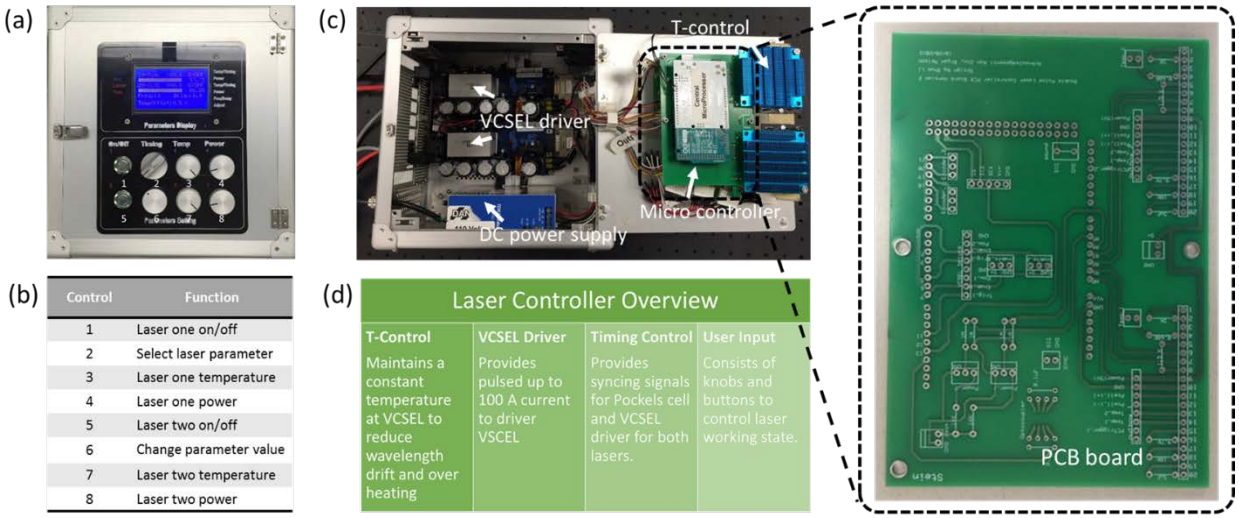

Control	Function
1	Laser one on/off
2	Select laser parameter
3	Laser one temperature
4	Laser one power
5	Laser two on/off
6	Change parameter value
7	Laser two temperature
8	Laser two power

Figure 3.5 Laser controller design. (a) Photo of laser controller panel, (b) Knob function, (c) Photo of laser controller internal view, (d) Laser controller overview.

The successful operation of actively Q-switched lasers depends on precise timing. This is especially true for double-pulse laser where four triggering signals are needed. Two of the signals are used to trigger VCSEL driver and the other two are used to trigger Pockels cell drivers. Low time jitter and adjustable time delay should also be possible among these signals. The powerful microcontroller ATmega2560 has several 16-bit timers that can fulfill these requirements. There are several parameters needed to be set up for laser to work properly. These parameters can be set up in laser controller using knobs and buttons shown in Figure 3.6 (a). No additional digital delay

generator is required for triggering and syncing both lasers. The detailed timing chart is shown in Figure 3.6 (b). The timing resolution of laser controller is 4 μs, which is enough to perform LIBS experiment. The resolution can also be further improved to 62.5 ns.

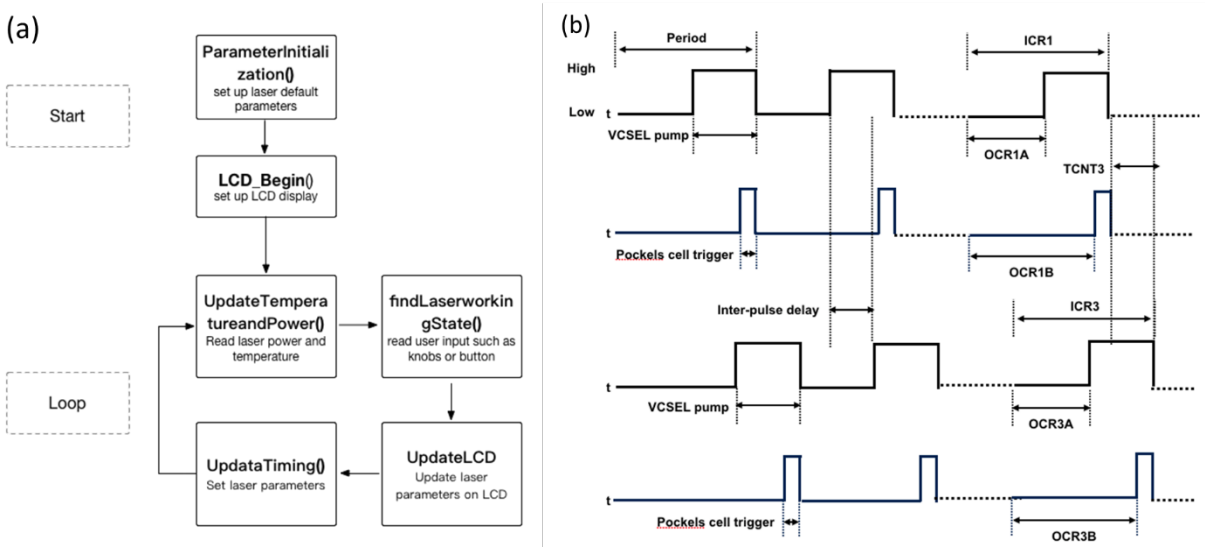

Figure 3.6 (a) Laser controller software flowchart and (b) Timing diagram of triggering signal from microcontroller.

Table 3.1 Pin mapping of microcontroller Mega 2560 and its function.

Mega 2560	Pin	Function
Timing output	11	Provides trigger signal to VCSEL 1
	12	Provides trigger signal to Pockets cell 1
	5	Provides trigger signal to VCSEL 2
	2	Provides trigger signal to Pockets cell 2
	3	Provides trigger signal to ICCD
Encoder reading	18	Reads increase signal from Encoder 1
	19	Reads decrease signal from Encoder 1
	20	Reads increase signal from Encoder 2
	21	Reads decrease signal from Encoder 2
Power and temperature	A0	Reads VCSEL real temperature from temperature controller 1
	A1	Reads VCSEL set temperature from user input 1
	A2	Reads VCSEL real temperature from temperature controller 2
	A3	Reads VCSEL set temperature from user input 2
	A4	Reads VCSEL driver current 1
	A5	Reads VCSEL driver current 2
Laser state	7	Reads Laser 1 on/off state
	6	Reads Laser 2 on/off state
LCD display	13	Provides display signal, connected to LCD SCK
	24	Provides display signal, connected to LCD SID
	22	Provides display signal, connected to LCD CS

3.3 DOUBLE PULSE LIBS EXPERIMENT

3.3.1 Experiment setup

The schematic of double-pulse LIBS experiment setup is shown in Figure 3.7. There are two types of configurations, one used for plasma imaging, another used for plasma spectrum. In the plasma imaging configuration, as shown in Figure 3.7 (a), the plasma was imaged by a single lens (50 mm) at the spectrometer entrance slit, which is wide-open to avoid cropping image. The grating is

set at its zero order which act as a mirror. The plasma will finally be imaged at ICCD and then recorded. In the plasma spectrum configuration, as shown in Figure 3.7 (a), the light emission from plasma was collected by a two-lens system (lens 1 with 60 mm focal length, lens 2 with 100 m focal length, effective magnification of ~0.6). A bundle consisted of 19 optical fibers (200-μm diameter) was used to transmit the collected light to the entrance slit of a spectrometer (Andor Tech., Shamrock 505i). The spectrometer was outfitted with a 1024×1024-pixel intensified charge coupled device (ICCD) detector (Andor Tech., iStar, DT-334T) that allowed us to perform time-resolved measurement. The grating used here was 1200 line/mm. The complete detection system had a spectral range of approximated 20 nm with a resolution of 0.06 nm.

Table 3.2 Elemental concentrations (wt.%) of Mn and Cr in Al alloy sample.

	Standard Reference Materials (wt %)			
Elements	1256b	1240C	1258I	No.1259
Mn	0.3857	1.2680	0.4810	0.0790
Cr	0.0572	0.00054	0.0011	0.1730

For a conventional DP-LIBS system, a digital delay generator with at least 4 triggering outputs is needed to synchronize two lasers and perform time-resolved measurement. Since our laser controller has a built-in signal synchronize system, no such digital delay generator is needed. The synchronizing signal of two lasers and the spectrometer triggering signal are both provided by the laser controller. A diagram explaining the timing sequence in double-pulse LIBS is shown in Figure 3.7 (b). Inter-pulse delay is defined as the time difference between the arrival of two laser

pulses. Gate delay is the time difference between the arrivals of second laser pulse and the time that spectrometer begins to acquire spectral data.

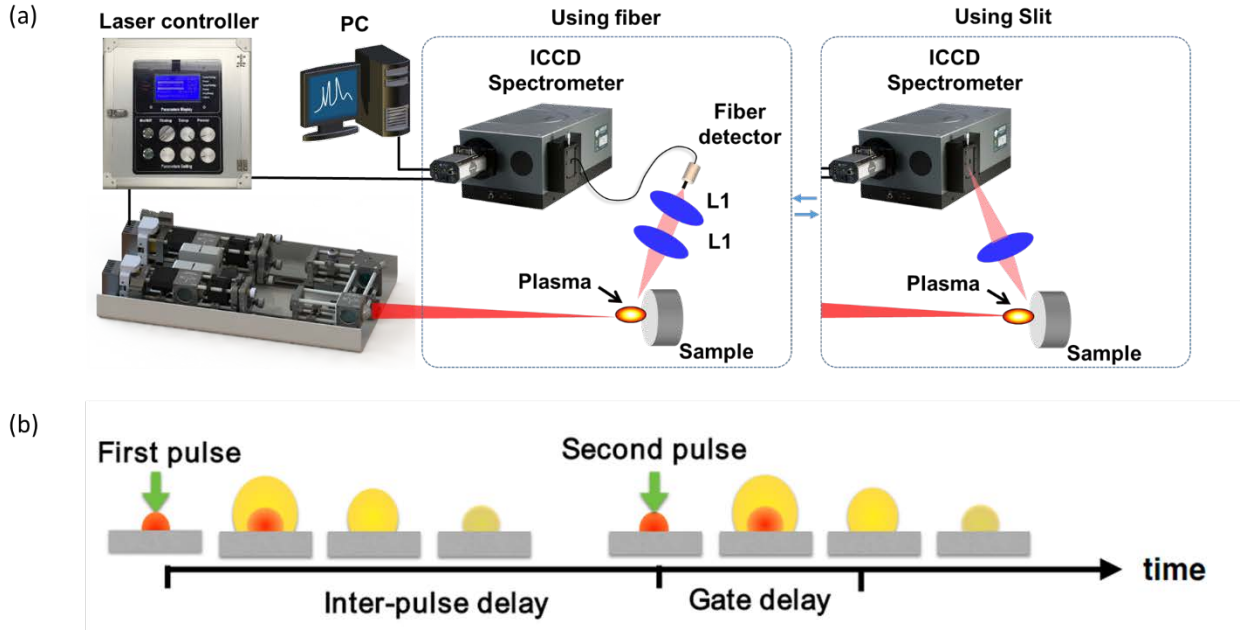

Figure 3.7 Double-pulse LIBS experiment setup. (a) Schematic of experiment setup, (b) Timing sequence.

The pulses from both lasers were focused on the same place on sample surface through a lens with 75 mm focal length. The focused laser beam had a spot diameter about 0.8 mm. During the experiment, the sample was continuously moved by a computer-controlled motorized stage to avoid over ablation. Its position was carefully adjusted to maximize signal intensity. The pulse energy and repetition rate for both lasers were set at 10 mJ and 10 Hz, respectively. Four Aluminum alloy standard reference materials from NIST were used as the targets in this study. The concentrations of both Mn and Cr are listed in Table 3.2. NIST-1256b sample was used for all the LIBS experiments. In the limit of detection experiment, all four samples were used.

3.3.2 Time-resolved measurement

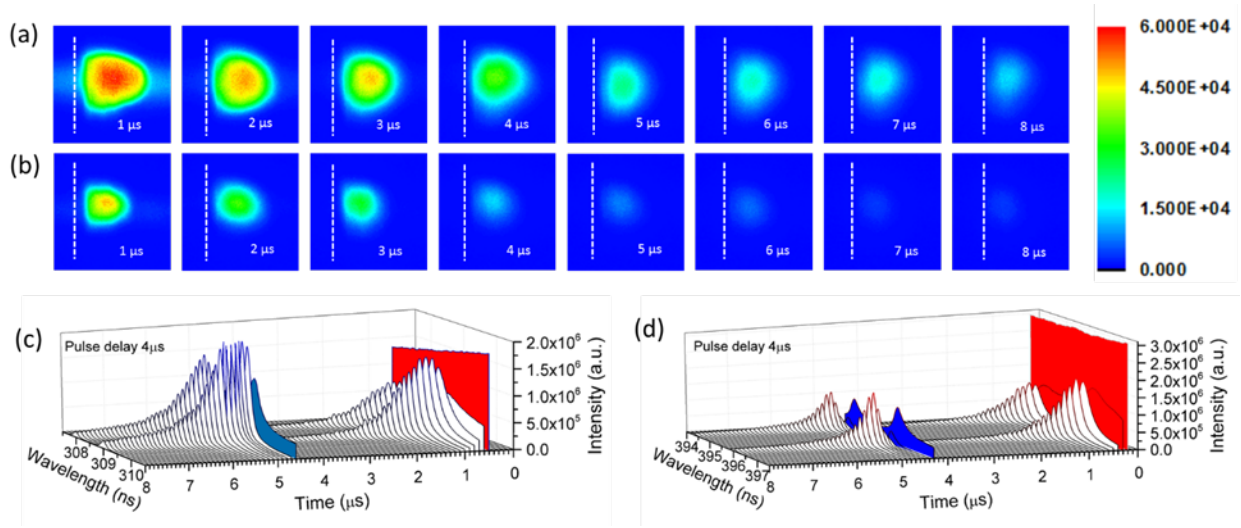

Figure 3.8 Time-resolved measurement. Time-resolved image of plasmas generated by (a) double-pulse and (b) single pulse. Time-resolved spectrum of (c) Al 308.2 nm, 309.3 nm lines and (d) 394.4 nm and 396.2 nm lines.

Time-resolved measurement in LIBS is the most powerful and fundamental technic that allows one to study the dynamic process in plasma, such as evolution of electron density and temperature inside plasma, the growth of plasma plume. Here, we compared the performance of SP-LIBS and DP-LIBS in terms of time-resolved plasma image and plasma spectrum. Figure 3.8 shows the time-resolved images of plasma generated by (a) double-pulse and (b) single-pulse at zero inter-pulse delay. In DP-LIBS configuration, enhanced plasma optical emission, longer plasma lifetime and larger plasma size were observed, agreeing well with previous study [46]. Unlike the previous study, our result was obtained at much lower energy (~10 mJ/pulse), making it suitable for field-portable application where lower pulse energy is preferred. Time-resolved Al emission spectrum in the range of 307~310 nm and 394~398 nm was shown in Figure 3.8 (c) and (d), respectively, where Al atomic emission lines peaked at 308.2 nm, 309.3 nm, 394.4 nm and 396.2 nm. During the early

plasma lifetime (<500 ns) for the spectrum generated by the first laser pulse, as shown in the red area, the continuous background emission was very strong and no useful line emission was observed. However, during the same period for the spectrum generated by the second laser pulse, as shown in the blue area, the continuous background emission was significant reduced and characteristics line emission was successfully revealed. This is one of the major advantages of DP-LIBS. We will provide more detailed study later.

3.3.3 Signal enhancement

To further study signal enhancement in double-pulse LIBS. We repeat the previous experiment at various inter-pulse delay. Figure 3.9 (a) shows the peak emission spectrum of Al 308.2 nm, 309.3 nm, 394.4 nm and 396.2 nm at various inter-pulse delay. Figure 3.9 (b) and (c) shows Al I 308.2 nm and Al I 394.2 nm peak intensity evolution under various inter-pulse delay, respectively. A set of three measurements were made for each point shown in the figure. Inserted figure is the average enhancement factor as a function of inter-pulse delay at the gate delay of 2 μs. As is shown, maximum signal enhancement for different peaks wasn't obtained at the same inter-pulse delay.

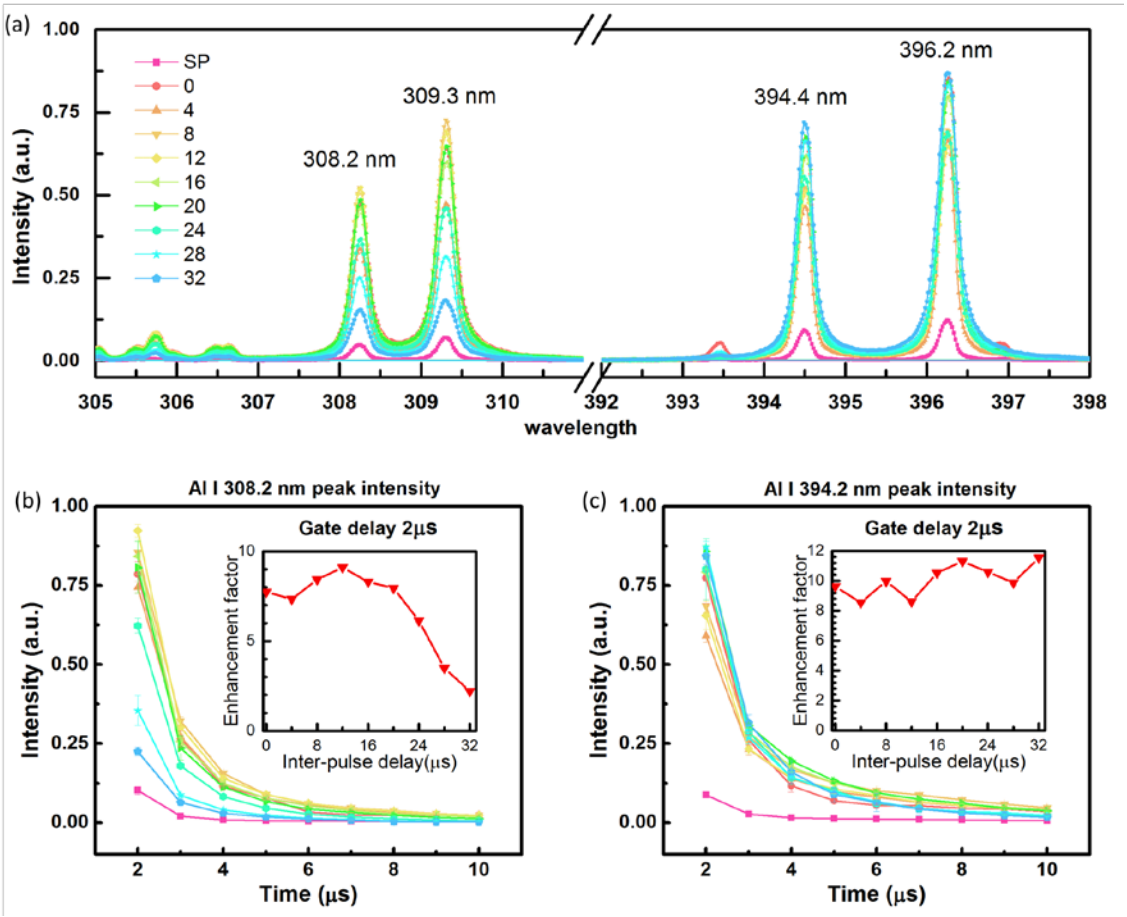

Figure 3.9 Signal enhancement in double-pulse LIBS. (a) Al peak intensity enhancement at various inter-pulse delay, Gate width: 1 μs. Gate delay: 2 μs. SP means Single pulse, unit is μs. (b) Al I 308.2 nm peak intensity evolution under various inter-pulse delay. Gate width: 1 μs. Inserted figure is the enhancement factor as a function of inter-pulse delay at the gate delay of 2 μs. (c) Al I 394.2 nm peak intensity evolution under various inter-pulse delay. Gate width: 1 μs. Inserted figure is the average enhancement factor as a function of inter-pulse delay at the gate delay of 2 μs.

3.3.4 Signal stability improvement

There are several ways to enhance LIBS signal, such as using longer integration time, larger ICCD gain and stronger laser pulse. However, these methods may also introduce noise in the measurement. The enhanced peak emission intensity obtained by double-pulse method leads to a

better signal-to-noise ratio but not necessarily a better shot-to-shot signal stability. Here, we compare the shot-to-shot signal stability of SP-LIBS and DP-LIBS, which affects the precision of LIBS measurement.[44] The strong Al 308.2 atomic emission line was chosen to minimize the effect of inhomogeneity. The relative standard deviation (RSD) of Al 308.2 nm peak-to-base atomic emission ratio was calculated from a set of 400 repeated single-shot *spectra*. Shot-to-shot emission peak analysis for single-pulse mode and double-pulse mode are shown in Figure 3.10 (a) and (b), respectively. The RSD was reduced from 16% in single-pulse mode to 7% in double-pulse mode. Similar analysis was performed on Al I 308.2 nm to Al I 309.3 nm peak-to-peak atomic emission ratio The RSD was reduced from 5.8% in single-pulse mode to 3.1% in double-pulse mode. Similar result has been demonstrated using double-pulse femtosecond lasers in a previous study using aluminum alloy samples.[55] The improved signal stability was obtained along with the enhanced signal intensity in double-pulse mode, thereby further enhancing the overall quality of LIBS signal. Therefore, a significant improvement in the sensitivity of double-pulse LIBS should be expected, where the limit of detection is improved.

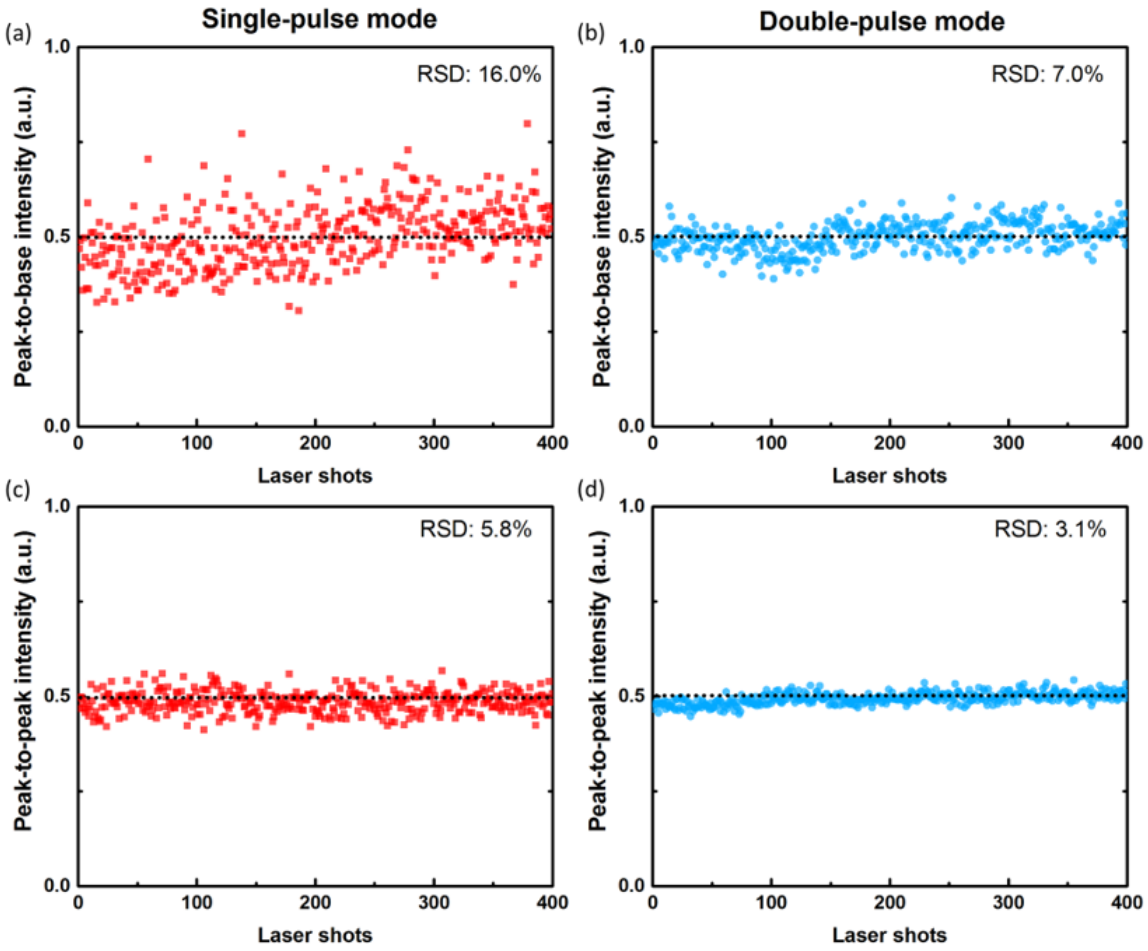

Figure 3.10 Signal stability improvement. Peak-to-base of Al I 308.2 nm emission intensity ratio in (a) single-pulse mode and (b) double-pulse mode. Peak-to-peak of Al I 308.2 nm to Al I 309.3 nm emission intensity ratio in (c) single-pulse mode and (d) double-pulse mode. Inter-pulse delay: 4 μs. Gate delay: 1 μs. Gate width: 1 μs.

3.3.5 LOD improvement

As one of the most important metrics to gauge the performance of LIBS experiments, the limit of detection (LOD) was studied using four Aluminum alloy standard reference materials from NIST as listed in Table 3.2. LOD was calculated according to International Union of Pure and Applied Chemistry (IUPAC) criterion: LOD= 3σ/s, where σ is the standard deviation of the background

and s is the slope of the calibration curve. The emission lines chosen to construct the calibration curves here were Cr I 425.3. nm, Mn I 403.1 nm, and Al I 309.3 nm. Fifteen repeated measurements were performed to produce the calibration curves.

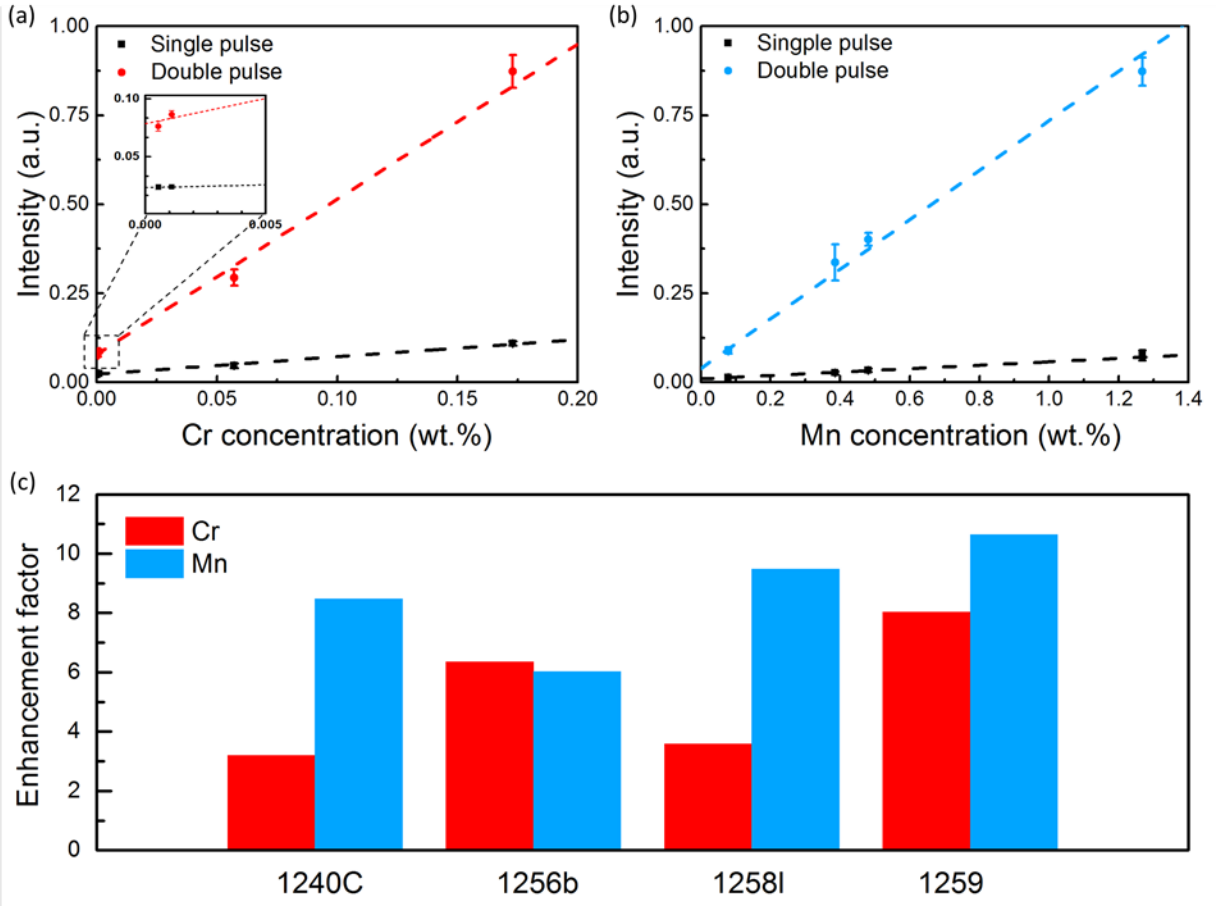

Figure 3.11 Limit of detection improvement**.** Calibration curves for (a) Cr (425.3 nm) and (b) Mn (403.1 nm) in single-pulse and double-pulse mode. Inter-pulse delay: 8 μs. Gate delay: 1 μs. Gate width: 10 μs. Inserted zoom-in figure in (a) shows overlapped data points. (c) Signal enhancement factor for the elements used to construct the calibration curve in various samples.

As shown in Figure 3.11, the obtained calibration curves have a good linear fitting (R>98%) within the experimental uncertainty. For Mn, the LOD was nearly 10 times lower with the double-pulse LIBS of 38 ppm compared to that of the single-pulse LIBS of 326 ppm. The LOD for Cr was also lowered from 158 ppm to 30 ppm for the double-pulse scheme. The significantly improved LOD using the double-pulse laser system indicates its promising prospect for field work detection requiring high detection sensitivity[56,57] with limited laser power.

3.3.6 Investigation of early plasma behavior

For most of the double-pulse LIBS experiments, a gate delay of several hundreds of nanoseconds should be used to avoid the strong continuum background emission that happens during the very early plasma lifetime. The useful information is the characteristic line emission of ion and atom which begin to show up when continuum background emission vanishes. Therefore, very few researches have been focused on the early plasma lifetime.[58-60] In recent studies[7,61,62], it is pointed out that the continuum background is significantly reduced in the early plasma lifetime using double pulse laser. With this reduced background, the early plasma lifetime may show useful information, which is crucial for understanding the subsequent plasma behavior. In previous Figure 3.8, we have already show such effect. Here, in Figure 3.12, a much shorter gate width of 20 ns was used, thus offering a much higher time resolution. For single pulse shown in Figure 3.12 (a), during the very early plasma lifetime (<300 ns), strong continuous background was observed. However, for double pulse with 4 μs inter-pulse delay shown in Figure 3.12 (b), a sharp emission peak was observed instead of the continuous background. As the inter-pulse delay was increased

to 12 μs and 28 μs when the plasma generated by the first pulse almost cools down, the continuous background began to show up with reduced emission peak.

The continuous background emission comes from the bremsstrahlung radiation so that continuous electromagnetic radiation is produced by the deceleration of electron. [6]. In double pulse LIBS, the plasma generated by the second laser pulse growth in an environment created by the plasma generated by the first laser pulse, where pressure in such an environment is usually much lower than room pressure. Thus, the electron expands much faster, leading to a reduced continuous background emission. [7] On the other hand, there are several factors that contribute to the enhancement of line emission. First of all, the shockwave generated by the second laser pulse can excite plasma generated by the first laser pulse.[11] Secondly, the second laser pulse itself can also re-excite the atom/ion that generated by the first laser pulse. Thirdly, the high energy free electron generated by the second laser pulse interact with the atom/ion generated by the first laser pulse, transferring energy to them.

As inter-pulse delay is increased, the plasma generated by first laser pulse cools down even further. The atoms recombine and form molecules that requires more energy to excite. The pressure inside the plasma plume begins to approach to room pressure. The environment where the new plasma to be generated by the second pulse grows begins to look like ambient environment. Therefore, as the inter-pulse delay is increase, the double-pulse enhancement effect is reduced.

In the following experiment, the enhancement factor of several ionic lines were studied during the very early stage of plasma lifetime[63]. The gate delay was set at 0 ns and gate width was set 500 ns. As is shown in Figure 3.13, the ionic lines with higher excited upper energy level such as Ca II 370.60 nm and 373.69 nm, the enhancement factor is minor compared with those ionic lines with lower excited upper energy levels. For example, for Na II 353.31 nm line, there is no

signal at all in single pulse LIBS, but a very shape peak is found in double pulse LIBS. Therefore, we have developed a method to selective enhance LIBS signal.

In previous studies, LIBS-LIF[10,64] is the most widely used method to selective enhance LIBS signal. On disadvantage of conventional LIBS is the signal interference. For example, when the characteristic line of a trace element is overlapped with the characteristic line form other elements, such trace element can't be detected. To solve this problem, LIBS-LIF method was used where a second laser is tuned to re-excite the target element when all the signals disappeared. However, such LIBS-LIF method is only widely used in the lab and hasn't been adapted to perform field work, because tunable lasers with high peak power and nanosecond pulse width are very bulky and heavy. Such lasers are not suitable to perform field work.

The double pulse laser system we developed here are not only small but also light weight, making it suitable to perform field work. Combined with the selective enhancement method during early stage plasma lifetime, this double pulse laser system has the potential to be used in field work where characteristic lines overlapped happened.

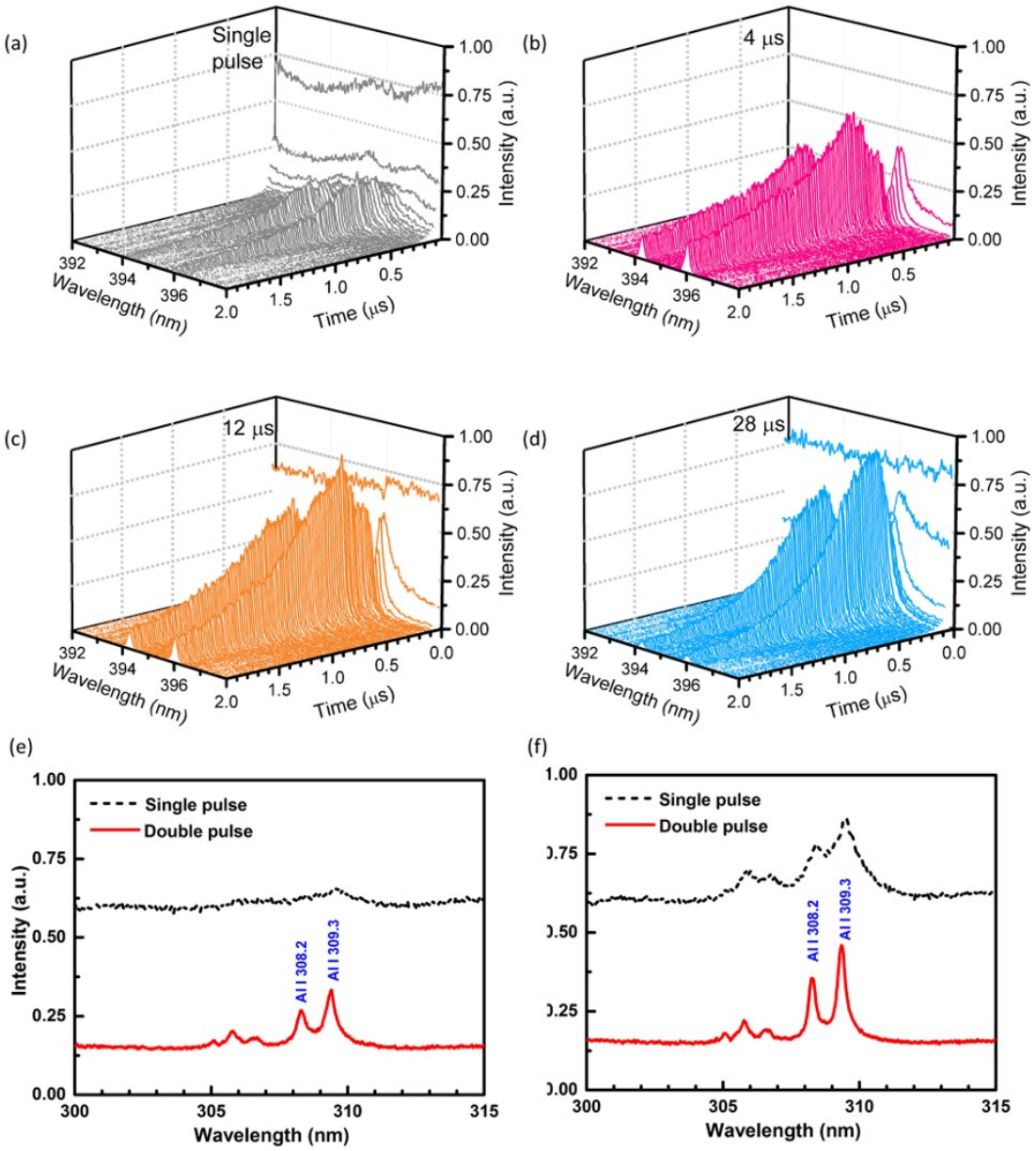

Figure 3.12 Plasma emission during early plasma lifetime. Time-resolved emission spectrum during early plasma lifetime of (a) single-pulse, (b) double-pulse 4 μs inter-pulse delay, (c) double-pulse 12 μs inter-pulse delay, (d) double-pulse 28 μs inter-pulse delay. Gate width: 20 ns. Early plasma emission spectra with gate width of (e) 100 ns and (f) 200 ns. The gate delay was 0 μs.

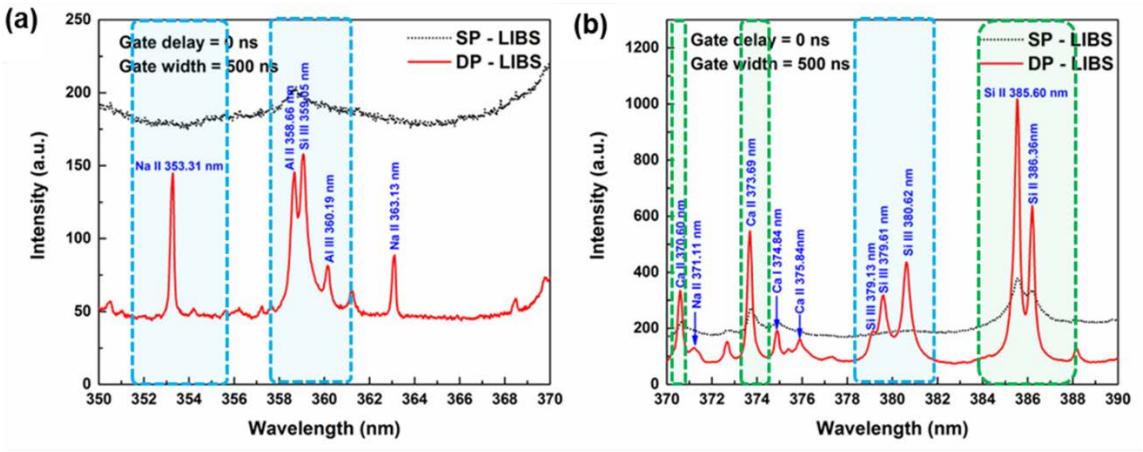

Ionic lines (nm)	Excited upper energy level (cm^{-1})	Ionic lines (nm)	Excited upper energy level (cm^{-1})
Ca II 370.60	52166.93	Si II 385.60	81251.32
Ca II 373.69	52166.93	Si II 386.36	81191.34
Na II 353.31	293220.33	Si III 359.05	204330.79
Al II 358.66	123423.35	Si III 379.61	201598.28
Al III 360.19	143713.50	Si III 380.65	201599.48

Figure 3.13 Enhancement factor v.s. upper energy level. For ionic lines with lower excited upper energy level, the enhancement factor is small. For ionic lines with higher excited upper energy level, a larger enhancement factor is found. SP-LIBS: Single pulse laser-induced breakdown spectroscopy. DP-LIBS: Double pulse laser-induced breakdown spectroscopy.

3.4 CONCLUSION

This chapter presents appealing experiment results that compact lasers with output pulse energy at 10 mJ level can perform highly sensitive LIBS experiment with significantly better performance than those using a single-pulse with similar laser pulse energy. A truly field-portable double-pulse laser system at 10 mJ level was constructed and tested for LIBS applications. Several LIBS

experiments have been performed to test its performance. Up to 9 times enhancement in atomic emission line were achieved with continuum background emission reduced by 70%. This has led to up to 10 times improvement on limit of detection. Signal stability is also improved by 128%, indicating a more robust and accurate LIBS measurement. The compact double-pulse laser presented here provides a viable tool to significantly improve functionality and applicability of the field-portable LIBS technology.

4.0 UNIBODY LASER ENABLED BY ADDITIVE MANUFACTURING

In this chapter, we designed, manufactured and demonstrated a 3D-printed passively Q-switched Nd: YAG laser that is compact, lightweight, and powerful. The entire laser frame was built as a single aluminum piece, featuring advanced mechanical and thermal designs. Passive air cooling and active water cooling mounts based on cellular structures were built into the frame. Meanwhile, we optimized the cell structure by using non-uniform design, which can reduce thermal deformation by 41.2%. More importantly, our results pave the way towards manufacturing, unique, single-purpose laser systems using 3D printing technology.

4.1 DIRECT METAL LASER SINTERING OVERVIEW

In this work, we used a powder-bed direct metal laser sintering (DMLS) technique to print laser frame. The DMLS technology takes a CAD model as its input and builds the geometry by depositing the constituent materials precisely in a layer-by-layer fashion. Figure 4.1 illustrates the operating principles of a powder bed DMLS system. For each layer of build, it deposits a layer of tiny particles across the entire powder bed. The production chamber is filled with inert gas to reduce the damaging effects of oxidation. As the particles are being deposited, a roller attached to

the depositor compacts the particles so that the resulting material has higher density and is thus stronger. A focused laser beam begins to move across the powder and the path of the laser beam is defined by the CAD file. The metal powder is melted into a solid part. After each layer is built, the powder bed is lowered by one layer thickness, and the whole process is repeated until the entire part has been built. When the building process is completed, the final model is left to cool. The unsintered powder is then recovered and recycled. Support structure is implemented wherever necessary and will be broken away from the laser frame during the post-machining.

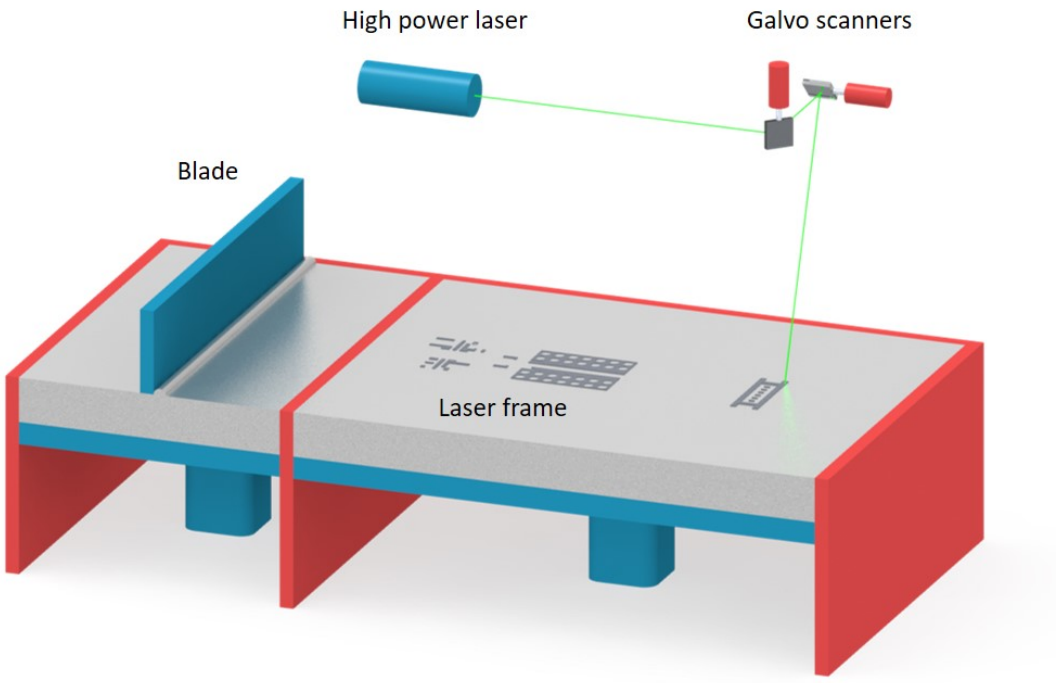

Figure 4.1 Schematic of the powder-bed direct metal laser sintering.

4.2 UNIBODY COMPACT LASER DESIGN

4.2.1 Unibody laser system overview

The optical design of this laser features a compact and elegant setup[4], as shown in Figure 4.2 (a). It consists of a vertical-cavity surface-emitting laser (VCSEL) array pump laser, a lens, an Nd: YAG crystal rod, a Cr: YAG passive absorber, and an output coupler. The VCSEL array delivered a maximum output power of 800 W at 200 A with a wavelength of 806.9 nm. The VCSEL worked in quasi-cw mode that permitted high output powers without exceeding the thermal limitation of the device. It was used to end-pump the Nd:YAG crystal rod. A single lens with 10 mm focal length was used to couple the VCSEL array pump light into the laser rod through one end. This pump end of the crystal acted as an end mirror of the laser cavity. The Nd: YAG rod had an anti-reflection (AR) coating for the pump wavelength of 806.9 nm and a high-reflection coating for the lasing wavelength of 1064 nm on the side facing the VCSEL. On the other end of the rod, there was an AR coating for the lasing wavelength. The Cr: YAG passive absorber was also AR coated and had an initial transmission of 55% at the lasing wavelength. A flat output coupler with a transmission of 50% acted as the output coupler of the laser cavity. When such cavity is lasing, it places a strict requirement on the alignment and stability, thus providing a good example to test the overall performance of the 3D printed laser frame.

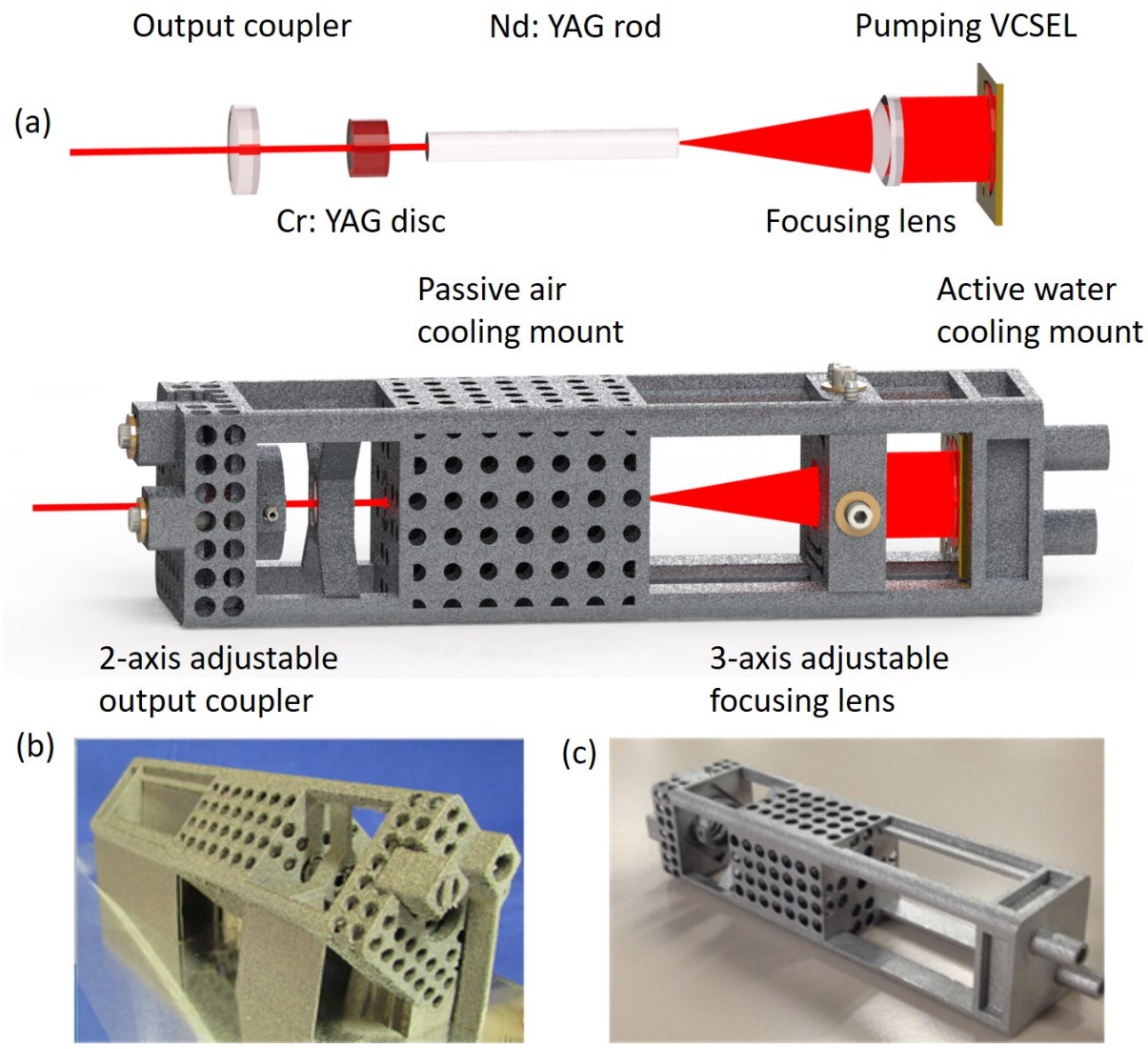

Figure 4.2 Schematic and photos of the 3D printed laser. a, Schematic of passive Q-switched laser cavity design and 3D printed laser frame with all the optical parts integrated into the frame. b, 3D printed laser frame with all the supporting structure. c, 3D printed laser frame with all the supporting structure.

The schematic of this laser, as shown in Figure 4.2 (a), features four functional structures, a 2-axis adjustable mirror mount, a passive air cooling mount, a 3-axis adjustable lens mount and an active water cooling mount. The whole laser frame weighs only 85 g after supporting structure was removed. To see how much weight can be saved, a similar laser frame was made based on

commercial available 30 mm cage system with some parts made from conventional manufacturing method. The total frame weight added up to over 1000g. Therefore, the 3D-printed frame here can reduce weight by at least 90%. The total weight of the 3D printed laser with all the optic components installed is only about 120g with a compact dimension of 3cm by 3cm by 15cm. Figure 4.2 (c,d) shows laser frame before and after supporting structure is removed.

4.2.2 Performance of 3D printed optomechanical parts

Flexure stages offer many merits over traditional bearing stages, such as being backlash free, frictionless, and exhibits highly repeatable motion [65]. Such a flexure stage is usually machined out of a single piece of metal. 3D printing, as an additive manufacturing method, makes it possible to design such a functional flexure structure that would be very difficult or impossible to make using conventional manufacturing method. Multiple components can be integrated into fewer parts offering a more rigid structure. Here, we demonstrated two types of flexure optical stages. One was an adjustable mirror mount that offers angular adjustment; the other was a 3-axis translation mount.

The adjustable mirror mount has two U-shape flexure structures that are perpendicular to each other as shown in Figure 4.3 (a,d). Each U shape structure can perform an angular adjustment in one direction. The adjustment was achieved through adjusting a 1/4"-80 Fine Hex adjuster which has extremely tight tolerances from Thorlabs. By adjusting screw 1, the mount can be rotated about x-axis. By adjusting screw 2, the mount can be rotated about z-axis. Thus, the two orthogonal U shape structures can provide independent angular adjustments in two respective orthogonal

dimensions. An output coupler was fixed to such a mount through a screw. For our current design, the adjustment range was at least 3°, which was enough for the cavity alignment.

Figure 4.3 (b,e) show the 3-axis translation mount that consists of a 2-axis flexure stage and a rail. The 2-axis flexure stage offers two orthogonal linear translation degrees of freedom. By adjusting screw 3, the stage can be moved along z direction, and by adjusting screw 4, the stage can be moved along x direction. The stage can also be moved along the rail which was printed into the frame, adding another translation degree of freedom. A lens was installed to such a mount through screws. The lens can then be moved along the rail to focus the pump beam onto the end face of laser crystal. After optimization, the stage can then be fixed to the rail by tightening the screw.

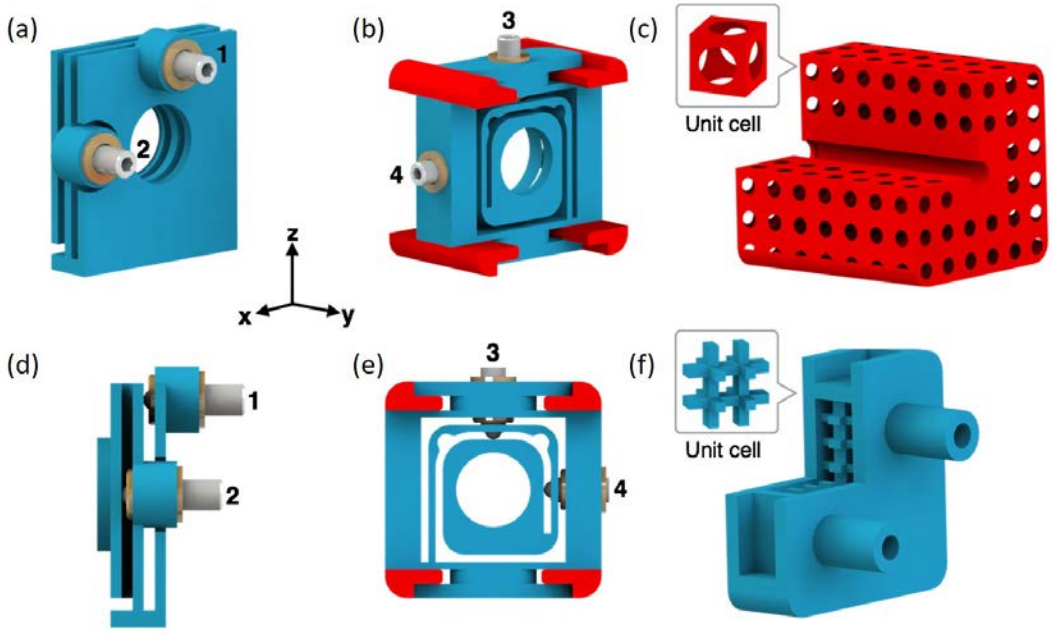

Figure 4.3 Laser mechanical and cooling design. a,d, Schematic of the 2-axis adjustable mirror mount based on flexure structure b,e Schematic of the 3-axis adjustable lens mount. c. Schematic of crystal cooling mount based

on cellular structure. The unit cell is a hollow-sphere-structure. f Schematic of VCSEl cooling mount based on cellular structure. The unit cell is a hollow-cubic-structure.

Nature frequently uses cellular materials such as wood, bones, and honeycombs as weight-optimized and functional structures. Inspired by this idea, artificial cellular structures have been studied for decades, and proven to have many excellent thermomechanical properties, such as high stiffness[66,67] , good impact absorption[68] , good heat dissipation ability[69], and potential for multifunctionality[70]. Therefore, we decide to introduce the cellular structure into designing the laser cooling system. Here, we demonstrate two cooling designs based on cellular structure, where a passive cooling mount is used to cool laser crystal and an active cooling mount is used to cool VCSEL. Since 3D printing offers unparalleled flexibility in make complex structure over traditional manufacturing methods[71] , these cellular structures can be easily made and integrated into laser frame.

As is shown in Figure 4.3 (c), a passive air cooling mount based on hollow-sphere structures [72] was used for cooling the laser crystal. The laser crystal covered by thermal compound was tightly fitted in the center of the crystal mount. For our Nd: YAG crystal, 50% of the pump power will be converted to heat in the crystal. High temperature may not damage the crystal but will cause a strong thermal lensing effect resulting to a smaller beam waist that is more likely to damage optical components. Due to the good heat dissipation ability of the crystal mount, thermal lensing effect was reduced. The high strength of the cellular structure also made the laser cavity mechanical stable.

Compared to the laser crystal, the VCSEL is more sensitive to temperature increases and requires more cooling power. Thus, an active water cooling base was made as shown in Figure 4.3 (f). This cooling base also featured a cellular structure used in the water cooling channel. This

cellular structure can double the heat exchange surface area, thus increasing the cooling efficiency. It can provide enough cooling power to maintain a low temperature for the VCSEL to ensure maximum output power, long life time and low wavelength drift.

4.2.3 LIBS experiment

A LIBS experiment was conducted to test laser performance. Since this laser features a passively Q-switched design, the spectrometer was chosen to work in ungated mode. The laser repetition rate was set at 10 Hz and laser pulse energy was 8 mJ. The measurement was performed by a spectrometer that integrated with an intensified charge coupled device detector (Andor Tech., iStar, DT-334T). Al standard reference sample (NIST-1762b) was used as target. The signal was collected to the spectrometer slit through a lens. As is shown in Figure 4.4, several elements such as Al, Fe, Mn, Cr and Mo were successful identified.

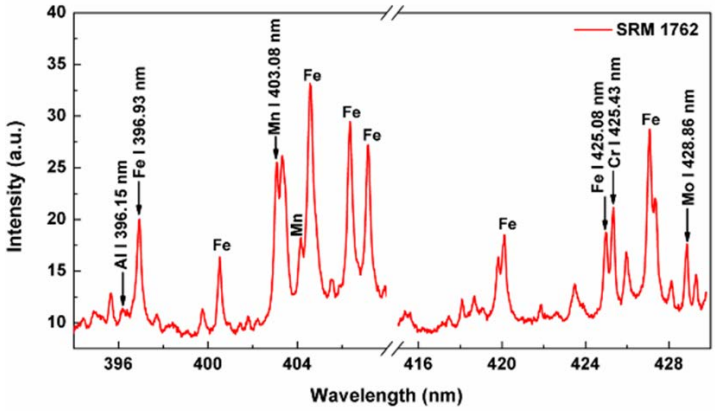

Figure 4.4 LIBS spectrum of an Al sample using 3D printed laser.

4.3 OPTIMIZATION OF 3D PRINTED PARTS

4.3.1 Reduction of thermal deformation by non-uniform structure

Given the design flexibility offered by 3D printing, advanced thermal management application with complex geometry have been studied for years.[73-75] In this study, we optimized the crystal cooling mount by reducing thermal deformation. In the end-pump configuration, the absorbed pump radiation leads to nonuniform temperature distribution in both laser rod and its mount. This results in an uneven thermal expansion, as shown in Figure 4.5 (b), in laser crystal holder due to the temperature gradient, which finally leads to cavity misalignment. 3D printing technology allows us to manufacture novel cellular structure that can reduce cavity misalignment by reducing temperature gradient within laser crystal holder.

As shown in Figure 4.5 (a), two crystal holders, one with uniform cell density (up), another with non-uniform cell density (down) were made. On the heater side of non-uniform structure, the cell density is low thus having a higher heat dissipation ability. On the mirror side of non-uniform structure, the cell density is high thus having a low heat dissipation ability. Therefore, the temperature gradient within the non-uniform structure can be reduce compared with the uniform structure where both side has similar heat dissipation ability. Thermal deformation of these two samples are calculated by measuring the deflection angle. As shown in Figure 4.5 (c), non-uniform structure can reduce thermal deformation by 41.2%.

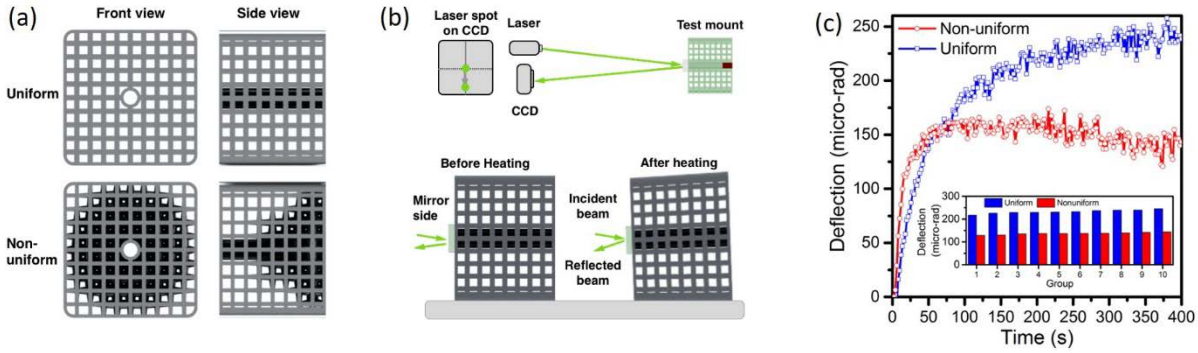

Figure 4.5 Thermal deformation of 3D printed cellular structure. (a) Schematic of non-uniform cellular structure and uniform cellular structure, (b) Schematic of Experiment setup, (c) Experiment result of non-uniform and uniform cellular structure. Non-uniform structure can reduce thermal deformation by 41.2% The experiment has been repeated 10 times as shown in the inserted figure.

4.3.2 Temperature mapping of uniform and non-uniform parts

Further verification is conducted by experiment and simulation of 3D temperature mapping of the two structures using fiber sensing. The optical fiber sensing system used in this study is an Optical Backscatter Reflectometer (LUNA OBR4600). It was configured to interrogate temperature profile of optical fiber up to 70 m in length with spatial resolution of 4 mm and temperature resolution of ~0.1°C. The optical fiber used was a conventional single mode optical fiber (SMF-28). As shown in Figure 4.6 (a), a 3D optical fiber mesh was interwoven and embedded into test samples. The optical fiber mesh had 10 layers, which extended the whole volume of the specimen vertically. Each layer of the mesh consisted of 10 parallel optical fibers which passed through respective horizontal voids, except for the layers 5 and 6 in the middle where the laser

crystal was inserted. To form the 3D optical fiber mesh, a ~60-meter-long optical fiber was used. A 4-mm long heater with 15-W output power, was inserted at the right side of sample to simulate non-uniform heating source in end-pump configuration. The temperature data recorded here was the temperature change with respect to the room temperature (20°C). By collecting all these data points and knowing their geometry coordinates, 3D temperature distribution within the sample can be reconstructed and imaged.

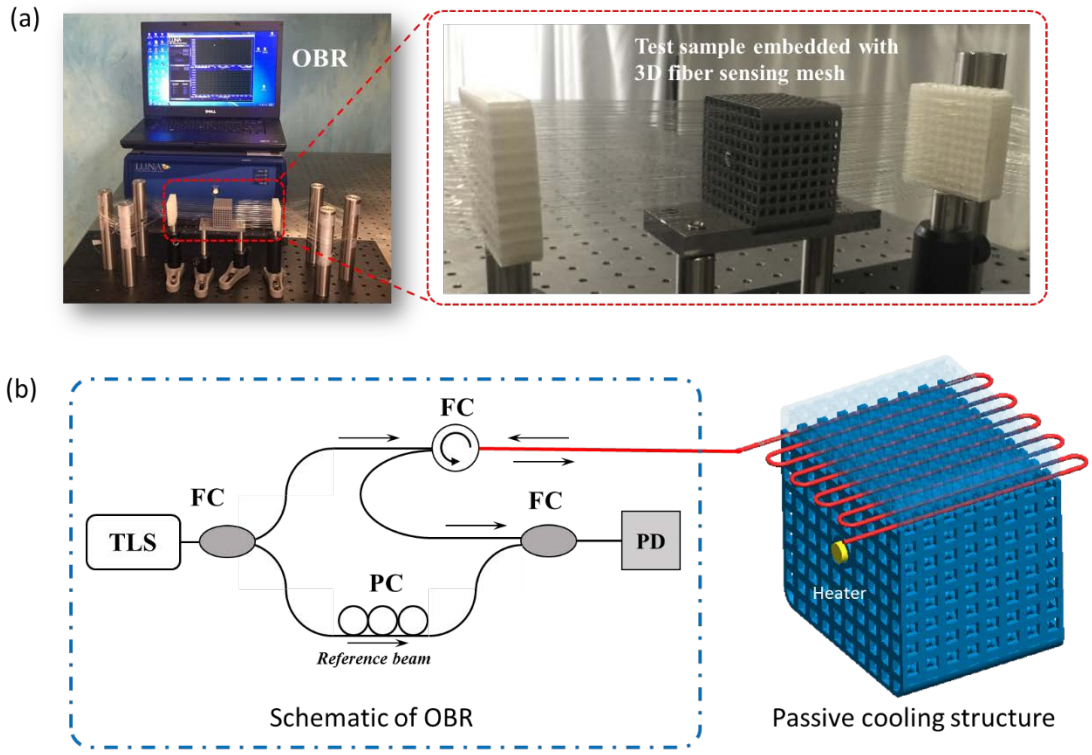

Figure 4.6 Experiment setup. Photo (a) and schematic (b) of experiment setup featuring an OBR and a passive cooling structure interwoven with 3D fiber mesh. TLS: tunable laser source, FC:fiber coupler, PC: Polarization controller, PD: photo detector, OBR: optical backscatter reflectometer.reflectometer.an OBR and a passive cooling structure interwoven with 3D fiber mesh. TLS: tunable laser source, FC:fiber coupler, PC: Polarization controller, PD: photo detector, OBR: optical backscatter reflectometer.

The distributed temperature measurement using the fiber is shown in Figure 4.7 with a spatial resolution of 4mm. Ten temperature spikes along the fiber was observed in Figure 4.7 (a), which records temperature profiles in the heated cellular structure. This is the region where fiber was inserted inside test structure. An inserted figure also shows a zoom-in temperature profile both inside and outside the cellular structure. Figure 4.7 (b) shows the 2D temperature mapping of the top layer of the cellular structure (designated as Layer 1). It is constructed using data from Figure 4.7 (a) by considering the geometric shape of the fiber thread through the cellular structure. As

shown in Figure 4.7 (b), the temperature is higher at the end where heater is inserted and gradually decreases away from the heater. Figure 4.7 (c) shows the 3D temperature mapping that is constructed from 10 layers of 2D temperature mapping. A total of 960 single temperature data points has been used to construct such a figure. This method is a significantly improvement over thermocouple measurement for interior temperature probing.

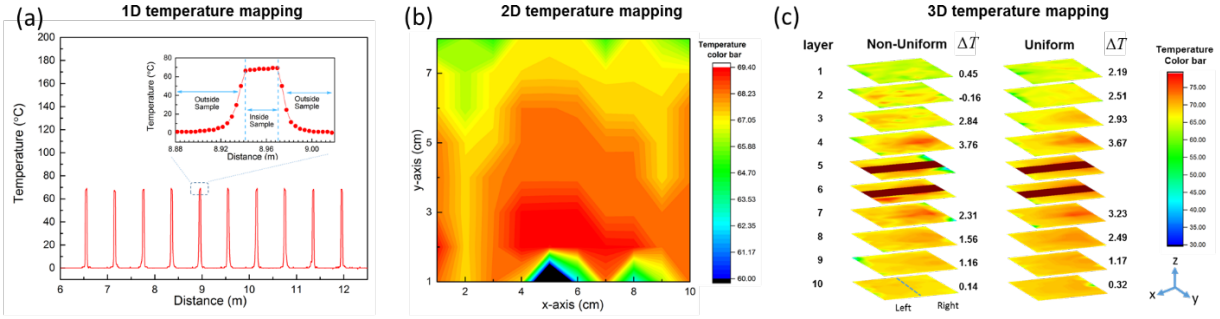

Figure 4.7 Construction of 3D temperature mapping within passive cooling structures. (a) 1D temperature mapping along fiber in layer 1 of uniform cooling structure, (b) 2D temperature mapping of layer 1 constructed from 10 sections of 1D data. (c) 3D temperature mapping of the whole structures, both uniform and non-uniform structures, each constructed from totally 10 layers of 2D data.

Figure 4.7 (c) compares temperature distribution between a non-uniform structure and a uniform cellular structure. ΔT here is defined as the average temperature difference between left side and right side of test samples. As revealing by the figure, temperature profile of non-uniform cellular structures can be significantly improved by optimizing the filling ratio of cellular structure. This will lead to a more uniform mechanic deformation upon heating and improvement of laser beam pointing and power output stabilities. At the top layer (layer 1), where convection cooling dominates, non-uniform structure reduces temperature difference from 2.19°C to 0.45°C compared with the uniform structure. This can be explained by the fact that the heater side, right side in

Figure 4.7 (c), of non-uniform structure has lower cell density, thus having a higher heat dissipation ability than the other side. As we move away from the heated side, the increased filling ratio will yield lower heat dissipation rate, resulting higher temperature than that of the uniform structures. This overall will yield more uniform temperature distribution.

4.4 CONCLUSION

In conclusion, we have demonstrated an advanced laser system made by 3D printing technology. Although the laser system chosen to exemplify this technology is relatively simple, the 3D printing technology itself has demonstrated the possibility to revolutionize the laser manufacturing industry. To our best knowledge, this is the first 3D printed laser.

This unibody laser can be widely used in the area where high energy pulse lasers are needed. Its unibody construction offers many advantages over conventional laser frames, such as being compact, lightweight and mechanically strong. It achieved all these advantages without sacrificing the functionality of the laser. Adjustable flexure optical mounts and innovative cooling structures were all built into this system.

As 3D printing technology continues to thrive, the next generation of 3d printers will be capable of fabricating parts with different materials, such as Al and glass. As this advance is realized, it may be possible to print the mirror and lens directly into the Al frame. The result will be a more robust photonic system.

5.0 ADDITIVE MANUSFACTURING OF DIAMOND METAL COMPOSITE

In previous chapter, we discussed using 3d printing technology for photonics application. The innovation is to 3D print Aluminum cellular structure to reduce weight as well as improving thermomechanical properties. In this chapter, we further explore this topic by 3D printing diamond/metal composite, a novel material with advanced thermomechanical properties. Cellular structure made of diamond/metal composite is successfully made through 3D printing.

5.1 OVERVIEW

5.1.1 Overview of diamond/metal composites

Thermal management is a critical issue in high power laser applications. [76] Reliability and long-life time of laser operation require not only materials with high thermal conductivity but also a coefficient of thermal expansion (CTE) matching to that of gain medium. The thermal expansion coefficients of copper laser crystal mount is 17 ppm/K, while the Nd:YAG laser gain medium has a thermal expansion coefficient of 7 ppm/K. Such thermal expansion coefficients mismatch will compromise high power laser application by introducing thermal stress at laser crystal.[38]

Diamond/metal composite not only exhibits high thermal conductivity but also can achieve tunable coefficient of thermal expansion by varying diamond/metal composition.[77,78] Therefore, diamond/metal composites have the potential be used as laser crystal mount that offering both high thermal conductivity and matched coefficient of thermal expansion.

Today, diamond/metal composite has been widely used in electronic packages and semiconductors industry as high performance heatsink.[79] However, such heatsink has very limited geometry such as cylinder, cube and slice. Diamond/metal composite with complex geometry such as cellular structure is very difficult to make using conventional manufacturing method because diamond/metal composite is extremely difficult to machine.

To solve this problem, we propose two innovative ways to produce diamond/metal composite with cellular structure. The first method is combining 3D printing with metal infiltration. We first use binder jetting 3d printing to make a diamond preform, then infiltrate such preform with metal. The second method is combining 3D printing with sintering. We 3D print mixed diamond/metal powder and sinter printed sample at high temperature. Both methods successfully yield diamond/metal composites with complex cellular structure.

5.2 BINDEER JETTING COMBINED WITH METAL INFILTRATION

In this section, we demonstrated the successfully making of diamond/copper alloy sample using the proposed binder jetting 3D printing combined with metal infiltration. By introduce spontaneous infiltration and low melting point metal powder into the diamond/metal composites fabrication, the most challenging problem of cutting and machining process, will be solved

efficiently. This technique will allow us to make complex diamond/metal composites at reduce cost.

5.2.1 Binder jetting technology

Binder Jetting[80] is an additive manufacturing process in which a liquid binder is selectively deposited into powder bed to join powder particles. Layers of powders are then bonded to form an object. The printing process is shown in Figure 5.1 (a). A roller first deposit a thin layer of powder. Then, the printhead strategically drops binder into the powder. The job box moves to the heater where binder solidities and joins powder particles. These three steps repeat themselves and the part develops through such process over time. The 3D printing machine, shown in Figure 5.1 (b), is X-1 Lab from ExOne, Inc. After the printing process, the sample box is carefully taken out of the machine and put into oven for post-curing at 200 C for 8 hours. When the sample is fully cured, it can be taken out of sample box. The residual powder is then removed by vacuum cleaner.

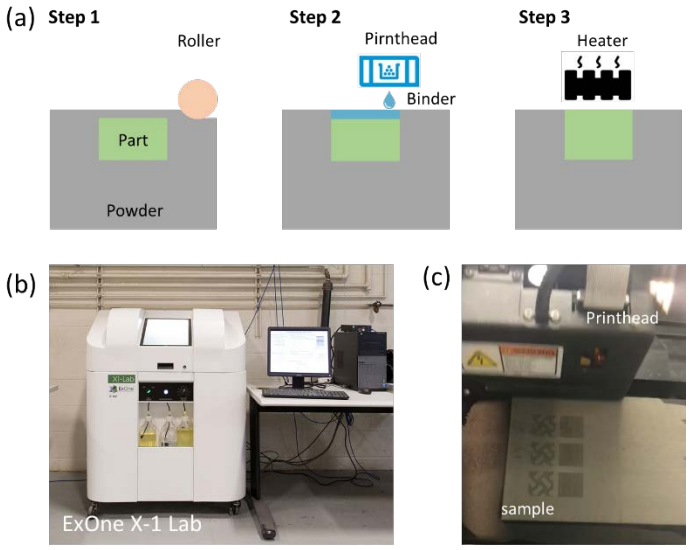

Figure 5.1 Binder jetting 3D printing. (a) Schematic of binder jetting 3D printing process, (b) Photo of binder jetting 3D printing machine, (c) Photo of 3D printing process.

5.2.2 Metal infiltration

Liquid metal infiltration of diamond preform is best suited fabrication method for our application. [81] Infiltration is a liquid-state fabrication method, in which the 3D printed diamond porous preform is impregnated in a molten matrix metal, which fills the pores between the dispersed-phase inclusions. Synthesis of porous diamond preform with sufficient mechanical strength, uniform pore distribution, pore size, and porosity level is one of the crucial steps involved in the infiltration processing.

There are two types of infiltration, forced infiltration and spontaneous infiltration.[82] Since binder jetting 3D printed diamond preform is not strong enough to withstand high pressure during forced infiltration process, only spontaneous infiltration is suitable for our application. Though the spontaneous infiltration technique is widely used to fabricate metal composite such as SiC/metal,

Mo/metal, W/metal and AlN/metal, the researches about the fabricating technique of diamond/metal composites by spontaneous infiltration are not very popular. This is mainly because there are poor wettability and high interfacial thermal resistance between diamonds and metal. To solve this problem, a thin metal (Ni or Ti) coating can be applied at the diamond surface to improve the wettability of diamond powder and liquid metal.[83] The powder we used here is micro diamond powder with particles size of ~40 μm and coated with Ti or Ni.

Infiltration temperature is a very critical parameter during infiltration. Diamond starts to undergo graphitization as low as 700°C.[84] Pure copper has a melting point of 1,085°C. To avoid diamond graphitization during copper infiltration process, we choose low melting point copper alloy as filter metal. This BCup-9 copper powder is from Prince & Izant Company. Pressure is also a critical parameter during infiltration. In a previous study [85], it is shown that diamond/metal composite can be successfully made under vacuum condition. Thus, we choose pressureless infiltration in this study. The detailed infiltration parameter is shown in Figure 5.2.

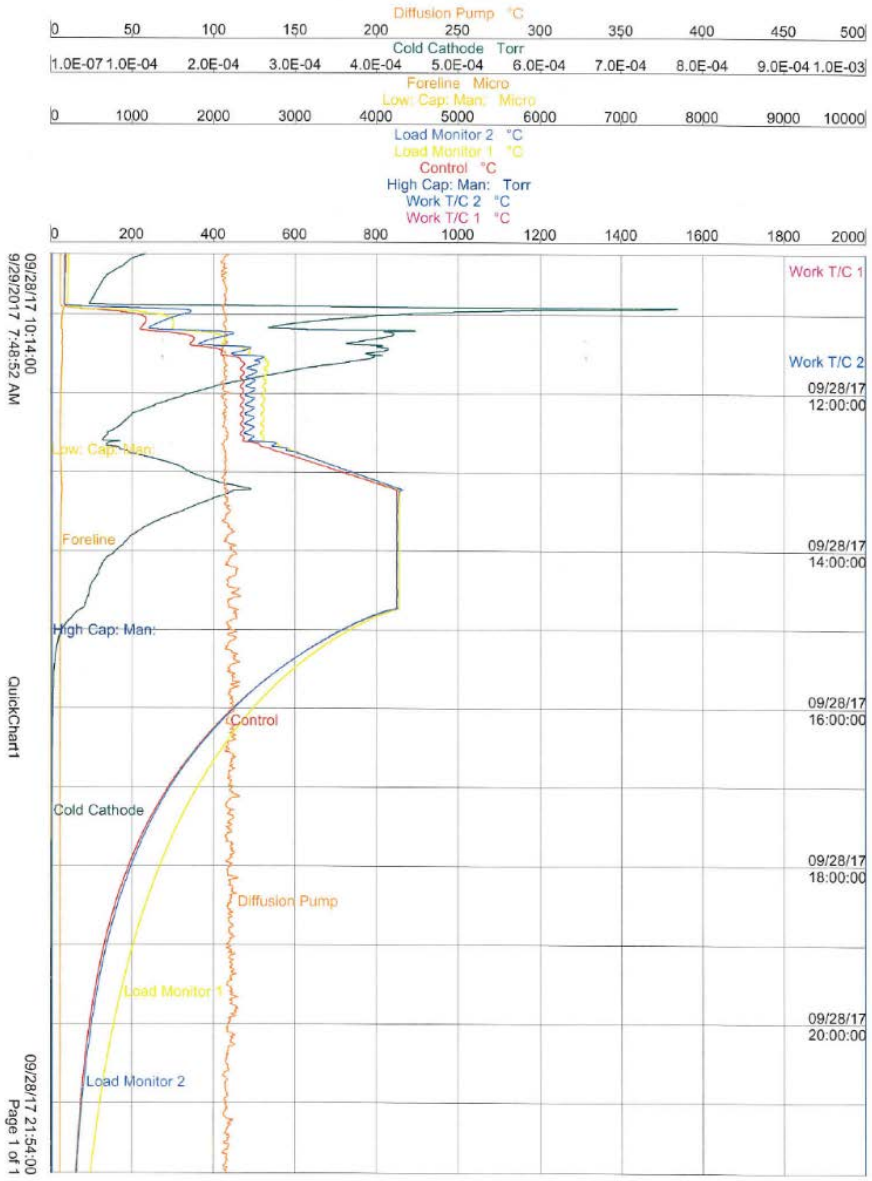

Figure 5.2 Detailed infiltration parameters.

5.2.3 Results and discussions

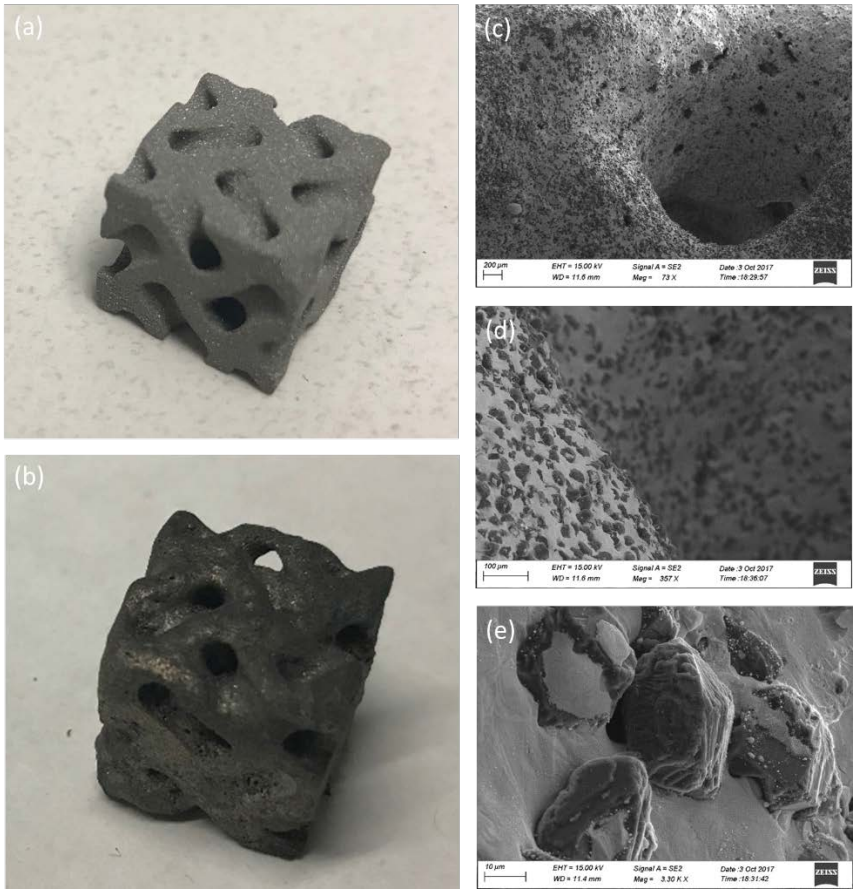

Figure 5.3 Photos and SEM images. (a) Photo of gyriod sample before infiltration, (b) Photo of gyriod sample after infiltration (c-e) SEM images of gyriod sample at various magnifications.

Figure 5.3 (a,b) shows the photos of 3D printed gyroid sample before and after infiltration. The sample maintains shape very well after infiltration. Figure 5.3 (c-d) shows SEM images of gyroid sample taken at various magnification. It clearly shows diamond particles are uniformly distributed among metal matrix.

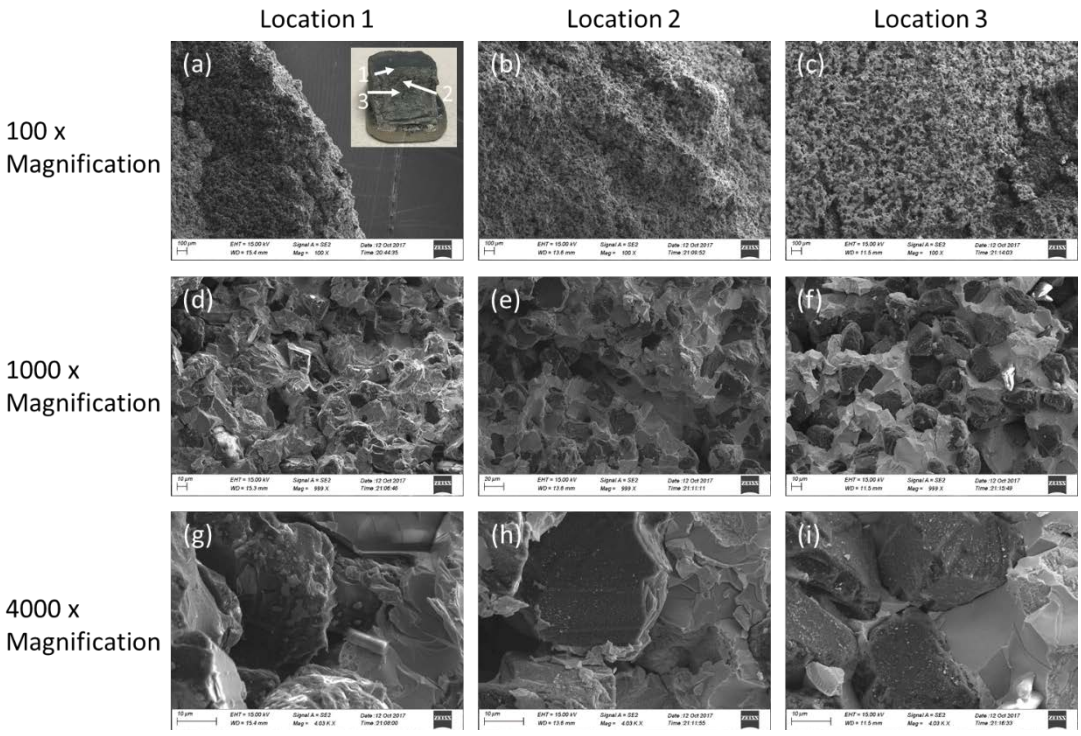

Figure 5.4 SEM images taken at three difficult sample locations and three different magnifications. Inserted photo shows the SEM location.

To further test whether infiltration process happened uniformly inside sample, we made a diamond/metal composite sample with cube shape. The sample was then broken from the middle and inspected under SEM. Figure 5.4 shows SEM images of a diamond/copper alloy composites at various sample location and magnification. This cube sample was broken from middle and SEM images were taken at three different location as labeled in the photo. The ideal is to test whether infiltration was uniform across sample. Figure 5.4 clearly shows that diamond particles are uniformly distributed among copper alloy at three locations. In the high magnification Figure 5.4 (g,h,i), shape edge can be clearly observed, indicating no significant graphitization happened.

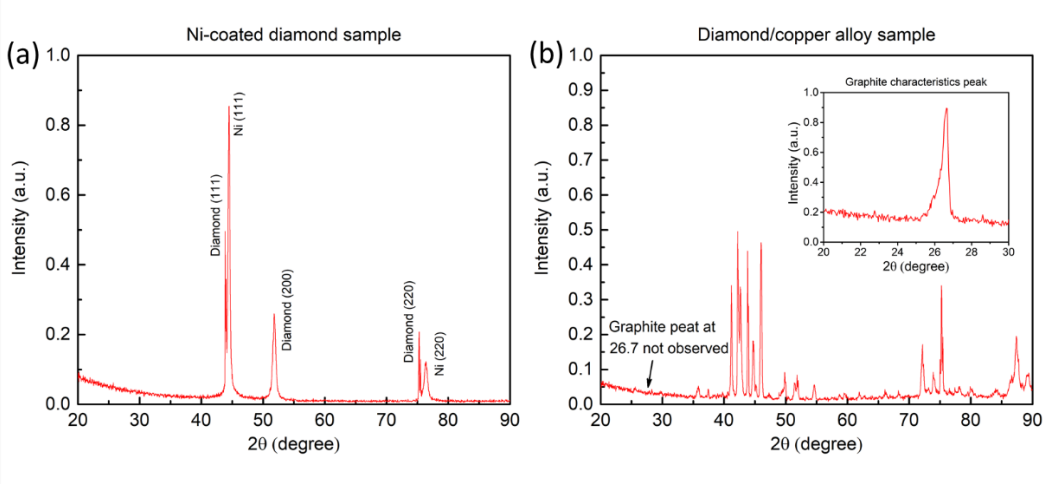

Figure 5.5 XRD result of (a) Ni-coated diamond and (b) diamond/copper alloy sample.

To further test whether graphitization happened during infiltration process, XRD patterns of a Ni-coated diamond sample before infiltration and after infiltration were taken with result shown in Figure 5.5 (a) and (b), respectively. In Figure 5.5 (a), several diamond characteristic peaks can be clearly observed. Since the graphite characteristic peak is at 26.3° and no such peak is observed in the diamond/copper alloy sample, as shown in Figure 5.5 (b), this XRD result further shows no graphitization happened during the infiltration process.

5.3 BINDER JETTING COMBINED WITH SINTERING

In this section, we demonstrated the successfully making of diamond/copper alloy sample using the proposed binder jetting combined with sintering.

5.3.1 Experiment setup

Sintering is the process of compacting and forming a solid mass of material by heat or without melting it to the point of liquefaction. Sintering is usually used to reduces the porous and enhances properties such as strength, electrical conductivity, translucency and thermal conductivity. During the sintering process, atomic diffusion drives powder surface elimination in various stages, starting from the formation of necks between powders to final elimination of small pores at the end of the process. The sample may shrink to 80% of its original size after sintering.

The method we used here is very similar to the method we used in previous section. Instead of using just diamond powder, diamond/metal mixed powder is used. Ni-coated diamond powder with average particles size of 40 μm is fully mixed with low melting point copper alloy BCup-9. Then this mixed powder is put into 3D printing machine and same printing procedure was used. After the 3D printing, the sample is put into oven for sintering.

5.3.2 Results

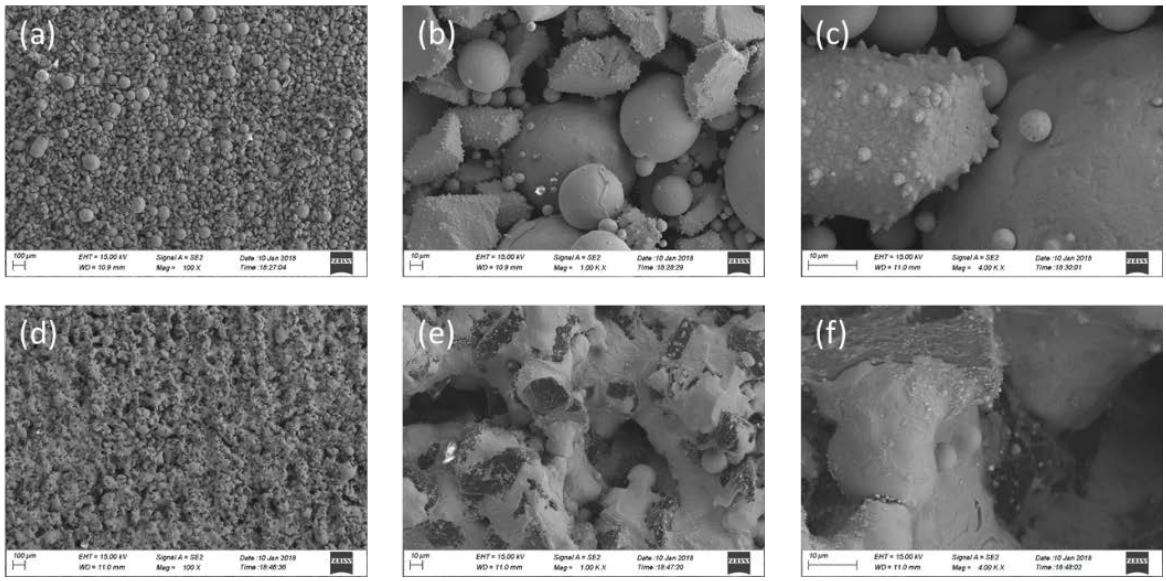

Figure 5.6 SEM image of samples (a-c) before sintering and (d-f) after sintering.

Figure 5.6 shows SEM images of samples before sintering and after sintering. It is shown in Figure 5.6 (a) and (b), the spherical metal ball and shape-edged diamond powder was mixed uniformly in sample before sintering. In Figure 5.6 (c), diamond particles were not smooth because it was covered by a thin layer of binder. Figure 5.6 (d) and (e) shows diamond particles were uniformly distributed within metal matrix. Figure 5.6 (f) also shows the bonding between diamond and metal was also very strong.

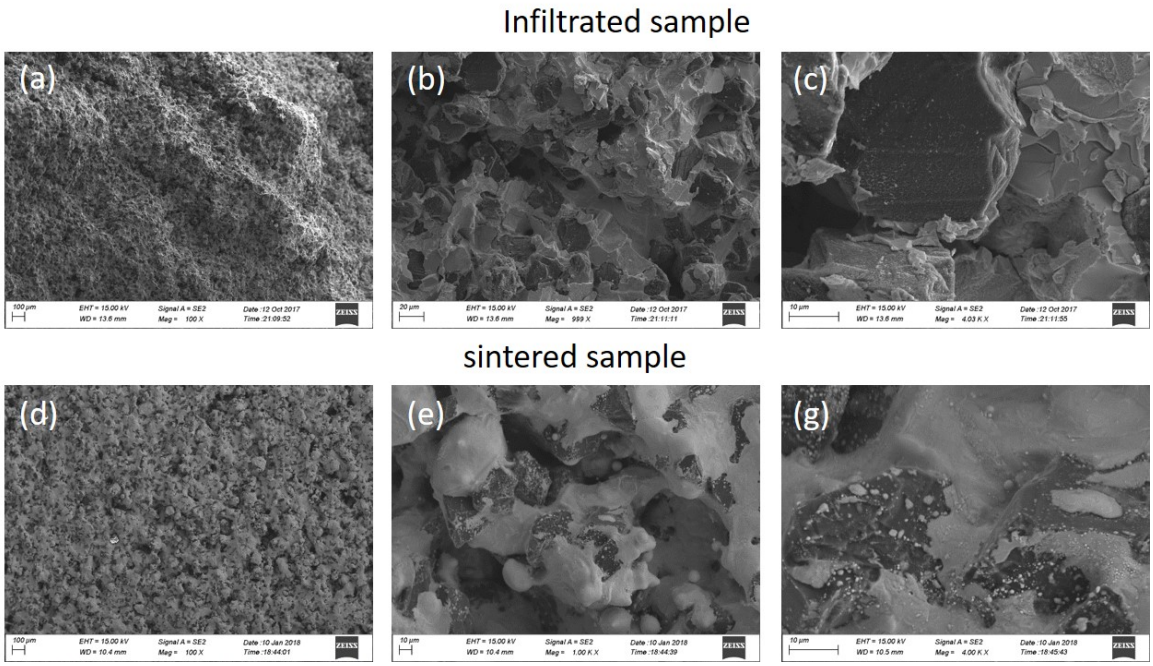

Figure 5.7 SEM images of infiltrated samples SEM images of infiltrated sample and sintered sample. (a-c) SEM images of infiltrated samples, (e-f) SEM images of sintered samples.

We also compared the sample made from infiltration and sintering with the result shown in Figure 5.7. By comparing these images, we find sintered sample has more porosity compared with infiltrated sample under the same parameters during heating process. Sintered sample will shrink to 80% of its original size while the size of infiltrated sample almost doesn't change. Since the sintered sample has higher porosity, such sample will be lighter and less strong with larger surface area compared with infiltrated sample.

5.4 CONCLUSION

In conclusion, we have demonstrated two innovative ways to make diamond/metal composites with complex geometry. No graphitization was observed, indicating excellent thermomechanical properties. These two methods we developed here can be used to develop high performance laser crystal cooling structure. The samples made from infiltration are stronger and heavier than the samples made from sintering. Therefore, these two kinds of samples can fulfil different purposes according to the requirements.

6.0 CONCLUSION AND FURTHER DIRECTION

In this dissertation, we focus on developing compact lasers for laser remote sensing applications, especially LIBS, using both conventional and advanced manufacturing method. Several compact field-portable laser systems are developed and tested for LIBS applications.

Chapter 1 served as the introduction to the fundamental of LIBS technology and compact laser sources. Chapter 2 introduces the development of a compact actively Q-switched laser. Chapter 3 further discusses the development of a field-portable double-pulse laser based on the same laser design developed in the previous chapter. It also investigates the advantages of using double-pulse LIBS during the early plasma stage. Significantly signal improvement has been observed. We also demonstrate selective signal enhancement which is usually achieved by LIBS-LIF that requires bulky and expensive high power tunable laser in the lab. The low-cost instrument and innovative technology we demonstrated here make it possible to extend such improvement to field-portable LIBS applications. By optimizing the experiment parameters, better signal improvement can be achieved. The detailed physics during the early plasmas lifetime is also deserved further studies.

Chapter 4 and 5 discuss using additive manufacturing to build compact, light-weight, rigid laser system, compared with chapter 2 and 3 where the laser systems are all built by conventional manufacturing method. Chapter 4 introduces the development of a compact unibody laser enabled

by additive manufacturing and its advantages compared with laser made by conventional method. Chapter 5 discuss 3D printing advanced diamond/metal composites with cellar structure. We exploited the flexibility of the bottom-up manufacturing schemes to produce entire laser photonic systems made of flexure, cellular structures with embedded cooling and sensing functions, as well as using advanced diamond/copper composites. 3D printing will lead to drastic reduction on labor cost in manual assembly and alignments. Further works should focus on thermal design optimizations and completely digitize the manufacturing of laser photonic systems with advantages in weight, size, thermal, mechanic performance, manufacturing costs, which are unattainable by current commercial products.

The innovation in manufacturing digitization and utilization of new materials and structures will allow rapid design modification and radical design innovation in developing laser and photonic systems for wider deployments on mobile drone platforms for a wide array of industrial, consumer and environmental applications.

APPENDIX A

LASER CAVITY ALIGNMENT

After assembling the laser, its cavity need alignment, where the front and end faces of laser cavity should be parallel to each other. It can be a difficult and frustrating task to properly perform such alignment if wrong method is used. It is even possible to move further away from the goal instead of towards it! Fortunately, there is a specific procedure that can be followed that is guaranteed to work. This method is called “walking the beam”. The ideal is based on the fact that a laser beam can be directed to any direction by using two mirrors within the limit of aperture size. A laser beam has four degrees of freedom and each mirror can control two degrees of freedom.

The cavity alignment is based on the fact that when the two end surfaces of laser cavity are parallel to each other, if a laser beam is perpendicular to one surface, it must also be perpendicular to the other surface. Based on this fact, the alignment procedure is designed as follow: First of all, using “walking the beam” method to make alignment laser beam perpendicular to the end face of laser cavity, where incident and reflected laser beams are overlapped. Secondly, adjust the front face of laser cavity to make sure the reflect laser beam is overlapped with the reflected laser beam from the end face. At this moment, two surfaces of laser cavity should be parallel to each other.

The detailed alignment method is described below. This method can also be easily adapted to align passive Q-switched laser, where Pockels cell and ¼ waveplate are replaced by saturate absorber.

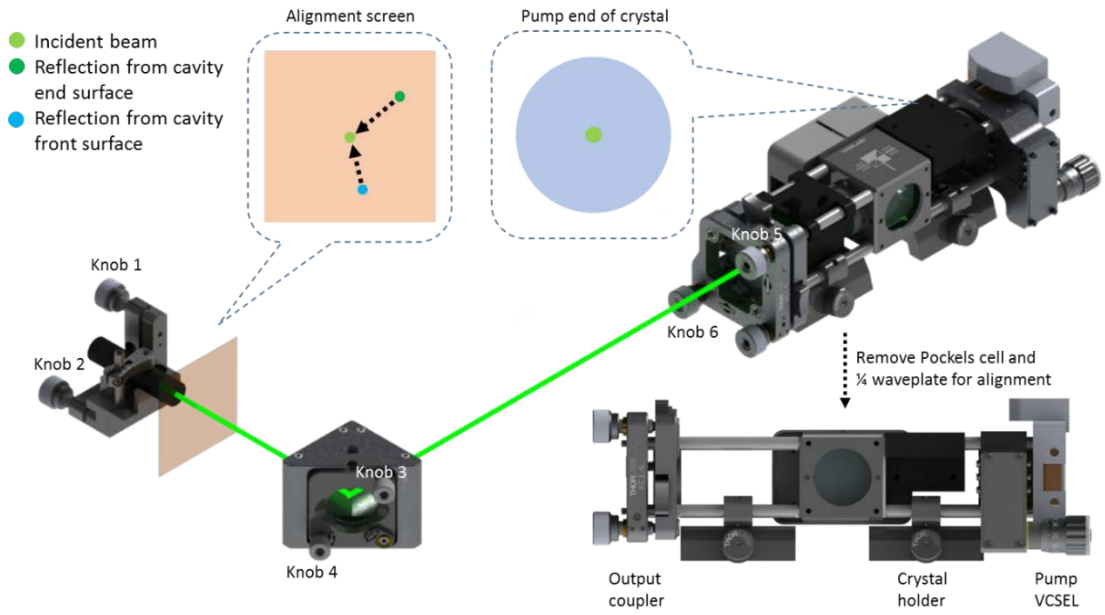

Figure A.1 Laser cavity alignment procedure.

1. Setup laser alignment system as shown in Figure A.1.
    a. Remove output coupler, Pockels cell and ¼ waveplate from Q-switch laser to reduce ghost image.
    b. Mount a 532-nm laser pointer on a kinematic mount. Then direct laser beam into laser cavity through a right-angle kinematic mount. Make sure laser beam is parallel to optical table.
    c. Mount the laser body to optical table so that laser beam can be directed roughly to the center of pump end of crystal and through the center of beam splitter at the same time. This is crucial for the following alignment since the range of alignment knobs are limited. A good initial course alignment is beneficial to the following fine alignment.
2. Direct the laser beam perpendicular to laser crystal end face
    a. Adjust knob 1 to center laser spot vertically on the back of crystal
    b. Adjust knob 3 to center the reflected laser spot vertically overlapped with incident beam
    c. Repeat step a and b to get as close as you can
    d. Adjust knob 2 to center laser spot horizontally on the back of crystal
    e. Adjust knob 4 to center the reflected laser spot horizontally overlapped with incident beam
    f. Repeat step d and e to get as close as you can
    g. Now the incident laser beam should be perpendicular to crystal pump end
3. Direct the laser beam perpendicular to output coupler.
    a. Add output coupler to laser
    b. Adjust knob 5 and knob 6 to overlap the reflected laser beam with incident beam
    c. Now the incident laser beam should be perpendicular to output coupler and the two faces of laser cavity are parallel to each other.
4. Fine adjustment using power meter in long pulse mode

a. Turn off Pockels cell driver to avoid high voltage shock!
b. Turn on pumping VCSEL. Use the maximum allowed power. The laser should begin to lase in long pulse mode. When putting a IR card in front of laser, a bright spot should be seen on that card
c. Put a power meter in front of laser cavity. Adjust knob 5 and knob 6 slowly to maximize laser output power. The power meter must stand high peak laser output power.

5. Final adjustment in Q-switch mode
    a. Put ¼ plate back into laser cavity. Turn on pump VCSEL and rotate ¼ plate to minimize the laser output power.
    b. Put Pockels cell back into laser cavity and turn on its driver. Turn on pump VCSEL. Adjust knob 5 and knob 6 to maximum laser output.

APPENDIX B

FIFTH HARMONIC GENERATION

After assembling the fifth harmonic generator, it need alignment to obtain maximum conversion efficiency by angle tilting. There are two axes for tilting crystal angles. Because the commercial available NLO crystals are normally cut in a principal crystal plane, conversion efficiency is only sensitive to the axis that is perpendicular to the principal crystal plane. Such plane is marked by a black line. The nonlinear crystal is mounted on a mirror mount that offer two angle adjustments. To separate the different harmonics, a Pellin Broca Prism made of CaF_2 is used to reduce the UV light absorption. A screen made of white paper is used to find the laser output. The experiment setup is shown in Figure A.2. The alignment steps are shown below.

1. Setup alignment system as shown in the figure.
    a. The incident laser beam should be parallel to the optical table and its polarization is perpendicular to the optical table.
    b. All the optical axis of the optical components should also be parallel to the optical table.
    c. The distance between prism and screen is about 40 cm.
    d. Maximize laser output.
2. Generating second harmonic
    a. Put the second harmonic laser crystal into mirror mount and make sure black marker is on top.
    b. Make incident laser beam roughly perpendicular to laser crystal front face.
    c. Use IR card to find the 1064 nm spot on the screen and mark it.

d. Adjust knob 1. A green dot should be seen on the screen.
e. Remove the screen and use a power meter to measure the 532 nm power. Make sure only 532 nm laser beam is collected by power meter.
f. Adjust knob 1 very slowly to get the maximum 532 nm output power.

3. Generating fourth harmonic
   a. Put fourth harmonic laser crystal into mirror mount and make sure the black maker is on the side. Make incident laser beam roughly perpendicular to laser crystal front face.
   b. Put away power meter and bring back screen.
   c. Adjust knob 4 very slowly and a blue spot should be found on the screen. Here you must pay attention to the distance between different spot. 266 spot is much far away from 532.
   d. Remove the screen and use a power meter to measure the 266 nm power. Make sure only 266 nm laser beam is collected by power meter.
   e. Adjust knob 1 very slowly to get the maximum 266 nm output power.
4. Generating fifth harmonic
   a. Put fifth harmonic laser crystal into mirror mount and make sure the black maker is on top.
   b. Make incident laser beam roughly perpendicular to laser crystal front face.
   c. Put away power meter and bring back screen.
   d. Adjust knob 5 very slowly and a very dim blue spot should be found on the screen. Such spot can be different to see especially when wearing protecting goggle. Turn off the ambient light may help.
   e. Remove the screen and use a power meter to measure the 213 nm power. Make sure only 213 nm laser beam is collected by power meter. Block the other wavelength or move power meter further away from prism if necessary.
   f. Adjust knob 6 very slowly to get the maximum 266 nm output power.
   g. You should get about ~1% conversion efficiency.

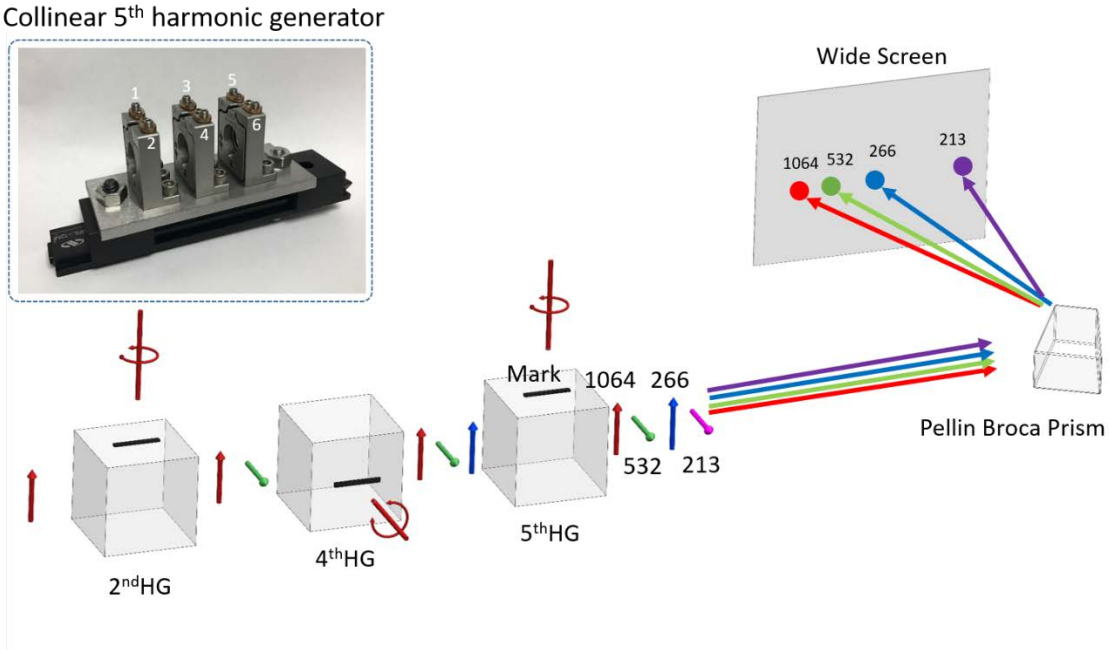

Figure A.2 Schematic of fifth harmonic generation.

APPENDIX C

DESIGN OF LASER CONTROLLER PCB

(a)

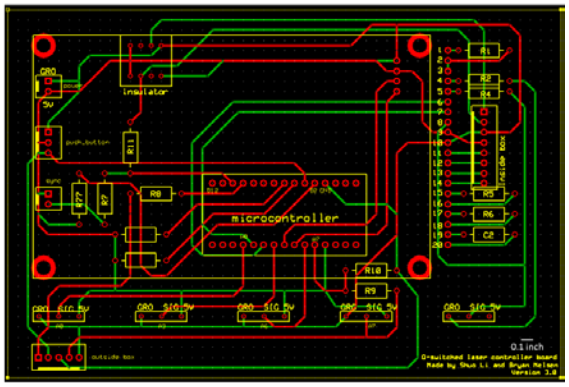

(b)

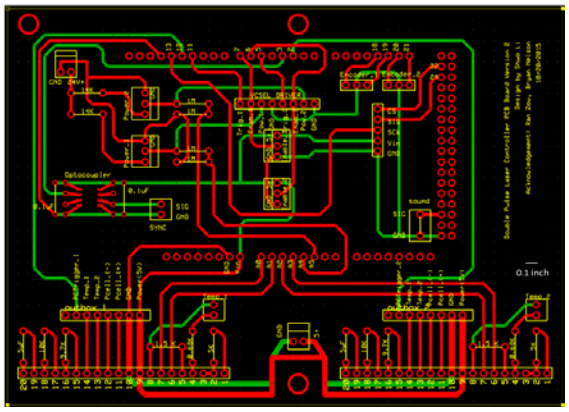

Figure A.3 PCB of single-pulse and double-pulse laser controllers

APPENDIX D

ARDUINO MICROCONTROLLER LIBRARIES

Table A.1 Libraries used for Arduino microcontroller coding.

Library name	Function
avr/io.h	The Arduino system is based on the avr-gcc compiler and makes use of the standard AVR libc libraries, specifically written for Atmel hardware. This library is used to control the trigger signals for VCSEL and Pockels cell.
Encoder.h	This library is used to get the input from encoder.
U8glib.h	This library is used to drive the 128x64 LCD display
LiquidCrystal_I2C.h	This library is used to drive the 128x32 LCD display
pitches.h	This library is used to drive the piezo buzzer.

BIBLIOGRAPHY

1 Jagdish P.Singh, S. N. T. Laser-induced Breakdown Spectroscopy. (ELSEVIER, 2007).

2 Rusak, D. A., Castle, B. C., Smith, B. W. & Winefordner, J. D. Fundamentals and Applications of Laser-Induced Breakdown Spectroscopy. Crit Rev Anal Chem 27, 257-290, doi:10.1080/10408349708050587 (1997).

3 Rakovsky, J., Cermak, P., Musset, O. & Veis, P. A review of the development of portable laser induced breakdown spectroscopy and its applications. Spectrochim Acta B 101, 269-287, doi:10.1016/j.sab.2014.09.015 (2014).

4 Goldberg, L., McIntosh, C. & Cole, B. VCSEL end-pumped passively Q-switched Nd:YAG laser with adjustable pulse energy. Opt Express 19, 4261-4267, doi:10.1364/OE.19.004261 (2011).

5 Babushok, V. I., DeLucia, F. C., Gottfried, J. L., Munson, C. A. & Miziolek, A. W. Double pulse laser ablation and plasma: Laser induced breakdown spectroscopy signal enhancement. Spectrochim Acta B 61, 999-1014, doi:10.1016/j.sab.2006.09.003 (2006).

6 Noll, R. Laser-Induced Breakdown Spectroscopy Fundamentals and Applications. 544 (Springer-Verlag Berlin Heidelberg, 2012).

7 Colao, F., Lazic, V., Fantoni, R. & Pershin, S. A comparison of single and double pulse laser-induced breakdown spectroscopy of aluminum samples. Spectrochim Acta B 57, 1167-1179, doi:Pii S0584-8547(02)00058-7

8 GobernadoMitre, I., Prieto, A. C., Zafiropulos, V., Spetsidou, Y. & Fotakis, C. On-line monitoring of laser cleaning of limestone by laser-induced breakdown spectroscopy and laser-induced fluorescence. Appl Spectrosc 51, 1125-1129, doi:Doi 10.1366/0003702971941944 (1997).

9 Measures, R. M. & Kwong, H. S. TABLASER: trace (element) analyzer based on laser ablation and selectively excited radiation. Applied optics 18, 281-286, doi:10.1364/AO.18.000281 (1979).

10 Hilbk-Kortenbruck, F., Noll, R., Wintjens, P., Falk, H. & Becker, C. Analysis of heavy metals in soils using laser-induced breakdown spectrometry combined with laser-induced fluorescence. Spectrochim Acta B 56, 933-945, doi:Doi 10.1016/S0584-8547(01)00213-0 (2001).

11 Guo, L. B. et al. Plasma confinement by hemispherical cavity in laser-induced breakdown spectroscopy. Appl Phys Lett 98, doi:Artn 131501

12 Shen, X. K., Lu, Y. F., Gebre, T., Ling, H. & Han, Y. X. Optical emission in magnetically confined laser-induced breakdown spectroscopy. J Appl Phys 100, doi:Artn 053303

13 Nassef, O. A. & Elsayed-Ali, H. E. Spark discharge assisted laser induced breakdown spectroscopy. Spectrochim Acta B 60, 1564-1572, doi:10.1016/j.sab.2005.10.010 (2005).

14 Tereszchuk, K. A., Vadillo, J. M. & Laserna, J. J. Depth profile analysis of layered samples using glow discharge assisted Laser-induced Breakdown Spectrometry (GD-LIBS). Spectrochim Acta B 64, 378-383, doi:10.1016/j.sab.2009.04.005 (2009).

15 Liu, L. et al. Flame-enhanced laser-induced breakdown spectroscopy. Optics express 22, 7686-7693, doi:10.1364/OE.22.007686 (2014).

16 Liu, L. et al. Laser-induced breakdown spectroscopy enhanced by a micro torch. Opt Express 23, 15047-15056, doi:10.1364/OE.23.015047 (2015).

17 Ikeda, Y., Moon, A. & Kaneko, M. Development of microwave-enhanced spark-induced breakdown spectroscopy. Appl Optics 49, C95-C100, doi:10.1364/Ao.49.000c95 (2010).

18 Liu, Y. A., Baudelet, M. & Richardson, M. Elemental analysis by microwave-assisted laser-induced breakdown spectroscopy: Evaluation on ceramics. J Anal Atom Spectrom 25, 1316-1323, doi:10.1039/c003304a (2010).

19 Effenberger, A. J., Jr. & Scott, J. R. Effect of atmospheric conditions on LIBS spectra. Sensors (Basel) 10, 4907-4925, doi:10.3390/s100504907 (2010).

20 Salle, B., Cremers, D. A., Maurice, S. & Wiens, R. C. Laser-induced breakdown spectroscopy for space exploration applications: Influence of the ambient pressure on the calibration curves prepared from soil and clay samples. Spectrochim Acta B 60, 479-490, doi:10.1016/j.sab.2005.02.009 (2005).

21 Noda, M., Deguchi, Y., Iwasaki, S. & Yoshikawa, N. Detection of carbon content in a high-temperature and high-pressure environment using laser-induced breakdown spectroscopy. Spectrochim Acta B 57, 701-709, doi:Pii S0584-8547(01)00403-7

22 Lopez-Moreno, C. et al. Test of a stand-off laser-induced breakdown spectroscopy sensor for the detection of explosive residues on solid surfaces. J Anal Atom Spectrom 21, 55-60, doi:10.1039/b508055j (2006).

23 Harmon, R. S. et al. Laser-induced breakdown spectroscopy - An emerging chemical sensor technology for real-time field-portable, geochemical, mineralogical, and environmental applications. Appl Geochem 21, 730-747, doi:10.1016/j.apgeochem.2006.02.003 (2006).

24 Yamamoto, K. Y., Cremers, D. A., Ferris, M. J. & Foster, L. E. Detection of metals in the environment using a portable laser-induced breakdown spectroscopy instrument. Appl Spectrosc 50, 222-233, doi:Doi 10.1366/0003702963906519 (1996).

25 Fortes, F. J., Cunat, J., Cabalin, L. M. & Laserna, J. J. In situ analytical assessment and chemical imaging of historical buildings using a man-portable laser system. Appl Spectrosc 61, 558-564, doi:Doi 10.1366/000370207780807722 (2007).

26 Gravel, J. F. Y., Doucet, F. R., Bouchard, P. & Sabsabi, M. Evaluation of a compact high power pulsed fiber laser source for laser-induced breakdown spectroscopy. J Anal Atom Spectrom 26, 1354-1361, doi:10.1039/c0ja00228c (2011).

27 Gornushkin, I. B., Amponsah-Manager, K., Smith, B. W., Omenetto, N. & Winefordner, J. D. Microchip laser-induced breakdown spectroscopy: a preliminary feasibility investigation. Appl Spectrosc 58, 762-769, doi:10.1366/0003702041389427 (2004).

28 Goujon, J. et al. A compact and portable laser-induced breakdown spectroscopy instrument for single and double pulse applications. Spectrochim Acta B 63, 1091-1096, doi:10.1016/j.sab.2008.08.019 (2008).

29 Wiens, R. C. et al. The ChemCam Instrument Suite on the Mars Science Laboratory (MSL) Rover: Body Unit and Combined System Tests. Space Sci Rev 170, 167-227, doi:10.1007/s11214-012-9902-4 (2012).

30 Lear, K. L., Choquette, K. D., Schneider, R. P., Kilcoyne, S. P. & Geib, K. M. Selectively Oxidized Vertical-Cavity Surface-Emitting Lasers with 50-Percent Power Conversion Efficiency. Electron Lett 31, 208-209, doi:Doi 10.1049/El:19950125 (1995).

31 Clarkson, W. A. et al. High power 808 nm VCSEL arrays for pumping of compact pulsed high energy Nd:YAG lasers operating at 946 nm and 1064 nm for blue and UV light generation. Proc. SPIE 7912, Solid State Lasers XX: Technology and Devices, 7912, 79120Z-79120Z-79127, doi:10.1117/12.873952 (2011).

32 Stampfl, J. & Liska, R. New materials for rapid prototyping applications. Macromolecular Chemistry and Physics 206, 1253-1256, doi:Doi 10.1002/Macp.200500199 (2005).

33 Murphy, S. V. & Atala, A. 3D bioprinting of tissues and organs. Nat Biotechnol 32, 773-785, doi:10.1038/nbt.2958 (2014).

34 Ahn, B. Y. et al. Omnidirectional printing of flexible, stretchable, and spanning silver microelectrodes. Science 323, 1590-1593, doi:10.1126/science.1168375 (2009).

35 Lewis, J. A. & Ahn, B. Y. Device fabrication: Three-dimensional printed electronics. Nature 518, 42-43, doi:10.1038/518042a (2015).

36 Symes, M. D. et al. Integrated 3D-printed reactionware for chemical synthesis and analysis. Nat Chem 4, 349-354, doi:10.1038/nchem.1313 (2012).

37 Hod Lipson, M. K. Fabricated: The New World of 3D Printing. (2013).

38 Koechner, W. Solid-State Laser Engineering. (Springer New York, 2006).

39 Van Leeuwen, R. et al. 83810I-83810I-83817.

40 Xu, R. V. L. Y. X. L. S. W. J.-F. S. G. High power 808 nm VCSEL arrays for pumping of compact pulsed high energy Nd:YAG lasers operating at 946 nm and 1064 nm for blue and UV light generation. Proc. SPIE 7912, Solid State Lasers XX: Technology and Devices, 79120Z (2011).

41 Vurgaftman, I., Meyer, J. R. & Ram-Mohan, L. R. Mid-IR vertical-cavity surface-emitting lasers. Quantum Electronics, IEEE Journal of 34, 147-156, doi:10.1109/3.655018 (1998).

42 Wintner, E., Kofler, H., Srivastava, D. K. & Agarwal, A. K. 90650B-90650B-90612.

43 Farrukh, U. O. & Brockman, P. Temperature distribution in side- and end-pumped laser crystal rods: temporal and spatial variations. Appl Opt 32, 2075-2081, doi:10.1364/AO.32.002075 (1993).

44 Castle, B. C., Talabardon, K., Smith, B. W. & Winefordner, J. D. Variables influencing the precision of laser-induced breakdown spectroscopy measurements. Appl Spectrosc 52, 649-657, doi:Doi 10.1366/0003702981944300 (1998).

45 Borisov, O. V., Mao, X. L. & Russo, R. E. Effects of crater development on fractionation and signal intensity during laser ablation inductively coupled plasma mass spectrometry. Spectrochim Acta B 55, 1693-1704, doi:Doi 10.1016/S0584-8547(00)00272-X (2000).

46 Ismail, M. A. et al. Comparison of detection limits, for two metallic matrices, of laser-induced breakdown spectroscopy in the single and double-pulse configurations. Analytical and bioanalytical chemistry 385, 316-325, doi:10.1007/s00216-006-0363-z (2006).

47 Pichahchy, A. E., Cremers, D. A. & Ferris, M. J. Elemental analysis of metals under water using laser-induced breakdown spectroscopy. Spectrochim Acta B 52, 25-39, doi:Doi 10.1016/S0584-8547(96)01575-3 (1997).

48 Scaffidi, J., Angel, S. M. & Cremers, D. A. Emission enhancement mechanisms in dual-pulse LIBS. Analytical chemistry 78, 24-32 (2006).

49 St-Onge, L., Sabsabi, M. & Cielo, P. Analysis of solids using laser-induced plasma spectroscopy in double-pulse mode. Spectrochim Acta B 53, 407-415, doi:Doi 10.1016/S0584-8547(98)00080-9 (1998).

50 Cremers, D. A. et al. Monitoring Uranium, Hydrogen, and Lithium and Their Isotopes Using a Compact Laser-Induced Breakdown Spectroscopy (LIBS) Probe and High-Resolution Spectrometer. Appl Spectrosc 66, 250-261, doi:10.1366/11-06314 (2012).

51 Baudelet, M., Willis, C. C. C., Shah, L. & Richardson, M. Laser-induced breakdown spectroscopy of copper with a 2 mu m thulium fiber laser. Opt Express 18, 7905-7910, doi:10.1364/Oe.18.007905 (2010).

52 Huang, H., Yang, L. M. & Liu, J. Qualitative assessment of laser-induced breakdown spectra generated with a femtosecond fiber laser. Applied optics 51, 8669-8676, doi:10.1364/AO.51.008669 (2012).

53 Wormhoudt, J., Iannarilli, F. J., Jones, S., Annen, K. D. & Freedman, A. Determination of carbon in steel by laser-induced breakdown spectroscopy using a microchip laser and miniature spectrometer. Appl Spectrosc 59, 1098-1102, doi:Doi 10.1366/0003702055012528 (2005).

54 Wainner, R. T., Harmon, R. S., Miziolek, A. W., McNesby, K. L. & French, P. D. Analysis of environmental lead contamination: comparison of LIBS field and laboratory instruments. Spectrochim Acta B 56, 777-793, doi:Doi 10.1016/S0584-8547(01)00229-4 (2001).

55 Piñon, V., Fotakis, C., Nicolas, G. & Anglos, D. Double pulse laser-induced breakdown spectroscopy with femtosecond laser pulses. Spectrochimica Acta Part B: Atomic Spectroscopy 63, 1006-1010, doi:10.1016/j.sab.2008.09.004 (2008).

56 Piscitelli, V. et al. Double pulse laser induced breakdown spectroscopy: Experimental study of lead emission intensity dependence on the wavelengths and sample matrix. Spectrochim Acta B 64, 147-154, doi:10.1016/j.sab.2008.11.008 (2009).

57 Heilbrunner, H. et al. Double-pulse laser-induced breakdown spectroscopy for trace element analysis in sintered iron oxide ceramics. Appl Phys a-Mater 106, 15-23, doi:10.1007/s00339-011-6669-5 (2012).

58 Nagli, L., Gaft, M. & Gornushkin, I. Comparison of single and double-pulse excitation during the earliest stage of laser induced plasma. Analytical and bioanalytical chemistry 400, 3207-3216, doi:10.1007/s00216-011-4806-9 (2011).

59 Sangines, R. & Sobral, H. Time resolved study of the emission enhancement mechanisms in orthogonal double-pulse laser-induced breakdown spectroscopy. Spectrochim Acta B 88, 150-155, doi:10.1016/j.sab.2013.06.008 (2013).

60 Liu, H. C., Mao, X. L., Yoo, J. H. & Russo, R. E. Early phase laser induced plasma diagnostics and mass removal during single-pulse laser ablation of silicon. Spectrochim Acta B 54, 1607-1624, doi:Doi 10.1016/S0584-8547(99)00092-0 (1999).

61 Asgill, M. E., Brown, M. S., Frische, K., Roquemore, W. M. & Hahn, D. W. Double-pulse and single-pulse laser-induced breakdown spectroscopy for distinguishing between

gaseous and particulate phase analytes. Applied optics 49, C110-C119, doi:10.1364/Ao.49.00c110 (2010).

62 De Giacomo, A., Dell'Aglio, M., Bruno, D., Gaudiuso, R. & De Pascale, O. Experimental and theoretical comparison of single-pulse and double-pulse laser induced breakdown spectroscopy on metallic samples. Spectrochim Acta B 63, 805-816, doi:10.1016/j.sab.2008.05.002 (2008).

63 Li, S. et al. in Conference on Lasers and Electro-Optics. AM2A.5 (Optical Society of America).

64 Liu, L. et al. Detection of trace-level uranium and samarium in glasses by combined laser-induced breakdown spectroscopy and plasma-induced fluorescence spectroscopy. J Anal Atom Spectrom 30, 1128-1132, doi:10.1039/c5ja00020c (2015).

65 Li, Y. M. & Xu, Q. S. A Novel Piezoactuated XY Stage With Parallel, Decoupled, and Stacked Flexure Structure for Micro-/Nanopositioning. Ieee Transactions on Industrial Electronics 58, 3601-3615, doi:Doi 10.1109/Tie.2010.2084972 (2011).

66 Zok, F. W. et al. Structural performance of metallic sandwich panels with square honeycomb cores. Philos Mag 85, 3207-3234, doi:Doi 10.1080/14786430500073945 (2005).

67 Compton, B. G. & Lewis, J. A. 3D-Printing of Lightweight Cellular Composites. Adv Mater 26, 5930-5935, doi:10.1002/adma.201401804 (2014).

68 M.F. Ashby, A. G. E., N.A. Fleck, L.J. Gibson, J.W. Hutchinson and H.N.G. Wadley (Butterworth-Heinemann).

69 Andreas Öchsner, G. E. M., Marcelo J. S. de Lemos. Cellular and Porous Materials: Thermal Properties Simulation and Prediction.

70 Evans, A. G., Hutchinson, J. W., Fleck, N. A., Ashby, M. F. & Wadley, H. N. G. The topological design of multifunctional cellular metals. Prog Mater Sci 46, 309-327, doi:Doi 10.1016/S0079-6425(00)00016-5 (2001).

71 Kim, G. D. & Oh, Y. T. A benchmark study on rapid prototyping processes and machines: quantitative comparisons of mechanical properties, accuracy, roughness, speed, and material cost. P I Mech Eng B-J Eng 222, 201-215, doi:Doi 10.1243/09544054jem724 (2008).

72 Andreas Öechsner, C. A. Multifunctional Metallic Hollow Sphere Structures. (Springer-Verlag Berlin Heidelberg, 2009).

73 Horn, T. J. & Harrysson, O. L. Overview of current additive manufacturing technologies and selected applications. Sci Prog 95, 255-282 (2012).

74 Wong, M., Tsopanos, S., Sutcliffe, C. & Owen, E. Selective laser melting of heat transfer devices. Rapid Prototyping J 13, 291-297, doi:10.1108/13552540710824797 (2007).

75 Sachs, E., Wylonis, E., Allen, S., Cima, M. & Guo, H. L. Production of injection molding tooling with conformal cooling channels using the three dimensional printing process. Polym Eng Sci 40, 1232-1247, doi:DOI 10.1002/pen.11251 (2000).

76 Liu, X. S., Hu, M. H., Caneau, C. G., Bhat, R. & Zah, C. E. Thermal management strategies for high power semiconductor pump lasers. Ieee T Compon Pack T 29, 268-276, doi:10.1109/Tcapt.2006.875878 (2006).

77 Prieto, R., Molina, J. M., Narciso, J. & Louis, E. Fabrication and properties of graphite flakes/metal composites for thermal management applications. Scripta Mater 59, 11-14, doi:10.1016/j.scriptamat.2008.02.026 (2008).

78 Qu, X. H., Zhang, L., Wu, M. & Ren, S. B. Review of metal matrix composites with high thermal conductivity for thermal management applications. Prog Nat Sci-Mater 21, 189-197, doi:Doi 10.1016/S1002-0071(12)60029-X (2011).

79 Abyzov, A. M., Kidalov, S. V. & Shakhov, F. M. High thermal conductivity composite of diamond particles with tungsten coating in a copper matrix for heat sink application. Appl Therm Eng 48, 72-80, doi:10.1016/j.applthermaleng.2012.04.063 (2012).

80 Gao, W. et al. The status, challenges, and future of additive manufacturing in engineering. Comput Aided Design 69, 65-89, doi:10.1016/j.cad.2015.04.001 (2015).

81 Beffort, O., Vaucher, S. & Khalid, F. A. On the thermal and chemical stability of diamond during processing of Al/diamond composites by liquid metal infiltration (squeeze casting). Diam Relat Mater 13, 1834-1843, doi:10.1016/j.diamond.2004.04.014 (2004).

82 Manu, K. M. S., Raag, L. A., Rajan, T. P. D., Gupta, M. & Pai, B. C. Liquid Metal Infiltration Processing of Metallic Composites: A Critical Review. Metall Mater Trans B 47, 2799-2819, doi:10.1007/s11663-016-0751-5 (2016).

83 Dong, Y. H., Zhang, R. Q., He, X. B., Ye, Z. G. & Qu, X. H. Fabrication and infiltration kinetics analysis of Ti-coated diamond/copper composites with near-net-shape by pressureless infiltration. Mater Sci Eng B-Adv 177, 1524-1530, doi:10.1016/j.mseb.2012.08.009 (2012).

84 Fedoseev, D. V., Vnukov, S. P., Bukhovets, V. L. & Anikin, B. A. Surface Graphitization of Diamond at High-Temperatures. Surf Coat Tech 28, 207-214, doi:Doi 10.1016/0257-8972(86)90059-9 (1986).

85 Dong, Y. H., He, X. B., Rafi-ud-din, Xu, L. A. & Qu, X. H. Fabrication and thermal conductivity of near-net-shaped diamond/copper composites by pressureless infiltration. J Mater Sci 46, 3862-3867, doi:10.1007/s10853-011-5307-0 (2011).